Experimental and Numerical Investigation of Turbulent Vortex Shedding

Hamidreza Shiri

Submitted to the
Institute of Graduate Studies and Research
in partial fulfillment of the requirements for the degree of

Doctor of Philosophy
in
Mechanical Engineering

Eastern Mediterranean University
July 2021
Gazimağusa, North Cyprus

Approval of the Institute of Graduate Studies and Research

Prof. Dr. Ali Hakan Ulusoy
Director

I certify that this thesis satisfies all the requirements as a thesis for the degree of Doctor of Philosophy in Mechanical Engineering.

Prof. Dr. Hasan Hacışevki
Chair, Department of Mechanical Engineering

We certify that we have read this thesis and that in our opinion it is fully adequate in scope and quality as a thesis for the degree of Doctor of Philosophy in Mechanical Engineering.

Prof. Dr. Hasan Hacışevki
Supervisor

Examining Committee

1. Prof. Dr. Kahraman Albayrak

2. Prof. Dr. Şenol Başkaya

3. Prof. Dr. Hasan Hacışevki

4. Assoc. Prof. Dr. Hüseyin Çamur

5. Asst. Prof. Dr. Devrim Aydın

ABSTRACT

Wake structures as well as flow properties formed behind bluff bodies have received great interest among researchers for years. As a result of various application of bluff bodies in different engineering topics and industry, there has been a growing interest on this phenomenon. As a significant feature of these geometries has been the formation of various vortices in the wake, possible suppression of such phenomenon is the desired outcome in order to reduce the fluctuation forces act on the structures in civil engineering application. The Reynolds de-composition is a very common technique to approach these problems. However, some researchers tackle such problems with an alternative technique known as the triple decomposition. Since the flow structure of a bluff body comprises large-scale organized motion, the time-varying component in the wake region of a bluff -body flow consists of a periodic component (coherent structure) that can be distinguished from a random (incoherent) component. In the present study, incoherent turbulent flow structures in the near-wake region downstream of a square cylinder have been studied by employing triple decomposition. It was observed that the main incoherent turbulent kinetic energy production occurs in the region with the same width of square cylinder. Moreover, it was demonstrated that while a vortex is developing from one edge with maximum incoherent streamwise stress, the initiated shear layers from the other edge exhibit a maximum in incoherent transverse stress production.

In addition, wake region behind three modified geometries namely Circular Cylinder (CC), Semi Circular Cylinder (SC) and C shape (CS) are investigated experimentally and numerically for Re of 20000 to identify the effects of shape modification on the

wake region. These effects have been discussed in regards to flow structure, Turbulent Kinetic Energy (TKE), pressure and vorticity. It was observed that while CC and SC demonstrated almost similar level of TKE peak value with just 6% rising on SC, CS wake region exhibit a significant increase of 40% in the peak value with respect to CC. It was also illustrated that the vorticity in the wake region of SC is mostly concentrated along the edges of separated shear layers.

Keywords: Coherent Flow Structure, Incoherent Flow Structure, Vortex Shedding, Suppression, Square Cylinder, Circular Cylinder (CC), Semi Circular Cylinder (SC), C shape Cylinder (CS)

ÖZ

Değişik şekilli cisimlerin arkasındaki akış özellikleri ve iz yapıları, yıllardır birçok araştırmacıyı büyülemiştir. Değişik şekilli cisimlerin mühendislik ve endüstride çeşitli uygulamalarının bir sonucu olarak, bu olguya artan bir ilgi vardır. Bu cisimlerin önemli bir özelliği, iz bölgesinde girdap sokağı oluşması olduğundan, bu fenomenin olası bastırılması istenen bir sonuçtur. Reynolds ayrıştırması bu problemlere yaklaşmak için çok yaygın bir tekniktir. Bununla birlikte, bazı araştırmacılar, üçlü ayrıştırma olarak bilinen alternatif bir teknikle bu tür sorunları çözmektedir. Bir değişik şekilli cismin gövdesinin akış yapısı büyük ölçekli organize hareket içerdiğinden, bir değişik şekilli cisim akışının iz bölgesindeki zamanla değişen bileşen, rastgele (tutarsız) bir bileşenden ayırt edilebilen periyodik bir bileşenden (tutarlı yapı) oluşur. Bu çalışmada, kare bir silindirin akış aşağısında uyanmaya yakın bölgedeki tutarsız türbülanslı akış yapıları üçlü ayrıştırma kullanılarak incelenmiştir.

Ana tutarsız türbülanslı kinetik enerji üretiminin aynı genişlikte kare silindire sahip bölgede meydana geldiği gözlemlendi. Ayrıca, maksimum tutarsız akış yönünde gerilme ile bir kenardan bir girdap gelişirken, diğer kenardan başlatılan kayma katmanlarının tutarsız enine gerilme üretiminde bir maksimum sergiledikleri gösterilmiştir.

Ayrıca, şekil değişikliğinin iz bölgesi üzerindeki etkilerini belirlemek için Re=20000 için Dairesel Silindir (CC), Yarı Dairesel Silindir (SC) ve Dairesel Kabuk (S) olmak üzere üç değiştirilmiş geometrinin arkasındaki iz bölgesi deneysel ve sayısal olarak incelenmiştir.

Bu etkiler akış yapısı, TKE, basınç ve girdap açısından tartışılmıştır. CC ve SC'nin SC'de sadece %6'lık bir artışla hemen hemen benzer düzeyde TKE tepe değeri gösterdiği gözlenirken, S iz bölgesinin CC'ye göre tepe değerinde %40'lık önemli bir artış gösterdiği gözlemlendi. SC'nin iz bölgesindeki girdaplığın çoğunlukla ayrılmış kesme tabakalarının kenarları boyunca yoğunlaştığı da gösterilmiştir.

Anahtar Kelimeler: Girdap Atma, Bastırma, Tutarsız Akış Yapısı, Tutarlı Akış Yapısı, Kare Silindir, Dairesel Silindir (CC), Yarı Dairesel Silindir (SC), Dairesel Kabuk (S)

To My Family

ACKNOWLEDGMENT

It’s a great pleasure to thank my supervisor Prof. Dr. Hasan Hacışevki, who encouraged me in every condition of my life both for my carrier and academic life to develop my skills and be a successful person.

On the other hand, I would like to thank my Maman Sahar and Peyman, because of the uninterrupted spiritual help and for not leaving me alone at any stage of my life. Also, I am grateful to have such a cute grandma who was the spark of my journey to study abroad and supporting me every second of my life.

Finally, I thank my beautiful and elegant sister Perinaz for trusting me and the many efforts she makes, as well as not leaving my family alone for the time I was away.

T ABLE OF CONTENTS

ABSTRACT iii

ÖZ v

DEDICATION vii

ACKNOWLEDGMENT viii

LIST OF TABLES xii

LIST OF FIGURES xiii

LIST OF SYMBOLS AND ABBREVIATIONS xvi

1 INTRODUCTION 1

1.1 Vortex Shedding 1

1.2 Historical Review 2

1.3 Literature Review on Vortex Shedding Behind Bluff Body 4

1.3.1 Bluff Body Shapes 4

1.3.2 Wake Control Around Bluff Body 5

1.3.3 Vortex Shedding Behind Finite Curvature Structure 5

1.3.3.1 Circular & Elliptical Cylinder 5

1.3.4 Vortex Shedding Behind Sharp-Edged Structures 10

1.3.4.1 Square Cylinder 10

1.3.4.2 Triangular Cylinder 13

1.3.5 Sharp-Edged Structures and Finite Curvature Structure 14

1.3.5.1 D Shape Cylinder 14

2 THEORETICAL DERIVATIONS 16

2.1 Introduction 16

2.2 Triple Decomposition Technique 17

2.3 Time Averaging and Rules 18
2.4 Phase Averaging 18
2.5 Modified Navier-Stokes Equation 19
3 EXPERIMENTAL FACILITY AND DATA ANALYSIS 22
3.1 The EMU Subsonic Wind Tunnel 23
3.2 Hot-wire Anemometry 24
3.2.1 Hot Wire Probe 25
3.2.2 HWA Principle 26
3.2.3 Hot Wire Instrumentation 28
3.2.4 Hot Wire Calibration 29
3.2.5 Hot Wire System Settings 32
3.3 Hot Wire Probe Traverse Mechanism 32
3.4 Data Analysis Program Code 33
4 APPLICATION OF TRIPLE DECOMPOSITION TECHNIQUE ON NEAR WAKE MEASURMENTS OF SQUARE CYLINDER 37
4.1 Summary 37
4.2 Experimental Results 38
4.2.1 Shedding Frequency and Strouhal Number 38
4.2.2 Time Averaged Results 40
4.2.3 Coherent Structure 42
4.2.4 Incoherent Structure 44
5 TURBULENT KINETIC ENERGY IN THE WAKE REGION OF MODIFIED CIRCULAR CYLINDERS 50
5.1 Summary 50
5.2 Experimental Setup 50

5.3 Results and Discussion 52
6 NUMERICAL STUDY ON FLOW CHARACTERISTICS IN THE WAKE REGION OF CIRCULAR CYLINDER, SEMI CIRCULAR CYLINDER AND C SHAPE CYLINDER 59
6.1 Summery 59
6.2 Numerical Methods 59
6.2.1 Governing Equations 59
6.2.2 Computational Domain and Grid 61
6.2.3 Turbulence Modelling 64
6.3 Results 65
7 CONCLUSION 83
7.1 Final Remark 83
7.2 Suggestions for future studies 85
REFERENCES 86

LIST OF TABLES

Table 1.0.1: Regime categorization for flow over circular cylinder 6

Table 1.0.2: Regime classification for flow over circular cylinder 7

Table 3.1: Hot wire sensors settings 32

Table 4.1: Verifing the strouhal number with published studies 39

Table 5.1: Frequency and strouhal number for different geometries..... 53

Table 6.1: Computed shedding frequencies, corresponding strouhal number, and drag coefficient 65

Table 6.2: Numerical and experimental frequency and strouhal no comparison..... 66

LIST OF FIGURES

Figure 1.0.1: Free water flow as a turbulent flow from a square channel into a pool (Gad-El-Hak, 1998) 3

Figure 1.0.2: flow diagram beyond circular cylinder representing (a) without bubble, (b) bubble at the top, (c) bubble at the bottom, and (d) 2-bubble conditions. (Desai, Mittal, & Mittal, 2020). The representation on every condition, proposed by(Cadot et al., 2015). 9

Figure 2.1: Mean, coherent and turbulent velocity components of periodic instantaneous velocity 17

Figure 3.1: Side view of the subsonic wind tunnel 23

Figure 3.2: Single Hotwire probe Model 1210 25

Figure 3.3: Cross Hotwire probe Model 1240 25

Figure 3.4: Calibration curve plot for single probe SN 961171..... 27

Figure 3.5: Hot wire anemometry system configuration (Figure taken from TSI Flow Point 1500 Instruction Manual) 28

Figure 3.6: Schematic diagram of a thermal anemometer system (Wheatstone bridge) 29

Figure 3.7: Calibration curve plot for single probe..... 31

Figure 3.8: Calibration curve plot for Cross probe 31

Figure 3.9: Schematic of hotwire probe traverse mechanism 33

Figure 3.10: Simulink diagram of filtering program..... 34

Figure 3.11: Acquired unfiltered (Top) and filtered (Bottom) velocity signal 34

Figure 4.1: Experimental setup 38

Figure 4.2: Spectral analysis for various x/D behind cylinder..... 39

Figure 4.3: Streamwise time averaged velocities 41
Figure 4.4: transverse time averaged velocities 41
Figure 4.5: Time averaged incoherent normal Reynolds stress 42
Figure 4.6: Coherent streamwise velocity component for different x/D's 43
Figure 4.7: Coherent transverse velocity component for different x/D's 44
Figure 4.8: Incoherent turbulent kinetic energy for different x/D's behind square cylinder 45
Figure 4.9: Incoherent streamwise Reynolds stress at various x/D 46
Figure 4.10: Incoherent transverse Reynolds stress at various x/D behind square cylinder 47
Figure 4.11: Stream wise phase averaged velocity at x/D =0.5 and x/D =2.0 48
Figure 4.12: Transverse phase averaged velocity at x/D =0.5 and x/D =2.0 48
Figure 5.1: Experimental setup and coordinate system (top view) 51
Figure 5.2: Modified cylinder geometries (t=3mm) 52
Figure 5.3: Spectral analysis for various x/D behind semi circular cylinder 53
Figure 5.4: Coherent Turbulent Kinetic Energy 55
Figure 5.5: Incoherent TKE measured at different x/D behind the Cylinders 57
Figure 5.6: Time averaged incoherent normal Reynolds stress (x/D=4.0) 58
Figure 6.1: Flow domain of circular cylinder 62
Figure 6.2: The computational mesh for circular cylinder with 38400 nodes and 74928 elements 63
Figure 6.3: The computational mesh for semi circular and C shape 64
Figure 6.4: Instantaneous streamwise velocity behind the CC 67
Figure 6.5: Instantaneous streamwise velocity behind the SC Cylinder 68
Figure 6.6: Instantaneous streamwise velocity behind the CS Cylinder 69

Figure 6.7: Average streamwise velocity behind circular cylinder and the modified bodies 70
Figure 6.8: Instantaneous transverse velocity behind the CC 71
Figure 6.9: Instantaneous transverse velocity behind the SC cylinder 72
Figure 6.10: Instantaneous transverse velocity behind the CS cylinder 73
Figure 6.11: Instantaneous pressure behind the CC 74
Figure 6.12: Instantaneous pressure behind the SC cylinder 75
Figure 6.13: Instantaneous pressure behind the CS cylinder 76
Figure 6.14: Average pressure field behind the modified bodies 77
Figure 6.15: Instantaneous TKE behind the CC 78
Figure 6.16: Instantaneous TKE behind the SC cylinder 79
Figure 6.17: Instantaneous TKE behind the CS cylinder 80
Figure 6.18: Instantaneous vorticity behind the modified cylinders at time=0.16s ... 81
Figure 6.19: Time histories of Cd and Cl value of CC and S cylinder 82

LIST OF SYMBOLS AND ABBREVIATIONS

CCA	Constant Current Anemometer
CTA	Constant Temperature Anemometer
L	Square Cylinder Width [mm]
HWA	Hot Wire Anemometer
MSE	Mean Square Error
R_w	Wire Resistance [Ohm]
R_e	Reynolds Number (uD/ν)
Sn	Single Normal Probe
S_t	Strouhal Number (fD/U_∞)
S_t^*	Modified Strouhal Number (fD'/U_∞)
U	Stream-Wise Direction Velocity [M/S]
$\bar{u}$	Time Mean Velocity Component [M/S]
u'	Incoherent Velocity Component [M/S]
$\tilde{u}$	Coherent Velocity Component [M/S]
V	Transverse Direction Velocity [M/S]
X	Stream-Wise Direction
Y	Transverse Direction
α	Angle of Attack
f	Vortex Shedding Frequency [Hz]
ν	Kinematic Viscosity [M^2 / S]
< >	Phase Averaging
$\sigma_k, \sigma_\omega, \sigma$	Diffusion Constant of the k-ω Model

α_1, α_2	Constant in the SST Limiter
F_1, F_2	Blending Function
k	Turbulent Kinetic Energy
ω	Specific Dissipation Rate
ρ	Density
ν	Viscosity
S	Invariant Measure of the Strain Rate
y	Distance to the Nearest Wall
P_k	Production Limiter
y_1	First Layer Thickness
y^+	Non-Dimensional Measurement of Distance from a Wall

Chapter 1

INTRODUCTION

1.1 Vortex Shedding

Vortex shedding is a phenomenon, after the fluid is blowing across a bluff body (term bluff body describe geometries such as; rectangular or circular cylinder, flat plate, and etc.), vortices start to shed from one side of the body to other side periodically and then forming Von Karman Vortex Street. Low-pressure zones are generated on downstream of the structures and increase the fluctuating forces acting at right angles to the wind directions. Vortex shedding occurs over a comprehensive range of Reynolds numbers, and resulting severe structural vibration, acoustic noise and resonance, and significant increase in the mean drag and lift. Therefore, it is important to have effective control on vortex shedding in engineering application.

Researchers are working on the flow structure in the wake region, vortex shedding behind bluff body, and analysis of flow separation for almost four decades. The curiosity of these topics has been started due to practical and fundamental significance in aerodynamics and hydrodynamics applications. Examples that can be mentioned such applications are vibration of pipelines lying on the sea bottom under influence of currents and waves, bridges, suspension of chimneys and bridges near tall buildings, interaction of currents and waves with offshore structure, and destructive effects on the structure of cooling tower and sky scrapers (Rashidi, Bovand, Pop, & Valipour, 2014; Rashidi, Nouri-Borujerdi, Valipour, Ellahi, & Pop, 2015; Zang & Gao, 2014;

Zang, Gao, & Cui, 2013). On the other hand, unsteady loading phenomena have been investigated on various geometries (Circular, Triangle, Square, and etc.) and arrangements such as tandem, staggered, and etc. (Hacışevki & Teimourian, 2015, 2016; Irwin, 2008a). Even, small modification on geometries can affect on the wake structure such as round edges on the edges of the bluff body. Despite to these contrasts, flow around bluff bodies feature a common flow structure development in the wake region. The flow on the wake is characterized by time-averaged velocity, velocity fluctuations, and flow structure.

In this dissertation vortex suppression on the wake of the bluff bodies have been studied experimentally and numerically by employing passive flow control. Coherent and incoherent flow structures as well as time averaged properties have been used to find out the wake region behavior. The effectiveness of the employed method and delay of the vortex street in the wake region behind the geometry have been studied.

1.2 Historical Review

The behavior of the fluid flow which passed around an obstacle is determine by Reynolds number. Steady flow and vortices appear in the range of $102 \leq Re \leq 105$, and finally turbulent flow emerge when the Reynold number is greater than 105. Turbulent flows are very complicated so that the speed of the fluid at a specific point is changing continuously in both magnitude and direction, they have been considered as the majority of natural flow and industrial applications. Even the flow in the river with gentle currents are turbulent. However, despite the observations of variety of turbulent flows, it is not easy to state a precise definition for turbulence. Instead it is possible to define turbulent flow in terms of its characteristics (Tennekes, Lumley, & Lumley, 1972).

Leonardo da Vinci has been sketched the fluid flow from square channel into a pool around 500 years ago as it has shown in Figure 1.1. He is known as a pioneer of the flow visualization, and has been observed that surface of water has two motions, one by the weight and another one by the direction of curl. After three centuries Osborne Reynolds proposed Reynolds-averaging of turbulent flows, where velocity components are expressed as the summation of mean and fluctuating components.

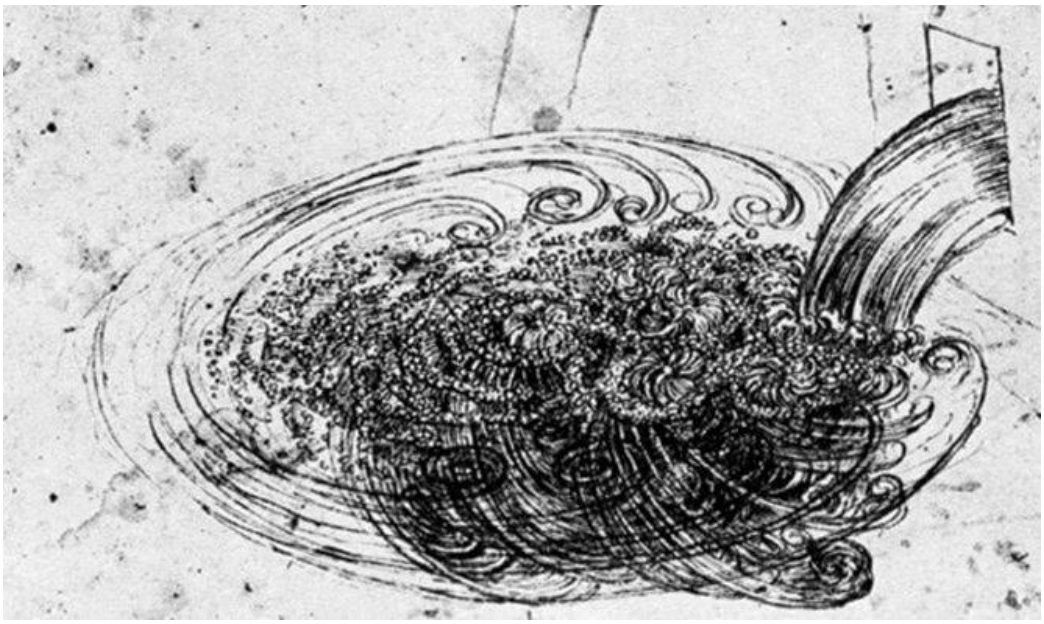

Figure 1.0.1: Free water flow as a turbulent flow from a square channel into a pool (Gad-El-Hak, 1998)

The first vortices have been discovered by Henri Benard the French physicist in 1904 after he built the water tank in the University of Lyon. The observation of the next experience of Benard had a strong impact in the way that most of famous scientists such as Theodore von Karman have cited his papers in his 1911 and 1912 papers.

At the end, the correlation between periodic flow of wire and the velocity passing over it have been revealed by Vincenc Strouhal a Czech physicist. Thus, for periodic vortex shedding behind bluff body, multiplication of the frequency which vortices are being

shed with characteristic length over free stream velocity are express a dimensionless term called Strouhal Number.

1.3 Literature Review on Vortex Shedding Behind Bluff Body

Observation of the flow characteristics on the wake of bluff body is one of the major problems in fluid mechanics due to wide range of parameters that effect on it. Also, there are many applications in engineering field for the flow around a bluff body like: bridges, road vehicles, urban structures, cooling towers, and etc. Therefore, this topic has been received the interest of scholars for research about the problems such as: delaying the separation, reduce the aerodynamic drag, increasing the aerodynamic lift, and suppression of the vortex shedding.

1.3.1 Bluff Body Shapes

In the field of aerodynamics, geometries are divided into two main categories. Streamlined bodies that the drag is dominated by viscous drag and bluff bodies which drag is dominated by pressure drag. However, the use of each structure varies according to their application. For instance, the geometries are divided aerodynamically into three different types:

1- Continues and finite curvature structure.

2- Sharp edged structures with infinitely large curvature.

3- A combination of 1 and 2.

The circular, square, rectangular, and triangular cross-sectional shapes are the most classic bluff bodies that scholars are investigating about flow structure, vortex formation in the wake, and etc. both experimentally and numerically.

Various flow factors such as Stagnation point, separation region, shear layers, vortex

shedding, circulation flow, vortex pattern, vortex formation length, wake breadth, shedding frequency, and phenomena establish the fundamentals of flow attributes Strouhal number St =fD/U is used to normalize the shedding frequency, where f (Hz) is representing the vortex shedding frequency, the diameter or length scale of the bluff body is D (m), while the free stream velocity is U (m/s).

Vortex-induced Vibration (VIV) is affected by vortex formation and due to the vibration, the structure obtains the flow's energy in every oscillation cycle. The fluctuating forces on the wake are the main concern for design in industrial systems because of destructive effects on the structure. In the literature there are many studies about vortex shedding with different geometries and different condition.

A large number of researches on bluff bodies have paid interest on the flow around a circular cylinder with a diameter of D, while paying less attention on that around a square cylinder (of side length, D).

1.3.2 Wake Control Around Bluff Body

In order to control destructive behavior of wake and suppress the vortex shedding behind bluff body, scholars have been found several methods such as: Active control method, passive control method, and control vortex shedding by employing an external element

1.3.3 Vortex Shedding Behind Finite Curvature Structure

1.3.3.1 Circular & Elliptical Cylinder

Circular cylinder is one of the outstanding bluff bodies that has been considered by scholars in fluid dynamics field for a long time. Due to its extensive usage in the nature and industrial application, there are significant number of studies about this shape to investigate different flow characteristics such as flow separation, vortex suppression, flow structure, separation delay, and etc. downstream in the wake both numerically

and experimentally. According to the (Roshko, 1954) study the flow downstream of a circular cylinder is divided by four different periods based on Reynolds number that have been present in Table 1.1.

Table 1.0.1: Regime categorization for flow over circular cylinder

Category item	**Reynolds domain**	**Region**
1	$Re < 2 \times 10^5$	Subcritical
2	$2 \times 10^5 \leq Re \leq 5 \times 10^5$	Critical
3	$5 \times 10^5 \leq Re \leq 5 \times 10^6$	Supercritical
4	$Re > 5 \times 10^6$	Trans-critical

For the subcritical regime, early separation occurred due to the laminar boundary layer on the circular cylinder shape. For the critical regime, the region called "Laminar Separation Bubble" (LSB) is appeared because, the separated boundary layer is transmitted to a turbulent mood immediately and reattach to the surface of the cylinder again (Behara & Mittal, 2011; Chopra & Mittal, 2017; Singh & Mittal, 2005). For the supercritical regime, as the Re increase the transition location moves gradually to the upstream and also the drag force rise moderately.

On the other hand, (Achenbach & Heinecke, 1981) break down the subcritical regime into four different periods with a little difference on the periods and presented in Table 1.2. based on visual remarks of the changes in *St* with *Re* and the flow structure.

Table 1.0.2: Regime classification for flow over circular cylinder

Category item	**Reynold's domain**	**Region**
1	$Re < 1$	Creeping flow
	$3\text{-}5 < Re < 40\text{-}48$	Steady separated
	$40\text{-}48 < Re < 300$	Periodic laminar wake
2	$300 \leq Re < 1.4 \times 10^5$	Subcritical
3	$1.4 \times 10^5 \leq Re < 1 \times 10^6$	Critical
	$1 \times 10^6 < Re < 5 \times 10^6$	Supercritical
	$Re > 5 \times 10^6$	Transcritical

Vortex shedding is one of the main phenomena in the wake of bluff body that most of the researchers are curious about it. (Derakhshandeh & Alam, 2019) have presented an extensive review on the bluff body wakes for different kind of geometries. An experimental study have been made by (Nishimura & Taniike, 2001) about the flow over a circular cylinder in the subcritical regime ($Re=6x10^4$). They have observed that the fluctuation of the lift force has been synchronized with the movement of separation and stagnation locations. (Schewe, 1983) conducted an experimental study from subcritical to transcritical Reynolds number ($2.3 \times 10^4 < Re < 7.1 \times 10^6$) in order to measure the force fluctuation on the circular cylinder. He observed two discontinuous transitions in the critical Reynolds number regime. Furthermore, he observed that both transitions lead to reduce the non-dimensional drag coefficient (CD) dramatically and escalate of the Strouhal number. A numerical investigation has been carried out by (Yeon, Yang, & Stern, 2016) by implementing a method namely Large Eddy Simulations (LESs) for two different Re regions which are the subcritical and supercritical to inspect the effect of the Aspect Ratio (AR) of the circular cylinder and the grid size to the sensitivity of flow. They have come to the conclusion that, for sub

and super critical Reynolds number cases the large aspect ratio and small aspect ratio is required respectively. According to the experimental study conducted by (So & Savkar, 1981) within sub-super critical Reynolds number regime on a circular cylinder, in the critical region the fluctuation forces are numerously varied with an increase in the free stream turbulent intensity. On the other hand, these changes are not significant in the subcritical region.

The fluctuation lift reduction, as well as progressively arbitrary behavior towards the end of the subcritical Re region was noticed by (Blackburn & Melbourne, 1996; Cadot, Desai, Mittal, Saxena, & Chandra, 2015; Schewe, 1983) between the others. An experimental study by implementing the two popular methods namely Time Resolved PIV (TRPIV), and Detached Eddy Simulation (DES) techniques at high Reynolds number have made by (Perrin et al., 2009). They provided a physical analysis of structural properties of turbulence affected by the coherent structure motion. Also, the other important result observed at $Re=1.4 \times 10^{5}$ is the dispersion of the strong vortex shedding with the explosion of weaker vortex shedding.

Furthermore, the effect of small deviations during the experiment such as the surface roughness as well as free stream on the critical regime presented by (Achenbach & Heinecke, 1981; Farell & Blessmann, 1983). The dynamics of turbulent reattachments at the time of drag crisis perused by (Cadot et al., 2015). The four most possible conditions of the flow in the critical region presented by them such as:

I. There is no laminar separation on the cylinder (Presented by #0),
II. The laminar separation appeared at the top surface (#1t),
III. The laminar separation appeared at the bottom surface (#1b),
IV. The laminar separation appeared at both top and bottom surfaces (#2).

That is shown in Figure 3. LS, TS, and TR observations are stand for Laminar Separation, Turbulent Separation, and turbulent Reattachment, respectively.

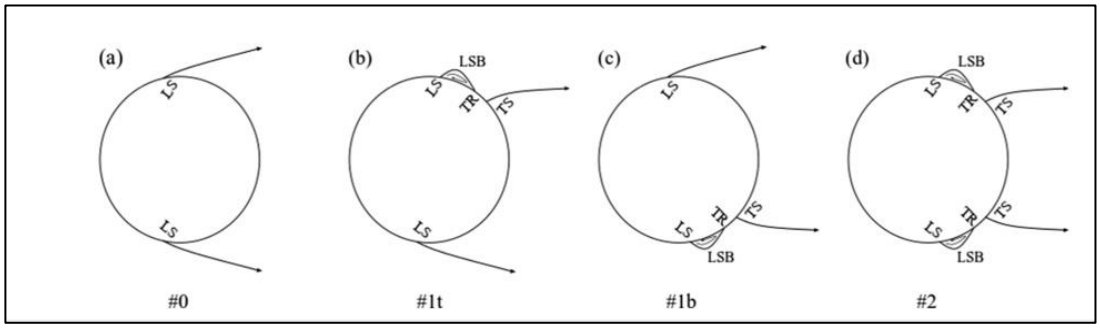

Figure 1.0.2: flow diagram beyond circular cylinder representing (a) without bubble, (b) bubble at the top, (c) bubble at the bottom, and (d) 2-bubble conditions. (Desai, Mittal, & Mittal, 2020). The representation on every condition, proposed by(Cadot et al., 2015).

According to Figure 1.2, both cases (b) and (c) are commonly known as "one bubble stage", and case (d) is known as "two bubble state" (Lehmkuhl, Rodríguez, Borrell, Chiva, & Oliva, 2014; Lin, Miau, Tu, & Tsai, 2011; Schewe, 1983). They observed that there are different possibilities for these states according to the flow and reattachments accrue randomly. Initially, the flow stays on (0#) stage in the critical regime. Then, within the first transition during the experiment, the flow changes the phase to without bubble, bubble at the top side and bubble at the bottom side stages incidentally and finally stabilized on the one bubble (Top side) state. For the next transition, the flow changes periodically between (#1t) and (#2) just before the last stabilizing at #2. They have observed the symmetrical structure right after replacing the angle of attack where the one bubble stage was bypassed for cylinder.

In addition, (Ozgoren, 2006) investigated flow structure in the wake of circular and square cylinder at incident angle of 45 degree. The Strouhal numbers observed to be in range St=0.204–0.212 and, St=0.12–0.134 for the circular cylinder and the square

cylinder respectively. Also, according to his investigation the range of Strouhal number for square cylinder at incidence is between St=0.165–0.174. The vortex shedding frequency in the wake region of elliptical and square cylinders studied by {Knauss, 1976 #190}{Knauss, 1976 #190}D. T. Knauss, J. John, and C. Marks (1976). It was reported that while Strouhal number depended on the geometrical shape of the bluff body, but almost independent of Reynolds number. In addition, Ozgoren, Pinar, Sahin, and Akilli (2011) and Provansal, Schouveiler, and Leweke (2004) investigated flow characteristics in the wake region behind circular cylinder and sphere. The study demonstrated that due to the three-dimensional flow over the sphere, it was more complex than the wake flow of the circular cylinder. Furthermore, sphere exhibit higher vortex shedding frequency, while circular cylinder demonstrates higher PSD. It was also reported that turbulence kinetic energy peak in the wake of circular cylinder is 3 times higher than peak values in wake of sphere. Cantwell and Coles (1983) studied the entrainment process in the turbulent wake of a circular cylinder. They described the kinematics of the vortex-formation process in terms of the formation and evolution of saddle points between vortices in the near wake. They reported that entrainment was found to be closely associated with saddles and to be concentrated near the upstream-facing interface of each vortex.

1.3.4 Vortex Shedding Behind Sharp-Edged Structures

1.3.4.1 Square Cylinder

The creation of vortices in the downstream wake is one of the most notable aspects of flow surrounding these bodies. Such an uneven wake could result in uneven loading, causing vortex-induced vibration to damage the construction of skyscrapers, cooling towers, chimneys, and bridges, all of which are vital to civilization. This phenomenon is not only the main concern during design stages of industrial systems but also in

service. Different configurations and bodies which include staggered, tandem, as well as other configurations have been investigated with an aim of identifying the unsteady loading behaviour which has been found out to resemble different engineering applications in civil or aerospace industry for instance (Hacışevki & Teimourian, 2015, 2016; Irwin, 2008b; Taylor, Gurka, & Kopp, 2014; Zdravkovich, 1997).

Teimourian, Hacisevki, and Bahrami (2017) used triple decomposition to investigate on the vortices behind two flat plates in tandem at an angle. A sequence of counter vortices with differing coherent intensity is shed alternately from the leading edge and trailing edge of the plates, as shown in the observed coherent structure. TKE contours demonstrated that the maxima was localized near the borders of the partitioned shear layer, corresponding to vortex shedding from the plate edges. Çuhadaroğlu and Turan (2009) investigated the wake region behind a square cylinder by employing triple decomposition numerically. While Rodi (1993) investigated calculation of vortex shedding flow for various turbulence models together with triple decomposition, Çuhadaroglu (2009) and Çuhadaroğlu and Turan (2009) studied on the turbulent flow around a square cylinder. Çuhadaroglu (2009) and Çuhadaroğlu and Turan (2009) demonstrated the effects of uniform injection or suction through a porous square cylinder on the flow field and on aerodynamic parameters and Strouhal number. Their numerical results show that the vortex shedding phenomenon becomes weaker due to the suction through top and bottom surfaces of the square cylinder. Hacışevki and Teimourian (2015) have been made a comparison study about the wake region between a square cylinder and flat plates in tandem. They observed a lower Strouhal number in wake region behind square cylinder than the wake region of tandem plates. This research intended to study possible similarities of the wake region features. To identify flow similarities the wake region has been studied in terms of vortex shedding

frequency, coherent structures and a quantitative comparison for variation of Turbulent Kinetic Energy (TKE) have been presented. Moreover, (Bosch & Rodi, 1998) carried out numerical study on vortex shedding over square cylinder for various turbulence models. They observed that the numerical details in the solutions of the procedure have a significant influence on the onset of the vortex shedding. But, after creation of the vortex shedding these details become less important for the calculation. (Minguez, Brun, Pasquetti, & Serre, 2011) performed numerical and experimental analysis over square cylinder for the near wall region. They have provided a comprehensive data set by use of Laser Doppler Velocimetry (LDV) and high-order large-eddy simulations (LES) approaches. Also, they observed the coherent flow structure that developed downstream and the sides of the cylinder. In addition, they found that the flow separation occurs at the leading edge of the cylinder with the incidence of three-dimensional Kelvin–Helmholtz (KH). A CFD study for unsteady flow passed a two dimensional square cylinder made by (Murakami & Mochida, 1995). They have compared the obtained 2D and 3D results and illustrated that the 3D results are equivalent to the experimental results but the 2D results are different with respect to experimental studies. (Dutta, Panigrahi, & Muralidhar, 2008) investigated the flow past a square cylinder with various angle of attack to the incoming flow experimentally with different methods such as: Hot wire Anemometry (HWA) with the use of probe, Particle Image Velocimetry (PIV) by implementing laser light, and flow visualization. They found the minimum time average drag coefficient and maximum Strouhal number at the angle of 22.5^{o}. They conclude that the reason of the low drag coefficient at this angle is the wake asymmetry due to the shear layers with various length on each side. In addition, (Saha, Muralidhar, & Biswas, 2000) conducted an experimental investigation by HWA for the flow over a square cylinder

for high Reynolds number. They observed that in the x=1.5 location there was a good association between vortex maxima and the turbulence shear stress.

1.3.4.2 Triangular Cylinder

Due to rising the computational power and development of new techniques in experimental investigation, there are several geometries such as triangular cylinder that received more attention for both numerical and experimental studies. Despite less attention given to the flow over triangular cylinder respect to the other geometries such as circular cylinder and square cylinder, there are several well studies that represent the flow over this cylinder. One of the clear instances of bluff body flow with a fixed separation point in the field of aerodynamic is the triangle cylinder (Zhang & Perot, 2000). Also, he mentioned that the Von Karman vortex street appears clearly for the Reynolds that are not too low but, for significantly high Reynold's flow over triangular cylinder the flow will be turbulent and turbulent model must be use. Furthermore, (Sjunnesson, Nelsson, & Max, 1991) conducted an experimental studies to measure the flow over triangle cylinder in the duct. On the other hand, Numerical study carried out by (Johansson, Davidson, & Olsson, 1993) for the flow over and downstream of triangular cylinder using k-ε model. (Durbin, 1994) conducted the same numerical study with k-ε-v^2 model as well. A finite element study for the beginning of vortex shedding for the flow past different bluff bodies have been made by (Jackson, 1987). According to this study, the critical Reynolds number and its corresponding Strouhal number for an isosceles triangle have reported as 34.318 and 0.13554 respectively. 2-dimensional numerical study on the wake of the equilateral triangular body with 1/15 blockage ratio carried out by (Zielinska & Wesfreid, 1995). The critical Reynold reported in this study was 38.3 which was confirmed by an experimental study conducted by (Wesfreid, Goujon-Durand, & Zielinska, 1996). (Abbassi, Turki, &

Nasrallah, 2001) conducted a numerical study on the laminar flow and heat transfer structure from a built-in triangular prism located in a channel. They observed that the transition between symmetric and periodic flow has occurred in the Reynolds of 45 with a blockage ratio of ¼.

1.3.5 Sharp-Edged Structures and Finite Curvature Structure

1.3.5.1 D Shape Cylinder

D-shape is one of the geometries that due to less applicable in industry it is much less extensive by scholars and it is worth noting that there are just few studies on this shape in the literature(Hourigan, Thompson, & Tan, 2001; D. T. Knauss, J. E. John, & C. H. Marks, 1976; Nishiyama, Ota, & Matsuno, 1988). (Gao, Li, Bai, & Wu, 2016) carried out an experimental investigation at subcritical Reynolds for effect of synthetic jets on a D-Shaped Cylinder wake. They have suppressed the large scale vortices at downstream of the D-shape Cylinder significantly by the perturbations of the synthetic jets. (Stalnov, Palei, Fono, Cohen, & Seifert, 2007) employed an experimental study to estimate the flow control by using body-mounted sensors in the wake of D-shape cylinder. In this study, they observed that the two modes of the flow field in the wake of the cylinder are accurate within 35% RMS error respect to the POD measurements of time coefficients RMS. Moreover, (Meliga, Pujals, & Serre, 2012) analysed the sensitivity of the turbulent flow passed a semi-circular cylinder at Reynolds of 13000 by adjoint-based gradient. The two dimensional, Reynolds averaged Navier-Stokes obtained result compared with the experimental data presented by (Parezanovic & Cadot, 2012) and suggested that the control cylinder acts independently with an aid of local modification of the mean flow profiles.

As a result, there are three different groups of structures such as finite curvature structures, sharp-edged structures, and the combination of them. There are numerous

studies that have been made by scholars about these structures with different conditions. For instance, studies of a single geometries with different Reynolds region, same geometries in tandem with a same Reynolds number and different gap ratio and etc. In this study, triple decomposition technique has been used rather than classical Reynolds decomposition to distinguish the incoherent turbulent flow fluctuation from coherent vortex shedding structure for a better understanding of this phenomena. Also, numerical study have been employed in order to illustrate the flow characteristics on the circular cylinder and its modified geometries.

Chapter 2

THEORETICAL DERIVATIONS

2.1 Introduction

Triple decomposition and ensemble averaging technique have been used to investigate the vortex shedding behind the bluff bodies. These techniques have been proposed by many scholars (Perry & Steiner, 1987; Reynolds & Hussain, 1972). Although, turbulent flow and vortex shedding which known as incoherent turbulent fluctuations and coherent structure respectively, could be resulted in a better understanding of the phenomena.

Since vortex shedding is a periodic flow, therefore it is more appropriate to analyze these types of signals by use of phase averaging technique. Phase averaging technique is one of the methods to decompose the measured time varying signal u(t) into fluctuating part and mean part for the periodic unsteady flow (Enotiadis, Vafidis, & Whitelaw, 1990; Tiederman, Privette, & Phillips, 1988).

The techniques that applied on the momentum equations such as: phase averaging technique, triple decomposition, and ensemble and modification of Navier Stokes equations have been derived accordingly in this chapter. Although, additional stress terms due to coherent structure and incoherent fluctuation can be investigate as well. Several properties have been explained in this chapter like: coherent and incoherent stresses term, turbulent kinetic energy (TKE) and other terms that are examined in the

result chapter for different bluff body geometries.

2.2 Triple Decomposition Technique

Since triple decomposition technique come up with an improved explication of incoherent turbulent fluctuation and coherent structure therefore, have been used to analyze flow properties such as instantaneous velocity. This method decomposing instantaneous stream wise velocity u as follow:

$$u(\vec{x},t) = \bar{u}(\vec{x}) + \tilde{u}(\vec{x},t) + u'(\vec{x},t) \quad (2.1)$$

Where $\bar{u}$, $\tilde{u}$, and u' are the time-mean is averaged component, periodic coherent structure, and random fluctuation incoherent structure respectively. The above expression can employ for any velocity components i.e., transverse velocity or product of velocity components like Reynold normal or shear stresses.

Mean velocity and instantaneous velocity for one period of alternation overlapped with coherent and incoherent random fluctuation have been shown in Figure 2.1.

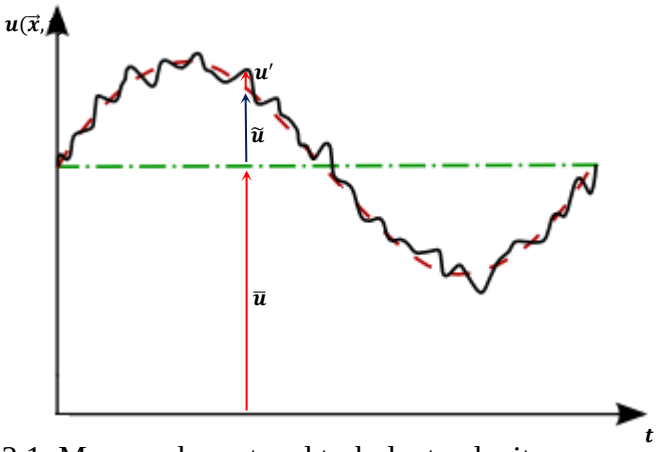

Figure 2.1: Mean, coherent and turbulent velocity components of periodic instantaneous velocity

2.3 Time Averaging and Rules

The time average of incoherent fluctuation u' and v' are zero because of their random nature. Therefore:

$$\overline{u'} = 0$$

$$\overline{v'} = 0$$

Furthermore, the other rule that have mentioned about the periodic vortex shedding is that the time average of coherent structure is zero as they have shown in the following:

$$\tilde{\bar{u}} = 0$$

$$\tilde{\bar{v}} = 0$$

The additional averaging rules have been employed to deduce the modified Navier Stokes equation by (Reynolds & Hussain, 1972) as researchers are referred. Accordingly, (Bradshaw, 2013) have shown that the time average of any flow property like velocity is calculated as:

$$\bar{u} = \frac{1}{T}\int_0^T u(x,t)dt \tag{2.2}$$

Because of the cyclic nature of the shedding phenomenon, $\bar{u}$ is not depending on the time.

2.4 Phase Averaging

There are several methods available to phase average the natural oscillating flow field. These methods are contained of two main groups of physical and mathematical. The physical model is based on the time-resolved measurement signal to define the oscillation period clearly. However, mathematical models are just depending on the mathematical methods to associate the phase between randomly procured data.

To apply Phase averaging based on physical group for oscillating flow field, a reference signal is necessary due to the lack of an external trigger. The obtain signals

have to clearly reveal a single oscillation period. Consequently, the reference signal data has to be adequately higher than the oscillation frequency. Different sources of reference signals are available such as: Microphone, hotwire anemometry, pressure transducers, optical measurement techniques that in the next chapter the hotwire anemometer will be discuss in detail.

The aim of applying phase averaging method is to decompose instantaneous velocity and employ it to triple decomposition. This is a mean operation over consecutive terms same phase in each period. Thus, phase average is calculating by:

$$u(x,y,t) = \lim_{N\to\infty} \frac{1}{N} \sum_{n=1}^{N} u(x,y,t+nT) \tag{2.3}$$

Where N and u are the number of cycles used and the instantaneous velocity, respectively.

The phase averaging is defined as the average of enormous collection of points with same phase respect to the specified wave. As a result,

$$\tilde{u} = u - \bar{u} \tag{2.4}$$

The expression above shows that in phase averaging method the coherent oscillations are filters from the instantaneous turbulent motion.

2.5 Modified Navier-Stokes Equation

Navier Stokes momentum equation have been shown and specified by four terms as follow:

$$\frac{\partial u_i}{\partial t} + u_j \frac{\partial u_i}{\partial x_j} = -\frac{1}{\rho}\frac{\partial P}{\partial x_j} + \nu \frac{\partial^2 u_i}{\partial x_j \partial x_j} \tag{2.5}$$

(I) (II) (III) (IV)

Phase averaging has applied to each term and the results are shown as follow:

Term (I):

$$\frac{\partial\langle\bar{u}_i+\tilde{u}_i+u_i'\rangle}{\partial t}=\frac{\partial\langle\bar{u}_i\rangle}{\partial t}+\frac{\partial\langle\tilde{u}_i\rangle}{\partial t}+\frac{\partial\langle u_i'\rangle}{\partial t}=\frac{\partial\bar{u}_i}{\partial t}+\frac{\partial\langle\tilde{u}_i\rangle}{\partial t} \tag{2.6}$$

Term (II) from continuity can be written as $\frac{\partial(u_j u_i)}{\partial x_j}$

$$\therefore\quad \frac{\partial(u_j u_i)}{\partial x_j}=\frac{\partial}{\partial x_j}\left\langle(\bar{u}_j+\tilde{u}_j+u_j')(\bar{u}_i+\tilde{u}_i+u_i')\right\rangle$$

$$=\frac{\partial}{\partial x_j}\left\langle(\bar{u}_j\bar{u}_i+\bar{u}_j\tilde{u}_i+\bar{u}_j u_i'+\tilde{u}_j\bar{u}_i+\tilde{u}_j\tilde{u}_i+\tilde{u}_j u_i'+u_j'\bar{u}_i+u_j'\tilde{u}_i+u_j'u_i'\right\rangle$$

$$=\frac{\partial}{\partial x_j}\left(\bar{u}_i\bar{u}_j+\bar{u}_j\langle\tilde{u}_i\rangle+\bar{u}_i\langle\tilde{u}_j\rangle+\langle\tilde{u}_i\tilde{u}_j\rangle+\langle u_i'u_j'\rangle\right) \tag{2.7}$$

Term (III):

$$-\frac{1}{\rho}\frac{\partial\langle\bar{P}+\tilde{P}+P'\rangle}{\partial x_j}=-\frac{1}{\rho}\frac{\partial\langle\bar{P}\rangle}{\partial x_j}-\frac{1}{\rho}\frac{\partial\langle\tilde{P}\rangle}{\partial x_j}-\frac{1}{\rho}\frac{\partial\langle P'\rangle}{\partial x_j}$$

$$=-\frac{1}{\rho}\frac{\partial\langle\bar{P}\rangle}{\partial x_j}-\frac{1}{\rho}\frac{\partial\langle\tilde{P}\rangle}{\partial x_j} \tag{2.8}$$

And Term (IV):

$$\nu\frac{\partial^2\langle(\bar{u}_i+\tilde{u}_i+u_i')\rangle}{\partial x_j\partial x_j}=\nu\frac{\partial^2\langle\bar{u}_i\rangle}{\partial x_j\partial x_j}+\nu\frac{\partial^2\langle\tilde{u}_i\rangle}{\partial x_j\partial x_j}+\nu\frac{\partial^2\langle u_i'\rangle}{\partial x_j\partial x_j}$$

$$=\nu\frac{\partial^2\langle\bar{u}\rangle}{\partial x_j\partial x_j}+\nu\frac{\partial^2\langle\tilde{u}\rangle}{\partial x_j\partial x_j} \tag{2.9}$$

The final form of Navier Stokes momentum equation after employing the phase averaging on each term is written as:

$$\rho\frac{\partial\bar{u}_i}{\partial t}+\rho\frac{\partial\bar{u}_i\bar{u}_j}{\partial x_j}+\frac{\partial\bar{p}}{\partial x_j}-\frac{\partial}{\partial x_j}\left(\mu\frac{\partial\bar{u}_i}{\partial x_j}-\rho(\langle\tilde{u}_i\tilde{u}_j\rangle+\langle u'_i u'_j\rangle)-\rho\left(\bar{u}_i\langle\tilde{u}_j\rangle+\bar{u}_j\langle\tilde{u}_i\rangle\right)+\langle\tilde{p}\rangle\right)=0 \tag{2.10}$$

Eventually, time averaging will apply to the obtained equation (2.10) and modified Navier Stokes equation is presented as follows:

$$\rho\frac{\overline{D\bar{u}_i}}{Dt}=-\frac{\overline{\partial\bar{P}}}{\partial x_i}+\frac{\partial}{\partial x_j}(\mu\frac{\overline{\partial\bar{u}_i}}{\partial x_j}-\rho(\langle\overline{\tilde{u}_i\tilde{u}_j}\rangle+\langle\overline{u_i'u_j'}\rangle))+\frac{\partial}{\partial x_j}(\rho(\overline{\bar{u}_i\langle\tilde{u}_j\rangle}+\overline{\bar{u}_j\langle\tilde{u}_i\rangle})+\langle\overline{\tilde{P}}\rangle)$$

(2.11)

Accordingly:

$$\rho\frac{D\bar{u}}{Dt}=-\frac{\partial P}{\partial x_j}+\frac{\partial}{\partial x_j}(\mu\frac{\partial\bar{u}_i}{\partial x_j}-\rho(\overline{\tilde{u}_i\tilde{u}_j}+\overline{u_i'u_j'})) \tag{2.12}$$

As it has noticed from modified Navier Stokes formula that have observed previously by triple decomposition technique, there is an additional term of $\overline{\tilde{u}_i\tilde{u}_j}$ beside Reynold's stress term $u'v'$ that describe Reynold's stress term because of coherent fluctuation.

Furthermore, determination of the Turbulence Kinetic Energy (TKE) has been established in the same way and shown as following:

$$\bar{k}=\frac{1}{2}\overline{u_i'u_i'}=\frac{1}{2}(\overline{u_1'u_1'+u_2'u_2'+u_3'u_3'})=\frac{1}{2}(\overline{u'u'+v'v'+w'w'}) \tag{2.13}$$

Hotwire anemometry has been used in this study for different geometries in order to measure the downstream velocity by electrical current on the wake of bluff body and described in chapter 3.

The wake region has been carried out in terms of coherent velocities, normal and shear stresses and Turbulent Kinetic Energy production, for example. Detailed investigation coherent structure and suppression of vortex shedding also presented for square cylinder in chapter 4.

Chapter 3

EXPERIMENTAL FACILITY AND DATA ANALYSIS

A number of experiments have been conducted for this dissertation with an intention of finding out the effect of shape modification on vortex shedding and the flow formation. For clarity of the experiments, the procedure has been chronologically explained which include: measuring techniques, experimental facilities and data analysis.

The velocity and fluctuation components of the desired region in wake of the bluff body Hot Wire Anemometer (HWA) have been established by measurements. In addition, the working principle of the HWA and the calibration procedure of the sensors have been elaborated.

The cross mechanism of the cross sensor that identifies the Hot wire sensor in the wake of the geometry in its desired position in the wind tunnels test section has been explained.

The working theory of the HWA, its calibration and instrumentation processes, and the traverse mechanism utilized in crossing the Hot wire probe of the wind tunnel test section have also been elaborated.

3.1 The EMU Subsonic Wind Tunnel

All tests were carried out in an open-type, subsonic wind tunnel with a test segment measuring 0.5 m in height, 0.5 m in width, and 1.4 m in length and a contraction ratio of 10:1. This tunnel is housed in EMU's Mechanical Engineering Department's aerodynamic laboratory. The tunnel's maximum speed and free stream turbulent strength are 0.8 percent and 30 m/s, respectively. The tunnel set-up has been presented in Figure 3.1 with associated systems as A, B, C, D, E, F that represent Test Section, Traverse Mechanism, TSI 1500 Flow Point Velocity Transducer, Step motors controller main board, Frequency controller unit, Fan respectively. The suction fan motor <H> speed was precisely controlled with a 12 kW Danfoss <E> electronic frequency control unit (0–50 Hz). Air is sucked into the tunnel by means of a 110 cm diameter fan <F> which was located at the exit section of the tunnel. To reduce the free stream turbulence level and swirling of the flow due to spinning of the fan blades, a nacelle < I > was installed upstream of the fan blades.

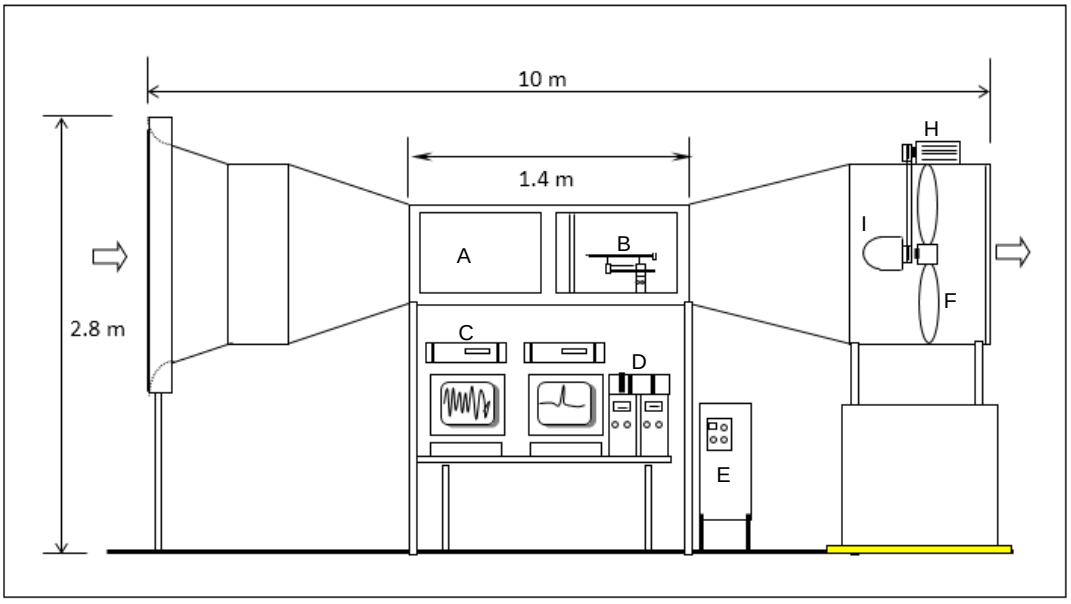

Figure 3.1: Side view of the subsonic wind tunnel

3.2 Hot-wire Anemometry

The hot wire anemometer (HWA) is among the most systematic method for measuring the instantaneous flow velocity behind a bluff body in turbulent flow measurements. Electric voltage measurements by a hot-wire anemometer are used to determine velocity. The high spatial resolution and perfect frequency response properties of this approach distinguish it from others. The technology achievement in the late 1950's leads to development of an accurate technique in flow measurements. This newly developed technique was superior in accuracy and flexibility compare with available flow measurements technique such as Pitot tube measurements (Bruun, 1996). However, this technique can be used in situations where a high-frequency response is needed. However, since the probe must be positioned in the flow sector, the HWA technique has some limitations. It's a live wire the sensors on anemometers are delicate and sensitive to dirt and dust in the flow. Furthermore, each sensor must calibrate before and after each experiment in order to make an accurate measurement. Constant Current Anemometer (CCA) mode and Constant Temperature Anemometer (CTA) mode are the two types of hotwire anemometers available (CTA). The "Constant Current" types operate in order to maintain a constant current through the sensing feature. The "Constant Temperature" styles, on the other hand, use an electrical control unit to try to maintain a constant temperature in order to alter the current as a result. To summarize, the working principles of the two approaches discussed are vastly different. Despite the circuit's complexity and the funds available, the CTA models are simpler to use and have less noise issues. Nonetheless, as (Bradshaw, 2013) said, CTA is the most common form and is referred to as standard. In this study the CTA model have been used for all experiments.

3.2.1 Hot Wire Probe

Hot-wire and hot-film probes are the most popular probes used in hot wire anemometers. These sensors assist turbulent flow studies, and it is preferred that the sensor's dimensions be based primarily on the Kolmogorov length scale of the smallest eddies to provide precise measurements of turbulent flow. (Bradshaw, 1996).

The hot wire sensor is composed of electrically conductive material, such as tungsten, platinum, and platinum alloys. The hot wire has a diameter of 5 μm and a length of 1 mm, and it is welded to the single and cross probe prongs, as shown in figures 3.2 and 3.3, respectively.

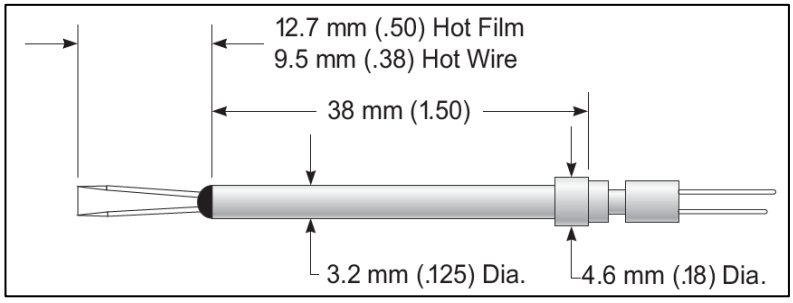

Figure 3.2: Single Hotwire probe Model 1210

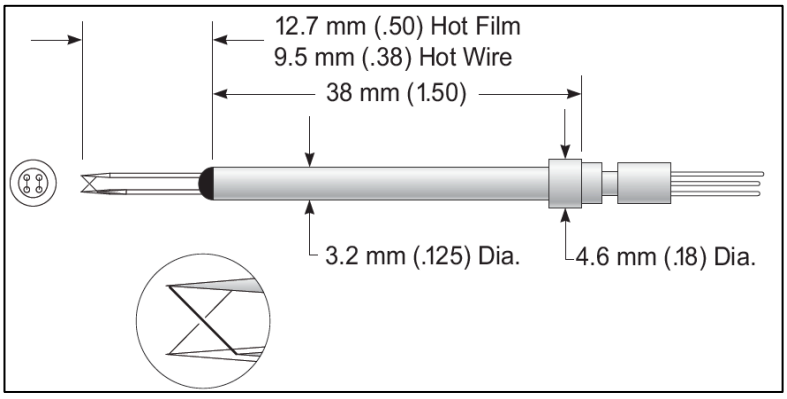

Figure 3.3: Cross Hotwire probe Model 1240

Spot welding or soldering methods would be used to mount these delicate and extremely sensitive wires on the probe prongs. The length of these prongs is important

and can have an impact on the hot wire system. Long prongs in periodic flows such as vortex shedding, for example, can vibrate and integrate deviation into HWA measurements. Hot-wire probes make it easier to test flow fields in gas and liquids.

3.2.2 HWA Principle

As previously stated, electrical current passes through the wire to keep the wire temperature constant. As a consequence, equation 3.1 gives the dissipated electrical energy from the sensor in the form of heat.

$$W_{elec} = I^2 R_w \tag{3.1}$$

Where I denote the electrical current flowing through the wire and R_w denotes the electrical resistance of the sensor.

To maintain the wire temperature constant, an equilibrium between the induced thermal energy and heat losses to the environment is needed. However, as the flow rate increases, the convective heat transfer varies, resulting in a new equilibrium. The HWA output is proportional to the flow velocity, and King's Law is an empirical law that describes the non-linear correlation between them and the flow velocity:

$$E^2 = A + BV^n \tag{3.2}$$

The coefficients obtained from the calibration method are A, B, and n. As a consequence, a 4^{th} order polynomial curve fit should be used, as it correctly estimates the inverse of King's law, and the output is proportional to the effective velocity.

$$V_{eff} = K + A*N + B*N^2 + C*N^3 + D*N^4 \tag{3.3}$$

Where V_{eff} denotes effective velocity, N denotes normalized bridge voltage, and A, B, C, D, and K denote constants to be established via the calibration method. The normalized voltage N is computed using the formula:

$$N = \frac{E - E_{\min}}{E_{\max} - E_{\min}} \tag{3.4}$$

Where, E is the Bridge voltage.

The fourth order polynomial curve fit has been applied to the normalized voltage to calculate velocities in order to produce a look up table that can be used for flow measurements. Figure 3.4 displays the calibration curve for a single probe, SN 961171. The calibration curve is non-linear, as can be shown, and the calibration was done for a velocity range of 0 to 20 m/s for 20 seconds sample data points which 17 m/s and 10m/s have been used for the velocity in the experiments. In comparison to high velocities, calibration at low velocities, which requires full sensitivity care, is done with a higher sampling density.

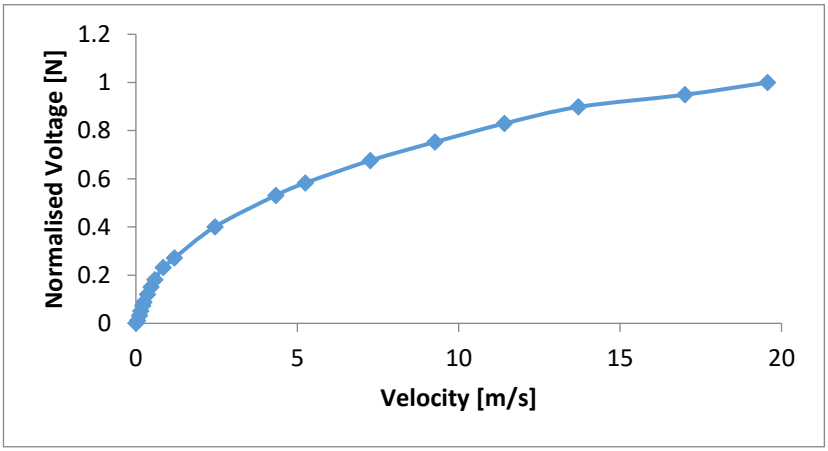

Figure 3.4: Calibration curve plot for single probe SN 961171

To every probe sensor, a look-up table is developed for the flow velocity range that will be used for calibration. The curve fit and mean square error (MSE) can be used to measure the calibration's accuracy. If the MSE is greater than 0.01-0.02 percent, repeat the calibration process to achieve an accurate calibration with correct curve fit and MSE.

3.2.3 Hot Wire Instrumentation

As shown in figure 3.5, the HWA used in this analysis is a constant temperature anemometer, which consists of a hot-wire probe mounted to a Wheatstone bridge (TSI Flow Point 1500 velocity transducer, CTA bridge). The output of the velocity transducers is transferred to the Flow Point velocity measuring device program through a DAS-1402 data acquisition card.

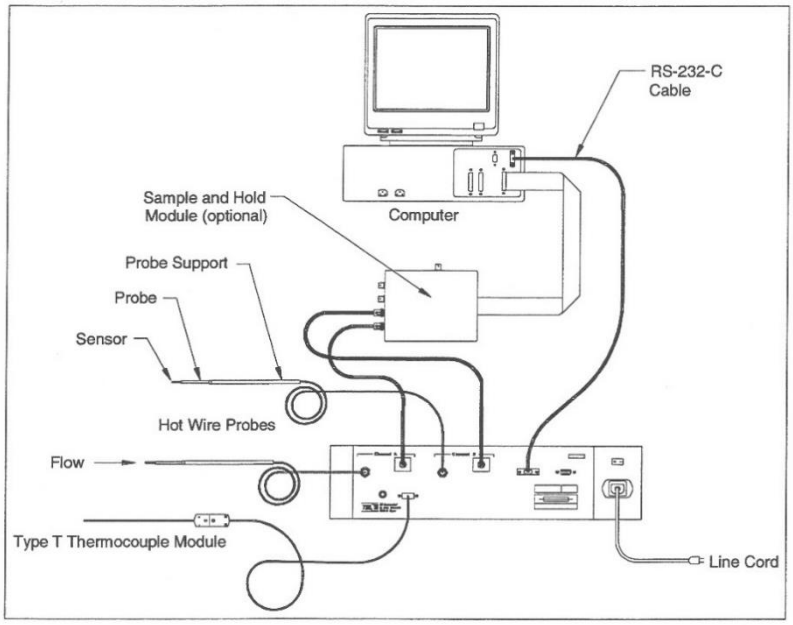

Figure 3.5: Hot wire anemometry system configuration (Figure taken from TSI Flow Point 1500 Instruction Manual)

The CTA hot-wire anemometry is regulated by the TSI Flow Point 1500 velocity transducer. The transducers' filter circuits and special bridges and amplifiers (figure 3.6) prevent excessive noise throughout data processing.

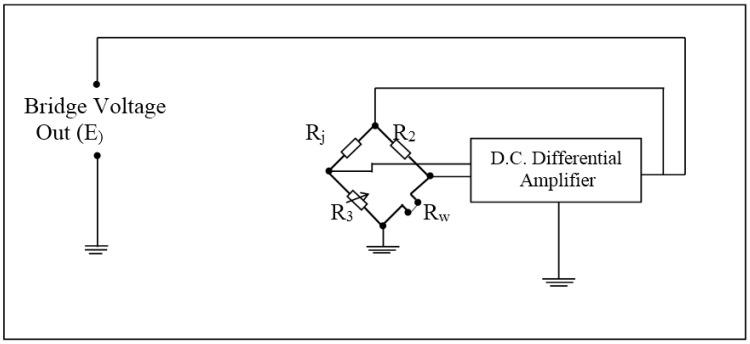

Figure 3.6: Schematic diagram of a thermal anemometer system (Wheatstone bridge)

TSI model 1210-T1.5 single normal (SN) probes and TSI 1243-T1.5 type x-wire probes were used in this study. The tungsten sensors were 3.8 μm in diameter and produced from tungsten.

3.2.4 Hot Wire Calibration

Before conducting each experiment, the HWA system must be calibrated. As a result, the calibration method previously mentioned will be used to evaluate the voltage-velocity guiding relationship.

The hot wire probes were calibrated with a TSI Model 1125 calibrator, which has a turbulence strength of less than 0.5 percent and thus removes potential error in the calibration constants. With this model, the calibrator has a velocity range of 0.01 to 300 m/s. The calibrator has three compartments accommodating low velocities (0.001 - 1 m/s), mid-range velocities (0.63 - 15 m/s), and high velocities (0.001 - 15 m/s) identified as D3, D2 and D1, consecutively.

A calibration against identified flow velocities is needed in order to use the CTA Hotwire system for data acquisition in the experiment. As a consequence, the output voltage would be a variable of the flow velocity.

Because of the impact of atmospheric pressure and temperature fluctuations on the results, the ambient pressure and temperature have been regarded for velocity calculations throughout all calibration process and data acquisitions.

The temperature (Bearman, 1971) and pressure impact on the TSI hot wire probes necessitate an ambient condition correction during the calibration process. As a result, a correction factor KVCF (TSI Manual) is applied to nominal velocities:

$$K_{VCF} = \sqrt{\left(\frac{293}{273+T}\right)\left(\frac{P}{760}\right)} \tag{3.5}$$

Whereby T = Atmospheric temperature (C)

P = atmospheric pressure (mm Hg).

In addition to adjusting for environmental conditions, a directional sensitivity right factor must be used for calibration, taking into account the flow path as studied by (Jorgensen, 1971). The direction of flow as well as the sensor axis must be in the same direction in an endpoint flow condition, while the sensor axis must be natural to the flow direction in a cross-flow condition. The response of a hot wire probe to end flow and cross flow conditions differs. Because of this directional sensitivity, a cross flow calibrated probe subjected to end flow conditions will yield false positives. As a result, the pitch response of the TSI probe was adjusted using the manufacturer's correction factor KSF.

The calibration curves for both single and cross probe have been present in Figures 3.7 and 3.8 respectively. The MSE of the both calibrations have been calculated and observed as 0.01 for the single probe and 0.005 for the cross probe. Since both of the values are in the interval that have been discussed in the previous section the calibration is validate.

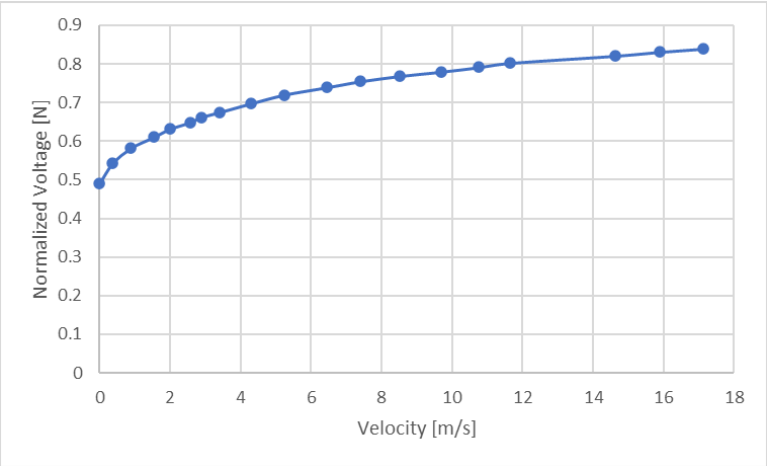

Figure 3.7: Calibration curve plot for Single probe

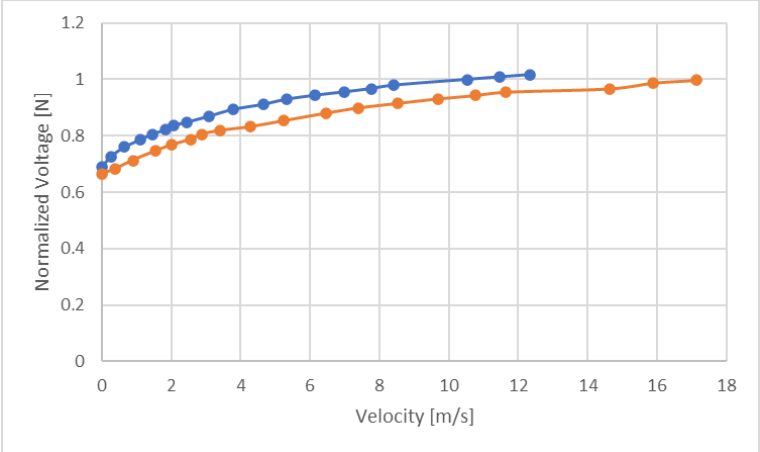

Figure 3.8: Calibration curve plot for Cross probe

3.2.5 Hot Wire System Settings

The HWA must be calibrated in order to calculate a relationship involving velocity and voltage, as described earlier. Inside the Flow Point app, you can adjust HWA configurations including probe type, probe-cable resistance, sensor resistance, gain, and offset. The probe-cable resistance was calculated using a simple unit, as well as the manufacturer gives sufficient system settings, as shown in table 3.1.

Table 3.1: Hot wire sensors settings

	Probe resistance	Wire resistance	Operating resistance	Operational temperature
1210-T.15	5.96 Ω	0.28 Ω	11.66 Ω	250 °C
1210-T.15	5.70 Ω	0.24 Ω	11.33 Ω	250 °C
1241-T.15	5.57 Ω	0.19 Ω	1082 Ω	250 °C

3.3 Hot Wire Probe Traverse Mechanism

As shown in figure 3.7, the X probe is installed on a three-axis traverse system that allows it to move throughout the target domain throughout data capture. For navigating across all directions, this mechanism's accuracy is 0.25 mm. All measurements were made in the z-direction at the midway point of the test segment, and the probe was traversed in x-y for a region of 0.5L to 4.0L in the downstream wake region. Traverse Mechanism Specification:

- 250 x 250 [mm] operation domain in XY plane
- 250 [mm] operation in Z axis
- Accuracy Max. 1600 steps per revolution.

The cross-Hotwire sensor was installed on a design 1155 probe help 457 mm upstream of the traverse system, with a 6 percent blockage ratio measured. It is agreed that the impact of the system on the data measuring equipment is insignificant in such conditions.

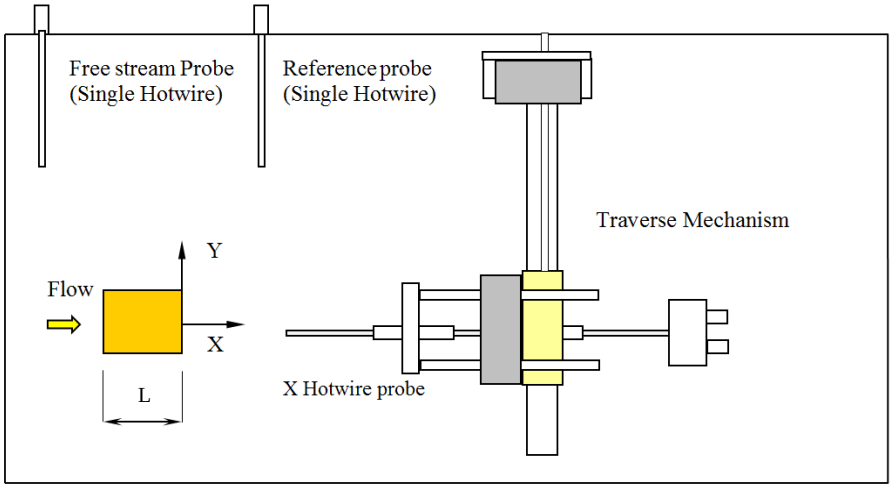

Figure 3.9: Schematic of hotwire probe traverse mechanism

3.4 Data Analysis Program Code

The obtained velocity data was evaluated in this section using in-house FORTRAN codes in conjunction with MATLAB/SIMULNIK software. Three velocity transducers were used to collect data on velocity. Two independent transducers were used to acquire the free flow velocity and reference velocity signals. The u and v velocity components from the x hotwire probe were acquired using the last velocity transducer. Because of the noise and interference in the obtained velocity signal, it is important to clean up/filter it.

As a result, the acquired velocity data were first converted to a matrix format in order to perform filtering operations on the data in MATLAB/Simulink. Convertor1.for, a FORTRAN application, was used to perform the reorganization. The velocity signal

data was then cleaned up in MATLAB/SIMULINK (figure 3.8) for high and low frequency noises with cut-off values greater than 0.25 and less than 0.25 and below 0.40, respectively. A delay in reference to the main signal was identified after each filtering activity. As a result, the latency value has been replaced into the circuit after each sorting process to rectify the schedule change. A standard filtered and unfiltered velocity signal is shown in Figure 3.9.

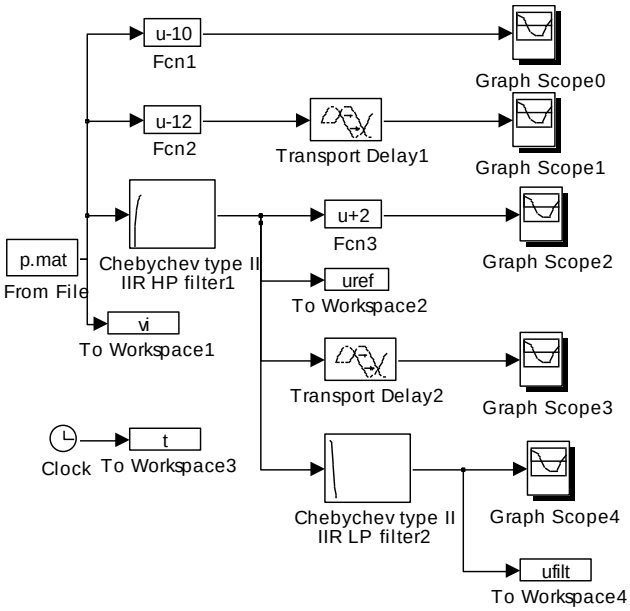

Figure 3.10: Simulink diagram of filtering program

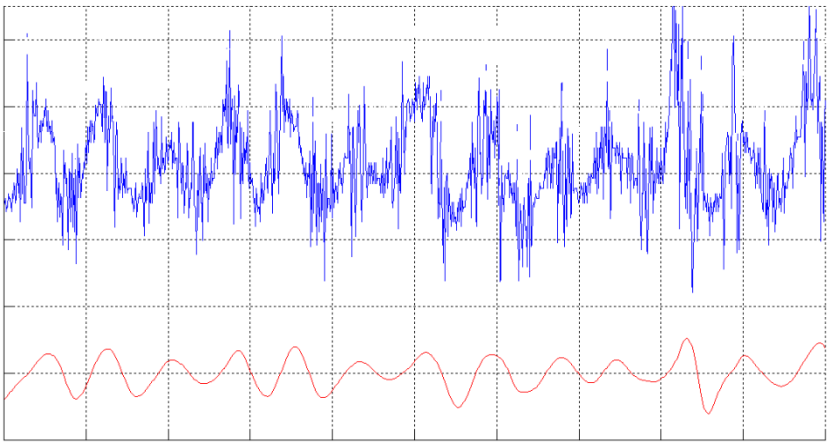

Figure 3.11: Acquired unfiltered (Top) and filtered (Bottom) velocity signal

Thus, utilizing this same FORTRAN software Convertor2.FOR, the initial velocity signal as well as the filtered velocity results were combined to achieve the null crossing point through reference signal evaluation. Eventually, using the ensemble for software, the velocity results was evaluated and velocity characteristics were calculated. Also, on Navier-Stock equation, phase aggregation, aggregate averaging, and triple degradation techniques have been used, and ensemble. For program code was established depending on the revised Navier-Stokes equations.

The velocity data have been acquired at sampling rate of 5 kHz (Due to the expected shedding frequency and measured frequency this value is sufficient) for sampling time of 2.048 second with a sampling size of 10 kpts/ch (kilopoints/channel). As described in the, preceding section the flow structures were investigated using triple decomposition and ensemble aggregation methodologies. The revised Navier-Stokes equation is obtained as follows upon disintegrating the instantaneous velocity into three components and implementing the above strategies toward the Navier-Stokes equation:

$$\frac{D\overline{u}_i}{Dt} = -\frac{1}{\rho}\frac{\partial \overline{p}}{\partial x_j} + \nu\frac{\partial^2 \overline{u}_i}{\partial x_i \partial x_j} + \frac{\partial}{\partial x_j}\left(-\langle\overline{\widetilde{u}_i \widetilde{u}_j}\rangle - \langle\overline{u_i' u_j'}\rangle\right) \tag{3.12}$$

Consequently $\langle\overline{\widetilde{u}_i \widetilde{u}_j}\rangle$ Owing to the step weighted result of clear, an additional term leads to Reynold's stress. This coherent Reynolds stress term, like the incoherent Reynolds stress term, is a flow-based domain that necessitated additional effort for periodic flow such as vortex shedding.

Obtaining the heavy reliance of the triple constituents of velocity on time (normalized with respect to total duration T) during each full period of occurrences is necessary for this analysis. As a reference signal, the periodic vortex shedding velocity variability

was chosen. As a result, the obtained free - stream and lateral velocity elements around the specific moment are averaged and combined for the identical t/T of sequential reference periods. Through one step, this aggregation procedures are replicated for various standardized periods in order to create the differentiation of various structures and or, and so on.

In addition, as previously stated, the reference signal is needed to determine the phases of each velocity variable. As a result, it is critical to place the reference probe in the correct position, as incorrect placement would have an impact on the data evaluation.

The critical step is to figure out how many cycles are needed to achieve phase averaging so that the structures are cycle self-sufficient. For this reason, a preliminary experiment was carried out with a series of phases ranging from 100 to 400 cycles. It was discovered that constant functions of properties like normal and shear stress needed at least 150 cycles for consolidation. As a result, the number of phases needed to implement step aggregation in this analysis were established at 300-400 cycles.

Chapter 4

APPLICATION OF TRIPLE DECOMPOSITION TECHNIQUE ON NEAR WAKE MEASUREMENTS OF SQUARE CYLINDER

4.1 Summary

In this chapter the vortex shedding near wake region downstream of a cylinder with square cross section has been studied by employing triple decomposition of the flow into mean, periodic and random velocity contributions. Coherent structures have been identified and incoherent fluctuation have been investigated. While for streamwise velocity a coherent structure peak of 20% of phase averaged magnitude have been observed, for transverse velocity, the coherent structure of the same order of phase averaged has been reported. It was demonstrated that while a vortex is developing from one edge with maximum incoherent streamwise stress, the initiated shear layers from the other edge exhibit a maximum in incoherent transverse stress. Investigations were conducted at a maximum speed of U_∞ = 16.6 ± 2% m/s, Re=3.3×10^4 and turbulence intensity of 0.8%.

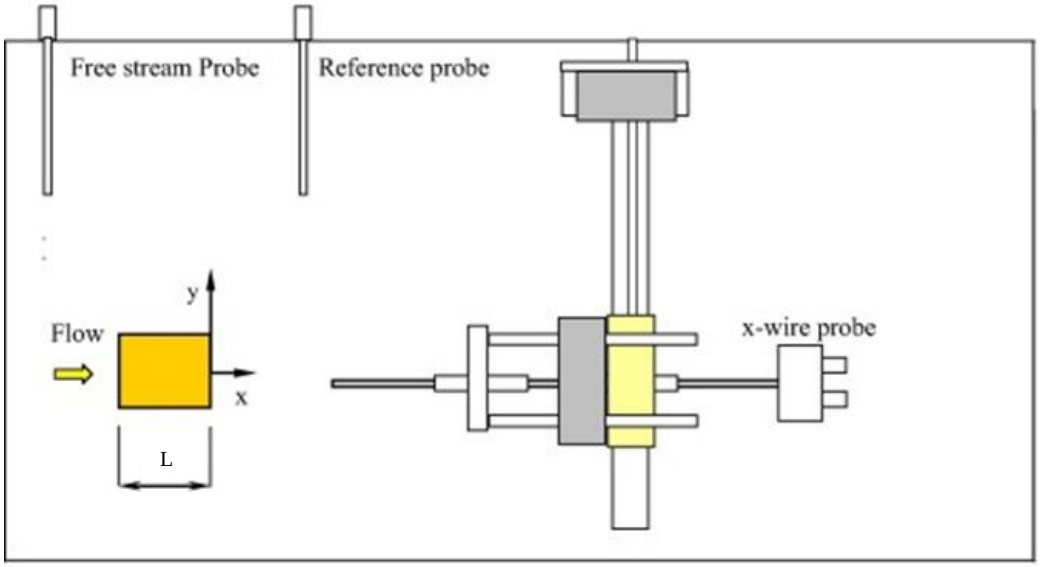

Figure 4.1: Experimental setup

A plexiglass hollow cylinder with a square cross section of 30 mm × 30 mm was selected for the experiment. Consequently, with employing end plates, the aspect ratio of the investigated square cylinder was 14. The Reynolds number of the experiment was Re = 33,000 (based on the cylinder width) resulting in turbulent vortex shedding behind the square cylinder in the domain of interest ($0.5 < x/D < 4.0$).

4.2 Experimental Results

4.2.1 Shedding Frequency and Strouhal Number

Fast Fourier Transformation (FFT) method has been applied to the collected velocity unit in the domain of interest to calculate the dominant vortex shedding frequency. Therefore, the peak of the highest spectral corresponded to the dominant vortex shedding frequency. Spectral analysis of transverse velocity component for different x/D's, downstream of the square cylinder is illustrated in Figure 4.2.

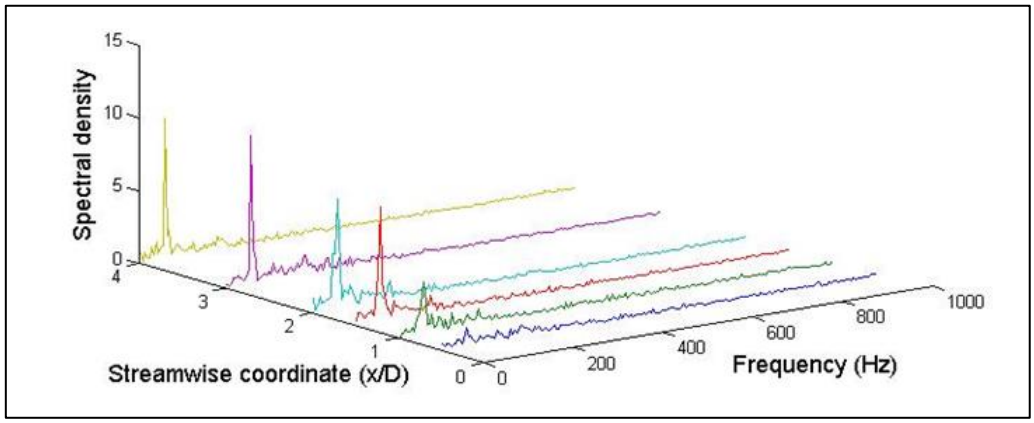

Figure 4.2: Spectral analysis for various x/D behind cylinder

The dominant shedding frequency can be observed as a single peak which correspond to an identical Strouhal number for all x/D's in the near wake behind the cylinder. In addition, magnitude of the peaks from the power spectral density graph is increasing as x/D increases from x/D=0.5 to 4.0. The result of the FFT evaluation on transverse velocity and streamwise velocity shown that the dominant shedding frequency is equal and for sake of brevity only transverse results were presented. From the Table 4.1 it has observed that the computed Strouhal number is in a good agreement with other literature. The reason of the slight difference between the current study and literature is due to various blockage ratio and turbulent intensity.

Table 4.1: Verifing the strouhal number with published studies

Literature	Geometry	Re	St
Current study	Square cylinder	3.3×10^4	0.107
(Lyn, Einav, Rodi, & Park, 1995)	Square cylinder	2.1×10^4	0.13
(Okajima, 1982)	Square cylinder	10^4 - 2×10^4	0.13
(Bearman & Obasaju, 1982)	Square cylinder	5.8×10^3-3.2×10^4	0.13
(Lyn & Rodi, 1994)	Square cylinder	2.1×10^4	0.134
(Kurtulus, Scarano, & David, 2007)	Square cylinder	4.9×10^3	0.128

4.2.2 Time Averaged Results

Figures 4.3 and 4.4 show the process aggregated time-mean of the velocity profile in the streamwise and transverse axes, correspondingly. In the aftermath of the square cylinder, these graphs show the data for various x/Ds. So rather than time averaging, the attribute of time average was evaluated as phase averaged time-mean values in this study. As a set of unconditioned samples, the latter performs a temporal averaging operation over all of the cycles. The averaging method for phase averaged time-mean properties, on the other hand, is performed over one cycle with values gathered from all cycles. Because both procedures suggest the same average, the test findings are identical. Quantitative comparison of these results with other studies on flow over square cylinder (Saha et al., 2000) shows good agreement. As can be seen from the figures, both streamwise and transverse velocities demonstrate symmetric patterns for different x/D ratios. Moreover, the highest value of negative and positive peak on the edges have demonstrated by time averaged transverse velocity. The discussed peaks could be an implication of vortices by the edges of the cylinder. The transverse velocity profile decays significantly while the probe moves toward downstream in the wake region. The wake expands as the flow progresses downstream, as fluid is repeatedly enter to the wake from the cylinder's edges. The time averaged transverse velocity profile is another indicator of an entrainment process. High fluid entrainment towards the centerline can be seen very close to the wake region. However, in the downstream wake, such a process faded dramatically beyond 4D.

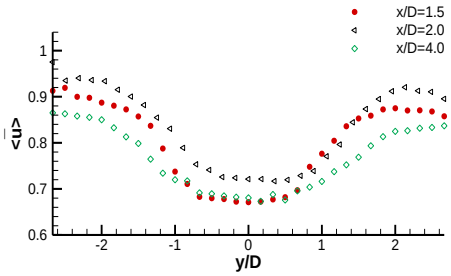

Figure 4.3: Streamwise time averaged velocities

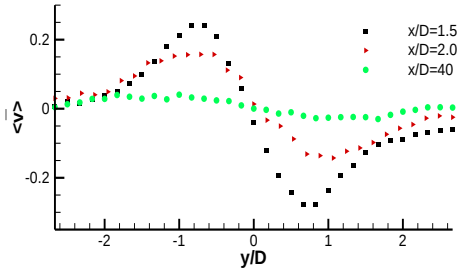

Figure 4.4: transverse time averaged velocities

The classical Reynolds decomposition defines the instantaneous velocity as $u = \bar{u} + u'$ where $u' = \tilde{u} + u'_{incoherent}$. Thus, classical Reynold's decomposition expresses both periodic fluctuation and random fluctuation as a single term. Triple decomposition, on the other hand, differentiates between coherent structure or vortex shedding and incoherent or random turbulent fluctuations. As a result, the periodical shedding phenomenon can be ignored in favour of a thorough analysis of the incoherent fluctuations. Time averaged incoherent streamwise and transverse normal Reynolds stresses acquired at various x/D's behind the cylinder with square cross section are depicted in Figure 4.5 (a) and (b), respectively.

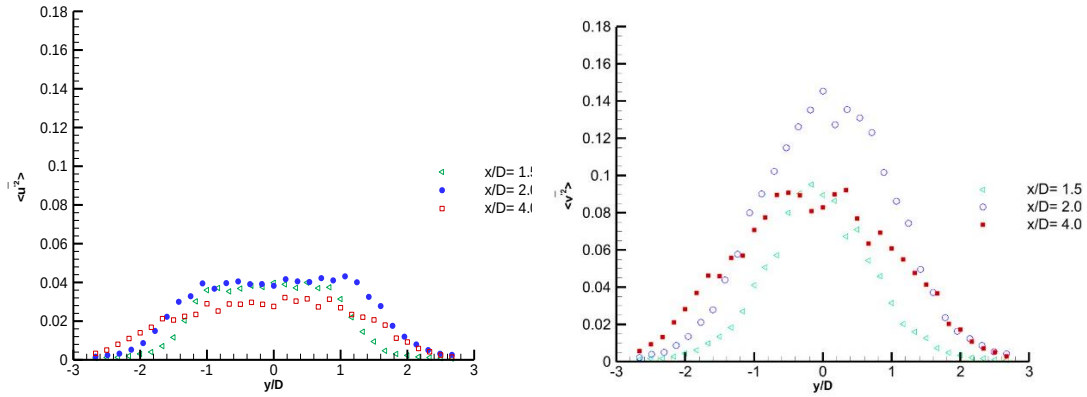

(a) (b)

Figure 4.5: Time averaged incoherent normal Reynolds stress

From Figure 4.5 it can be observed that while streamwise normal stress demonstrates double peak profile, transverse normal stress reaches a peak at the centerline. This phenomenon is in accordance with the phase averaged incoherent turbulent kinetic energy contours as illustrated in Figure 4.8. In the presence of coherent structures, treating coherent structure and random fluctuation as one can lead to a significant overestimation of the stochastic part of the flow (Baj, Bruce, & Buxton, 2015). In addition (Saha et al., 2000) reported $(\overline{u'})^{\frac{1}{2}}$ and $(\overline{v'})^{\frac{1}{2}}$ are the same order as these terms in classical Reynolds decomposition containing both periodic and random fluctuation. However, by extracting coherent structure from incoherent random turbulent fluctuations, incoherent transverse stress is observed to be in order of 3 times of incoherent streamwise stress.

4.2.3 Coherent Structure

Figures 4.6 and 4.7 present temporal and spatial development of coherent structure of the velocity components for both streamwise and transvers axis of different x/D's in the downstream of the cylinder. The coherent structure is concentrated along the edges of the square cylinder at wake zone close to the square base (i.e. x/D=0.5). The

creation of coherent structures, on the other hand, can be seen as vortices convected downstream in the wake zone. The coherent structure peak is roughly 20% of its phase averaged values, according to a contrast involving the $\langle u \rangle$ peak and the $\langle \tilde{u} \rangle$ peak.

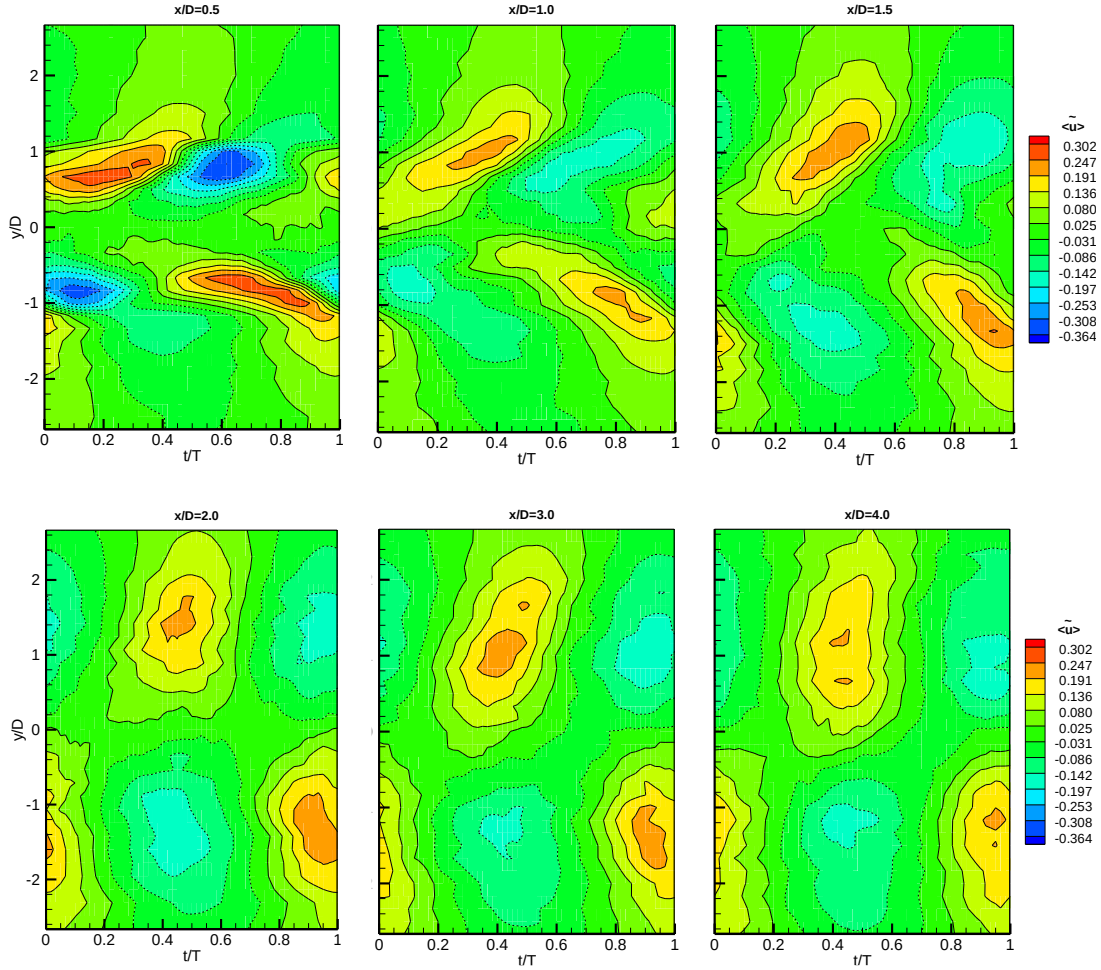

Figure 4.6: Coherent streamwise velocity component for different x/D's

Despite that, for transverse velocity, the coherent structure of the same order as the phase averaged has been observed, due to a considerable lateral momentum within the shedding process.

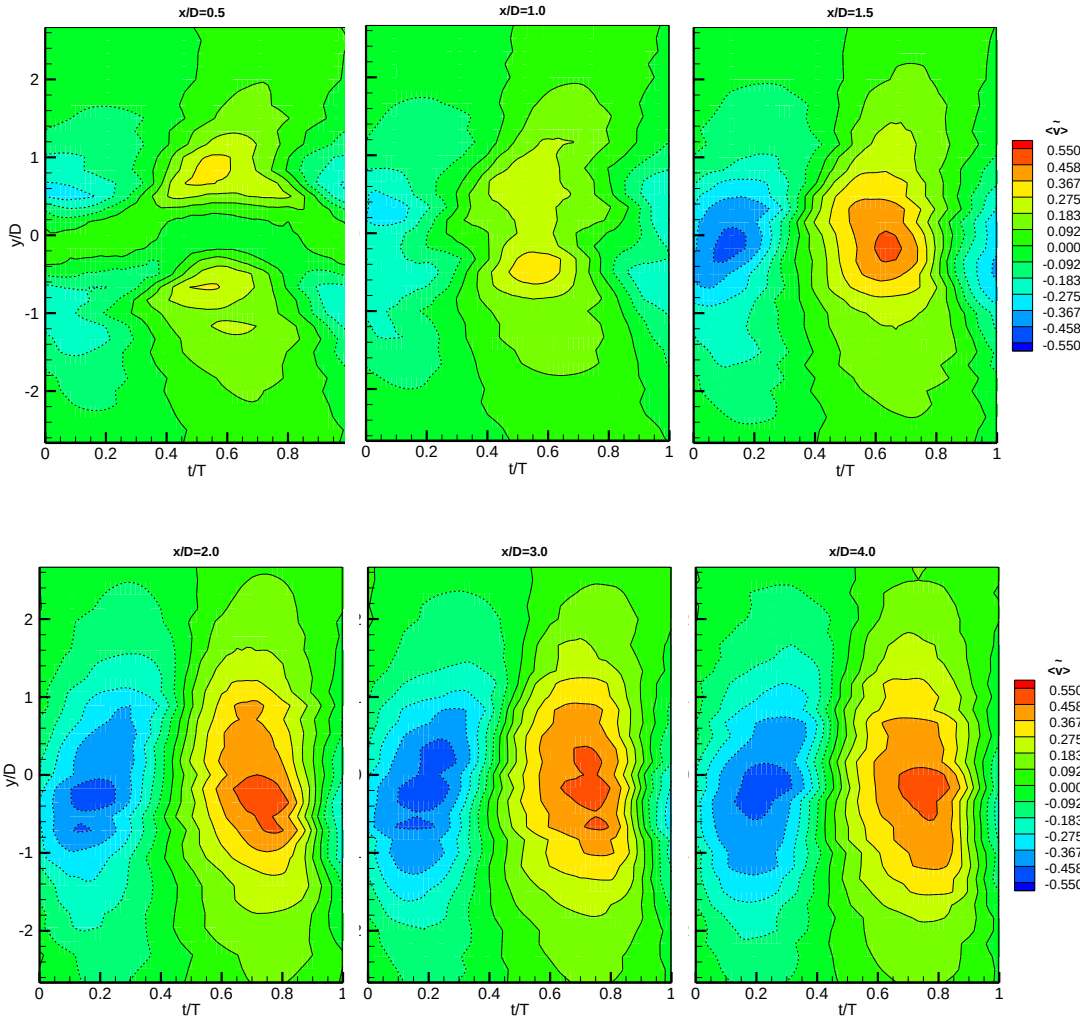

Figure 4.7: Coherent transverse velocity component for different x/D's

4.2.4 Incoherent Structure

Triple decomposition differentiates across coherent structure or vortex shedding occurrence and incoherent pattern of turbulent oscillations as previously mentioned. As a result, the periodic shedding process can be ignored in favour of a thorough analysis of the incoherent fluctuations. Figure 4.8 depicts incoherent turbulent kinetic energy in the wake zone at three distinct normalized streamwise coordinates. Development of the incoherent turbulent kinetic energy is clearly recognizable from the figure. When the probe travel further downstream of the wake from x/D= 0.5 to 2.0, the incoherent TKE peak increases by approximately 86%. In contrary, for x/D

beyond x/D=2.0 the incoherent TKE peak decreases approximately 29% in region 4D downstream in wake.

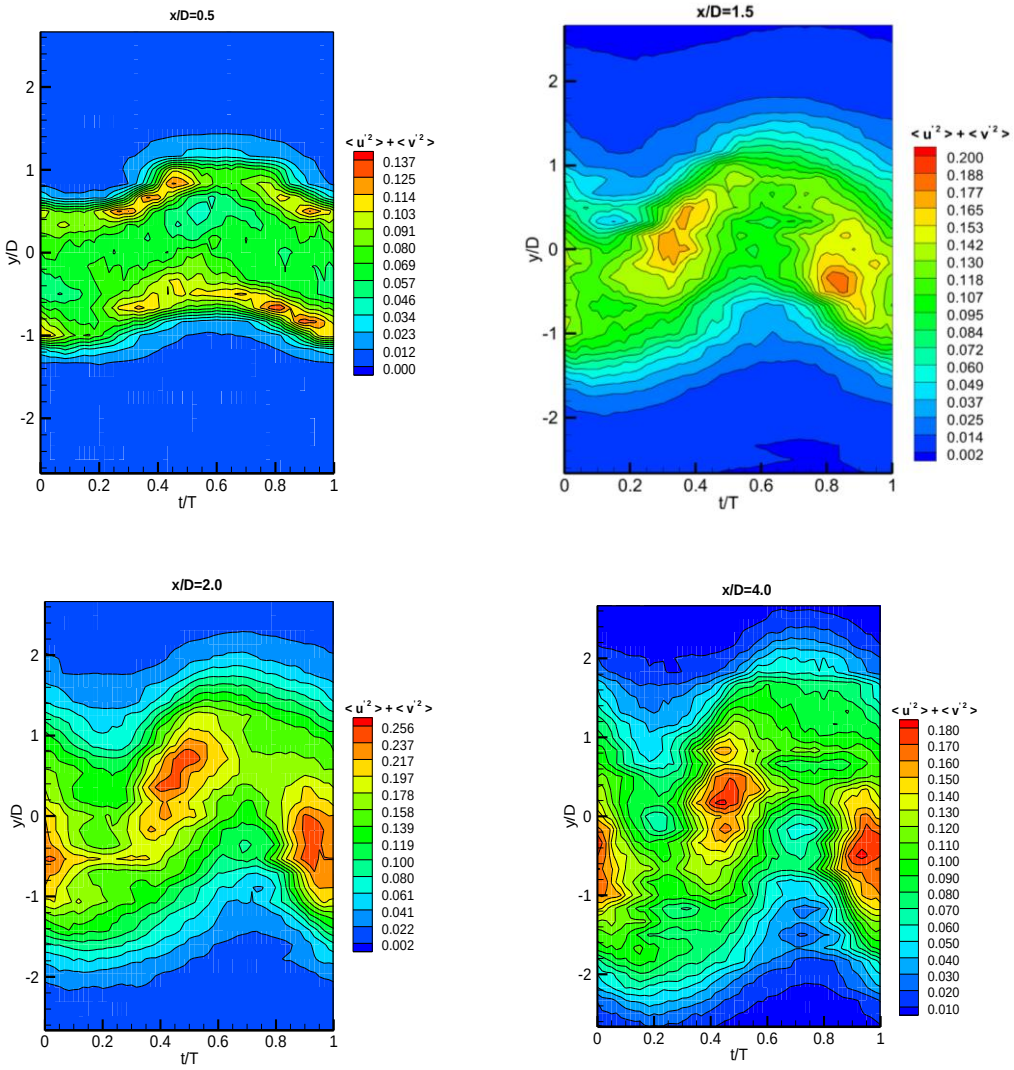

Figure 4.8: Incoherent turbulent kinetic energy for different x/D's behind square cylinder

In addition, the plotted contours of TKE also demonstrate that the main incoherent turbulent kinetic energy concentrated in the region with the same width of square cylinder. However, at near wake region i.e. x/D=0.5, the maximum value of the TKE concentrated through the boundaries of the separated shear layer which corresponds to vortex shedding from both sides of the square cylinder. As the probe moves

downstream in the wake region, the wake is widened and these peak regions are developing toward the centerline. As a result of such development, the TKE concentrated in the wake as wide as the initiated shear layers with peak approximately along the centerline.

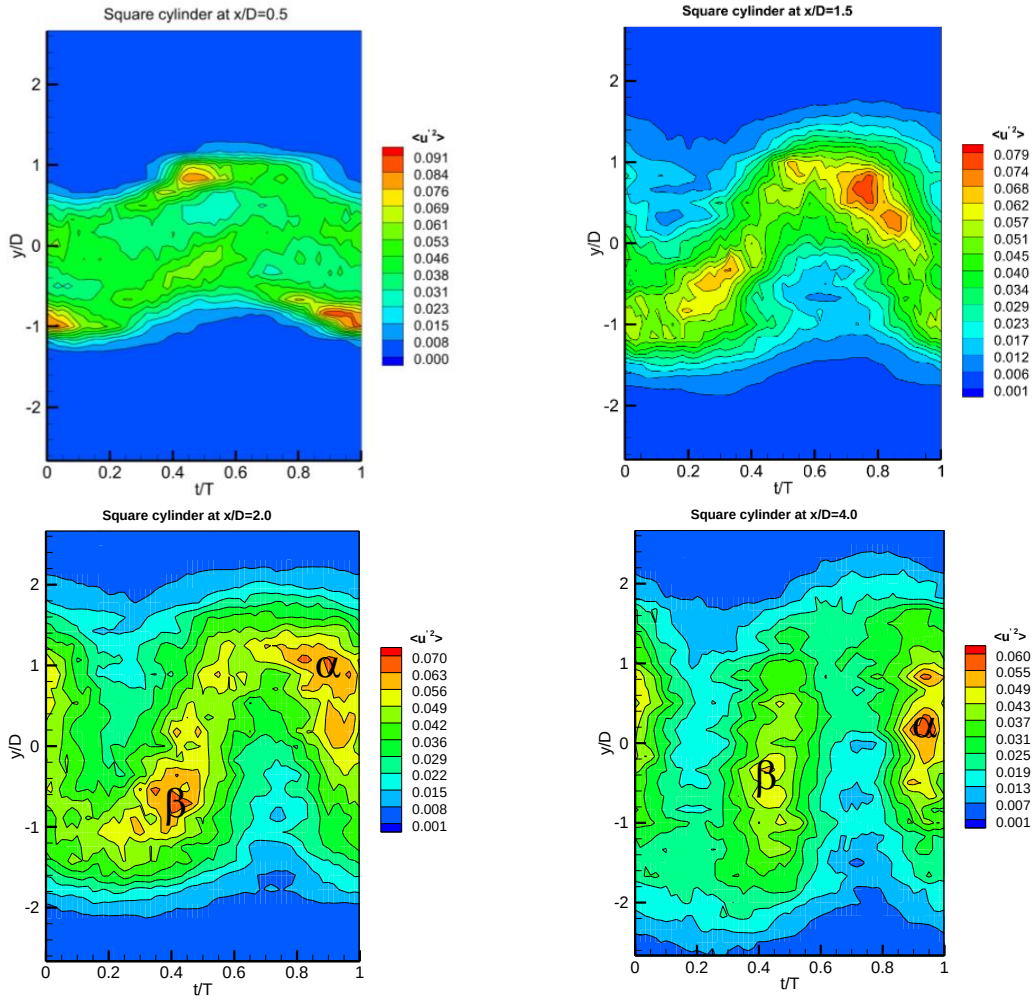

Figure 4.9: Incoherent streamwise Reynolds stress at various x/D

Figures 4.9 and 4.10 illustrate the incoherent streamwise and transverse Reynolds normal stress contours, respectively. A comparison between the contours demonstrates that the peak of both stresses (marked as α and β in the figures) coincide at the same normalized time. However, while streamwise stress is at peak at one edge of the square cylinder, the opposite edge of the square cylinder exhibits a maximum

in transverse stress production. Such observation demonstrates that while a vortex is developing from one edge with maximum streamwise stress, the initiated shear layers from the other edge exhibit a maximum in transverse stress production.

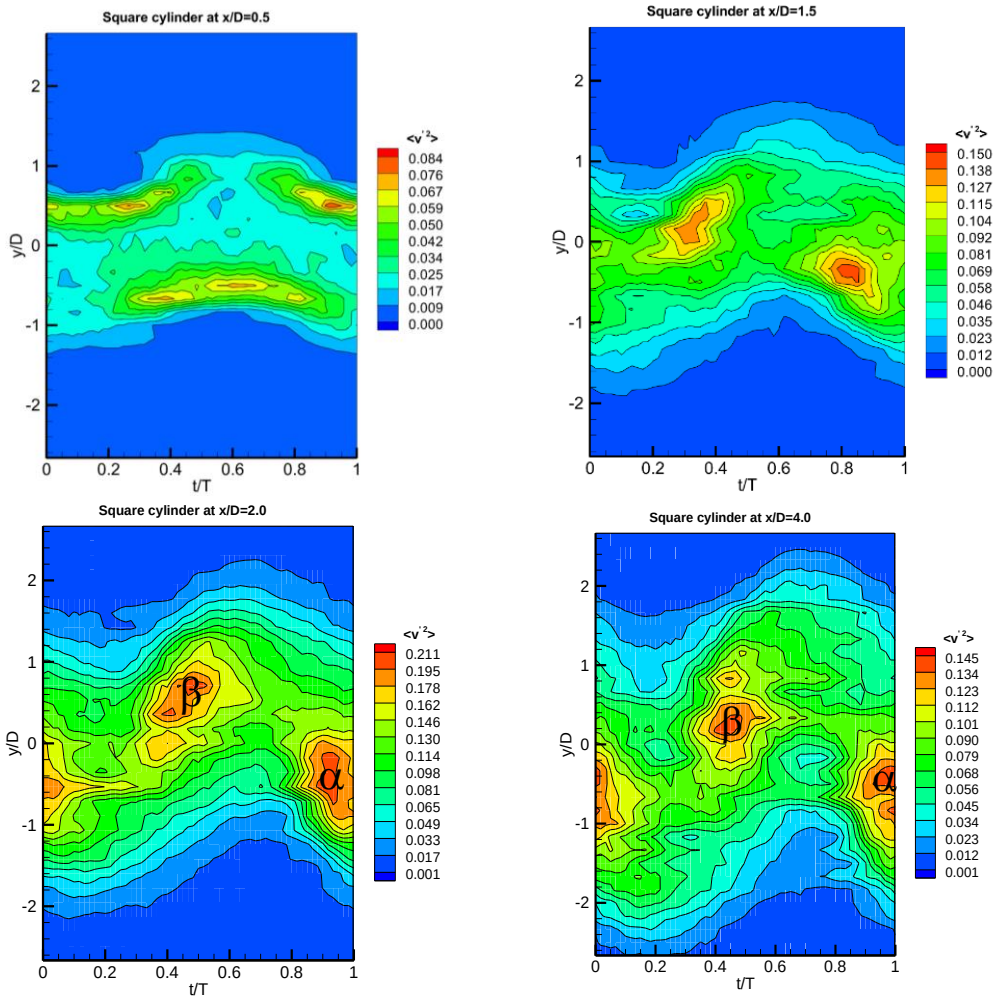

Figure 4.10: Incoherent transverse Reynolds stress at various x/D behind square cylinder

A detailed investigation on phase averaged velocities and incoherent normal Reynolds stresses has revealed an additional remarkable finding. Figures 4.11 and 4.12 illustrate streamwise and transverse velocity components acquired at x/D=0.5 and 2.0 in the downstream wake region.

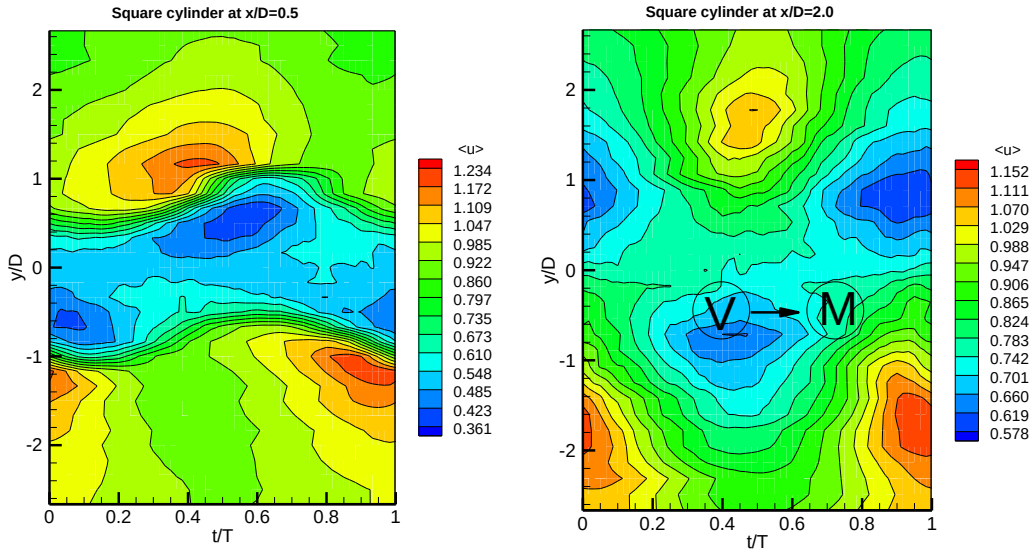

Figure 4.11: Stream wise phase averaged velocity at x/D =0.5 and x/D =2.0

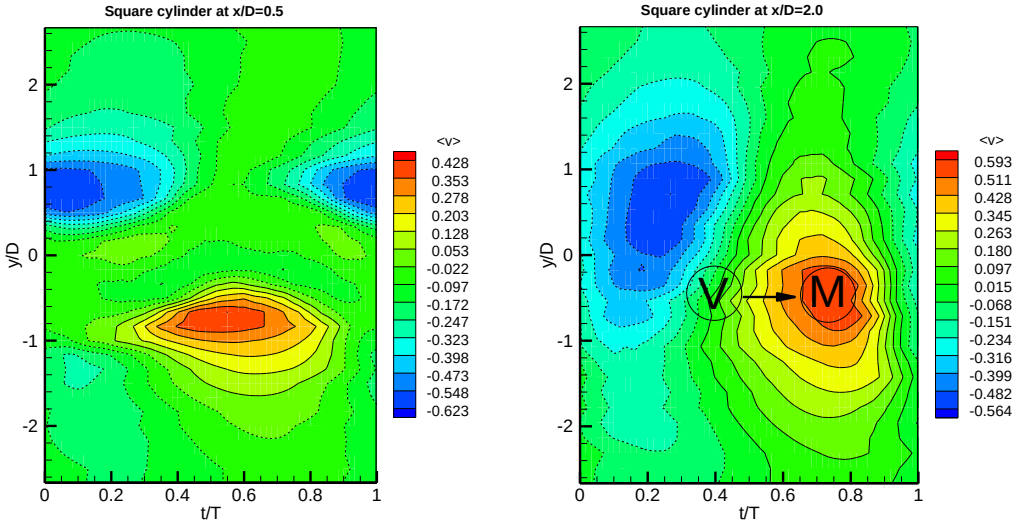

Figure 4.12: Transverse phase averaged velocity at x/D =0.5 and x/D =2.0

It can be observed that the incoherent stresses exhibit similar phase with streamwise velocity. However, the stresses exhibit a phase lead of t/T=0.2 with respect to transverse velocity maxima. Therefore 1/5 of period after a vortex is shed (marked as V in the figures), a substantial momentum transfer in the direction of the opposite shear layer is perceptible (point M). Moreover, the streamwise normal stress peak corresponds to the edge with minimum streamwise velocity. In contrary, transverse normal stress peak occurs simultaneously at the other edge exhibiting a peak in

streamwise velocity. Comparison between the turbulent energy contours and normal Reynolds stresses reveals that the TKE contour trends follow transverse normal Reynold's stress development. This phenomenon has also been confirmed by time averaged incoherent normal Reynolds stresses plot (Fig. 4.5). Therefore, the more energetic transverse normal Reynold's stress is the major contributor to incoherent turbulent kinetic energy.

Chapter 5

TURBULENT KINETIC ENERGY IN THE WAKE REGION OF MODIFIED CIRCULAR CYLINDERS

5.1 Summary

For several decades, one of the most intriguing issues among researchers has been flow qualities and wake formations behind bluff bodies. The use of bluff bodies in different fields such as engineering and industry has sparked a great deal of curiosity in this phenomenon. The structure of the fluid flow in the wake of a Circular Cylinder, Semi-circular Cylinder, and C shape have been compared in this chapter. To see if there are any commonalities among these shapes, the wake flows were examined in terms of shedding frequency, Reynold's stress, and Turbulent Kinetic Energy (TKE). On either side of the isolated shear layer, the largest value of turbulent kinetic energy was discovered. Furthermore, it was discovered that when the TKE developed downstream, the peaks migrated towards the centerline. Formation of Vortex Street in the wake region of bluff bodies is a matter of great importance in the field of engineering. Such periodic phenomenon, could be the cause of devastating load on the structural body and may lead to catastrophic incidents. Therefore, to prevent such destruction, it requires a better understanding of this phenomenon.

5.2 Experimental Setup

The experiments have been made in an open-return subsonic wind tunnel at Mechanical Engineering Department, Eastern Mediterranean University. The free

stream velocity of the experiment was U=10.44±2% m/s. The Reynolds number of the experiment was Re= 20660 (Re=UD/ν) based on cylinder diameter of 30mm. In this study flow structures around a semicircular cylinder (SC) and a circular cylinder (CC) with a diameter of 30 mm were investigated. In addition, a C shape (CS) with a diameter of 30 mm was also considered to identify flow structure similarities between these geometries. Stream wise and transverse velocity components have been acquired by employing TSI Flow point 1500 CTA Hot-Wire anemometer system for various x/D ratios behind the plates. The domain of investigation in the wake region was between 1.0 D to 6.0 D of the cylinder diameter ($1.0 \leq x/D \leq 6.0$) as illustrated in figure 5.1.

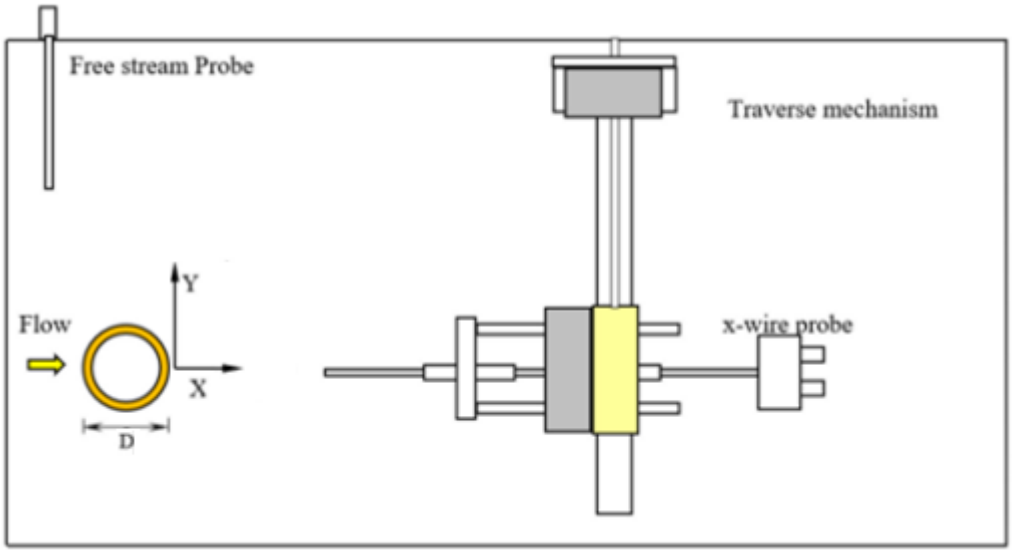

Figure 5.1: Experimental setup and coordinate system (top view)

Circular cylinder (CC) | C Shape Cylinder (CS) | Semicircular cylinder (SC)

Figure 5.2: Modified cylinder geometries (t=3mm)

The flow properties examined by two techniques namely triple decomposition and ensemble averaging. Therefore, any instantaneous properties of flow can be determined as superposition of time-mean averaged ($\bar{\phi}$), coherent ($\tilde{\phi}$) and incoherent component (ϕ') as follow:

$$\phi = \bar{\phi} + \tilde{\phi} + \phi'$$

For phase averaging technique, the operation will be performed on successive data with the same form respect to a specific wave. Therefore,

$$\langle \phi' \rangle = \frac{1}{n} \sum_{1}^{n} \phi_i'$$

Where n is the number of cycles and (ϕ') is the value of incoherent component at the same normalized time successive cycles. In order to obtain the modified Navier-Stokes formula, two technique namely triple decomposition and phase averaging techniques implemented on the Navier Stokes momentum equation.

5.3 Results and Discussion

The dominant vortex shedding frequency can be determined by implementing (FFT) method on the obtained velocity unit in the domain of investigation. Therefore, the spectral peak will indicate the dominant vortex shedding frequency.

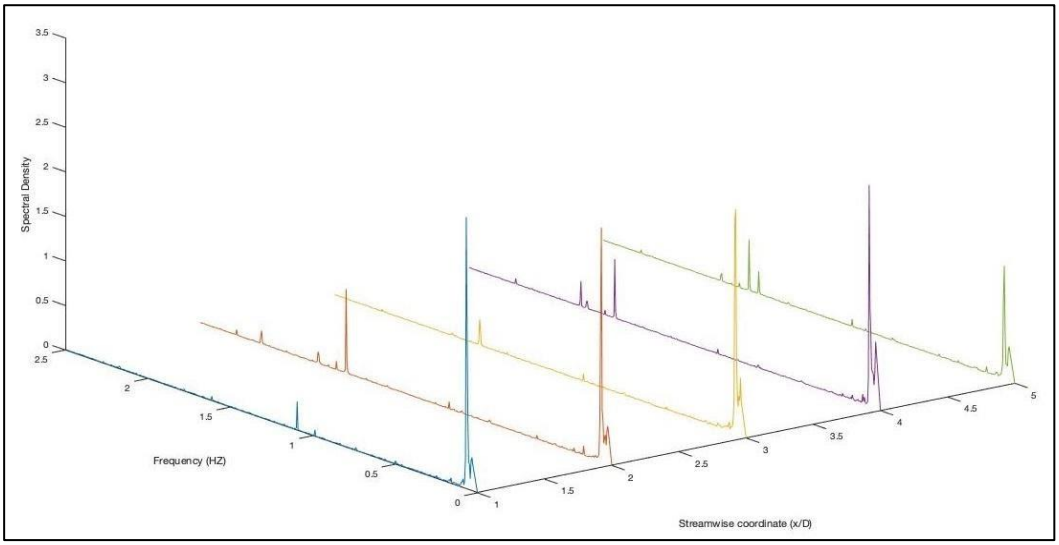

Figure 5.3: Spectral analysis for various x/D behind semi circular cylinder

From Figure 5.3 the dominant shedding frequency is apparent as a single peak. Which correspond to an identical Strouhal number (st=fD/U) in all x/D's near wake behind the cylinders and have shown in Table 1. The FFT analysis on both stream wise and transverse velocity components resulted in equal dominant shedding frequency and for sake of brevity only transverse results were presented.

Table 5.1: Frequency and strouhal number for different geometries

Geometry	Frequency (Hz)	S_t
Circular Cylinder (CC)	63.5	0.182
Semi Circular Cylinder (SC)	68.4	0.197
C shape Cylinder (CS)	68.4	0.197

In this study coherent and incoherent turbulent energy production behind modified circular cylinders have been investigated and some remarkable features of this periodic flow have been studied. Figure 5.4 illustrated the development of the coherent turbulent kinetic energy downstream wake of CC, SC and CS cylinders. According to

the observation from Figure 5.4 the evolution of the TKE is clearly evident for higher x/D downstream the wake. Similarly for all investigated geometries, near the base the TKE peak intense for both sides of the separated shear layer corresponding the shed vortices.

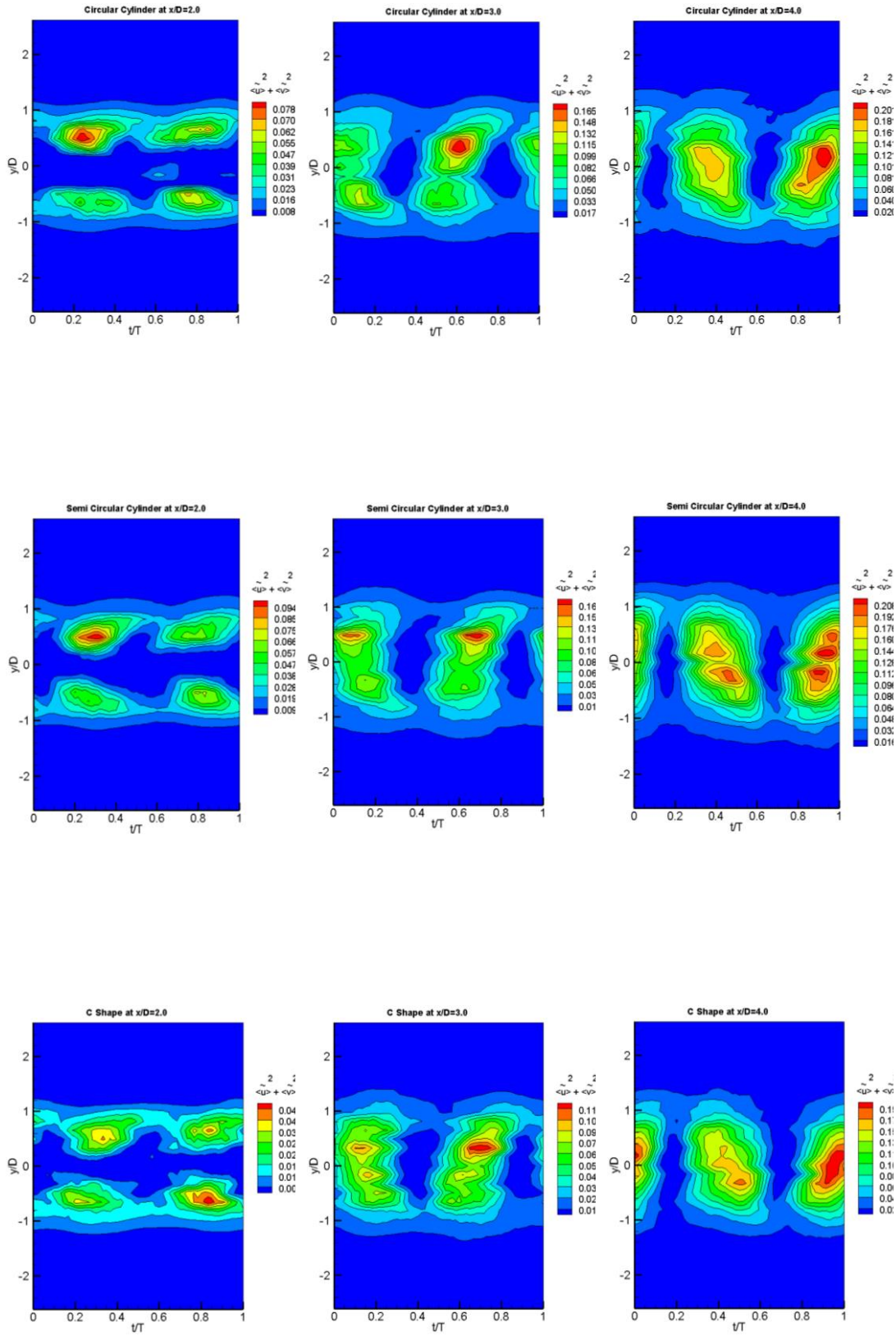

Figure 5.4: Coherent Turbulent Kinetic Energy

However, the TKE peaks shifted toward the center of the wake as the probe moves further downstream. In this regard, SC demonstrated a delay in transition of the peaks from sides of the wake towards the center. Therefore, in the zone near to the base i.e. x/D= 2 the turbulent kinetic energy reaches its peak once in each cycle at each side of the wake, while at higher x/D TKE peak occurs twice per cycle close the centerline of the wake. Figure 5.5 demonstrated the incoherent turbulent energy for different x/D in the wake region at the back of the modified circular cylinders. In a similar manner to coherent turbulent kinetic energy as discussed previously, incoherent TKE development in the downstream wake is also evident from Figure 5.5. Although, it has been demonstrated that, the incoherent TKE developed within the edges of the periodic flow as it passes towards downstream (Figure 5.5). It was also observed that close to the base of the cylinder flow of periodic features were not apparent. However, while the probe moves further the downstream in the wake region of the cylinder, the periodic features of flow developed and become more apparent.

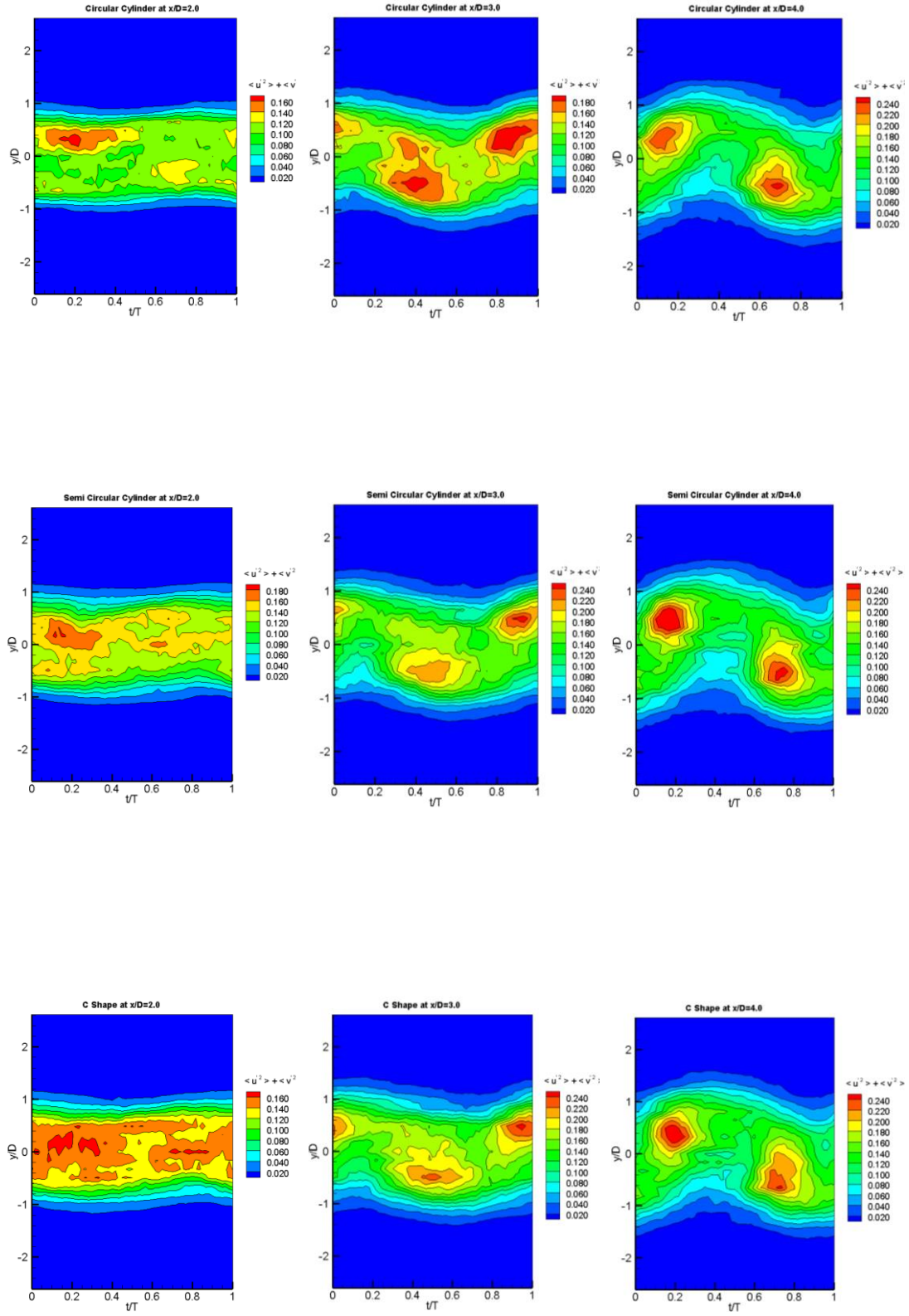

Figure 5.5: Incoherent TKE measured at different x/D behind the Cylinders

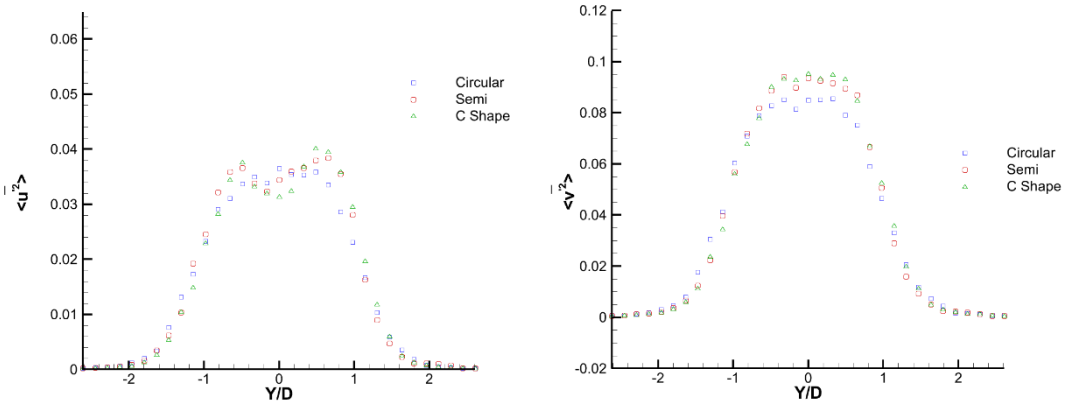

Figure 5.6: Time averaged incoherent normal Reynolds stress (x/D=4.0)

Figure 5.6 illustrated the time averaged of incoherent stream wise and transverse normal Reynolds stresses for various measured at x/D=4.0 in the wake region. From the figure two peaks profile approximately corresponding to the edges of the cylinders are apparent for streamwise stress. On the other hand, the transverse stress reaches a peak alongside the wake center. Moreover, from the figure it can be concluded that the wake region behind the CC exhibited the lowest normal stresses compare to SC and CS.

Chapter 6

NUMERICAL STUDY ON FLOW CHARACTERISTICS IN THE WAKE REGION OF CIRCULAR CYLINDER, SEMI CIRCULAR CYLINDER AND C SHAPE CYLINDER

6.1 Summery

Significant number of researchers have been studying the flow properties and wake formations behind bluff bodies for many years. As a result of various application of bluff bodies in engineering and industry there is a growing interest on this phenomenon. As a significant feature of these geometries is formation of vortices that have shade in their wake region, possible suppression of such phenomenon is a desired outcome. In this chapter wake region behind three modified geometries namely Circular Cylinder, Semi Circular Cylinder and C shape have been investigated for Re of 20000 to identify the effects of shape modification on the wake region. These effects have discussed in terms of flow formation, TKE, pressure and vorticity.

6.2 Numerical Methods

6.2.1 Governing Equations

The SST k-omega turbulence model is a two-equation eddy-viscosity model that is used for many aerodynamic applications. It is a hybrid model combining the Wilcox k-omega and the k-epsilon models.

In this section, the complete formulation of the SST model is given, with the limited number of modifications highlighted.

$$\frac{\partial(\rho k)}{\partial t}+\frac{\partial(\rho U_i k)}{\partial x_i}=\widetilde{P}_k-\beta^*\rho k\omega+\frac{\partial}{\partial x_i}\left[(\mu+\sigma_k\mu_t)\frac{\partial k}{\partial x_i}\right] \tag{6.1}$$

$$\frac{\partial(\rho\omega)}{\partial t}+\frac{\partial(\rho U_i\omega)}{\partial x_i}=\alpha\rho S^2-\beta\rho\omega^2+\frac{\partial}{\partial x_i}\left[(\mu+\sigma_\omega\mu_t)\frac{\partial\omega}{\partial x_i}\right]+2(1-F_1)\rho\sigma_{w2}\frac{1}{\omega}\frac{\partial k}{\partial x_i}\frac{\partial\omega}{\partial x_i}$$

Where the blending function F1 is defined by:

$$F_1=tanh\left\{\left\{min\left[max\left(\frac{\sqrt{k}}{\beta^*\omega y},\frac{500\upsilon}{y^2\omega}\right),\frac{4\rho\sigma_{\omega2}k}{CD_{k\omega}y^2}\right]\right\}^4\right\} \tag{6.2}$$

Where y is the distance to the nearest wall and $CD_{k\omega}$computed as:

$$CD_{kw}=\left(2\rho\sigma_{\omega2}\frac{1}{\omega}\frac{\partial k}{\partial x_i}\frac{\partial\omega}{\partial x_i},10^{-10}\right) \tag{6.3}$$

F1 is equal to zero away from the surface (k-e model), and switches over to one inside the boundary layer (k-w model). The turbulent eddy viscosity is defined as follows:

$$\nu_t=\frac{a_1k}{\max(a_1\omega,SF_2)} \tag{6.4}$$

Where S is the invariant measure of the strain rate and F2 is a second blending function defined by:

$$F_2=tanh\left\{\left[max\left(\frac{2\sqrt{k}}{\beta^*\omega y},\frac{500\upsilon}{y^2\omega}\right)\right]^2\right\} \tag{6.5}$$

A production limiter is used in the SST model to prevent the build-up of turbulence in stagnation regions:

$$P_k=\mu_t\frac{\partial U_i}{\partial x_j}\left(\frac{\partial U_i}{\partial x_j}+\frac{\partial U_j}{\partial x_i}\right)\longrightarrow\quad\tilde{P}_k=\min(P_k,10,\beta^*\rho k\omega) \tag{6.6}$$

All constants are computed by a blend from the corresponding constants of the k-ε and the k-ω model via $\alpha=\alpha_1F+\alpha_2(1-F)$ etc. The constants for this model are: $\beta^*=0.09$,

α_1=5/9, β_1 =3/40, σ_{k1}=0.85, $\sigma_{\omega 1}$=0.5, α_2=0.44, β_2=0.0828, σ_{k2}=1, $\sigma_{\omega 2}$=0.856. The only modifications from the original formulation are the use of the strain rate, S, instead of the vorticity in Equation 3 and the use of the factor 10 in the production limiter, instead of 20 as proposed in (Menter, 1994; Menter, 1993).

6.2.2 Computational Domain and Grid

The dimensions of the computational domain as well as the boundary conditions considered for every simulation is presented in Figure 6.1. Computational domain has divided to two different regions: the main domain is 20D × 60D with the cylinder in the center of the vertical plane and the second region with 10D × 47D for generating a finer mesh in order to increase the accuracy of the simulation and reduce the simulation time. The upper and lower walls are located at a distance of 10D from the center of the cylinder; in order to eliminate the effect of the flow around the cylinder. The flow inlet is located 20D upstream, and flow outlet is located 40D at the rear from the center of the cylinder (Ong, 2010). These distances are acceptable in order to eliminate the effects of far field on the flow around the cylinder. The boundary conditions used for every individual simulations are as follows:

i. Uniform flow velocity of U_∞ *=10.44 m/s* with turbulent intensity of 5 % and turbulent viscosity ratio of 10.
ii. Gage pressure 0 at outlet with backflow turbulent intensity of 5 % and backflow turbulent viscosity ratio of 10.
iii. Stationary wall with No slip condition for cylinders surface.
iv. No slip condition for the far field walls.

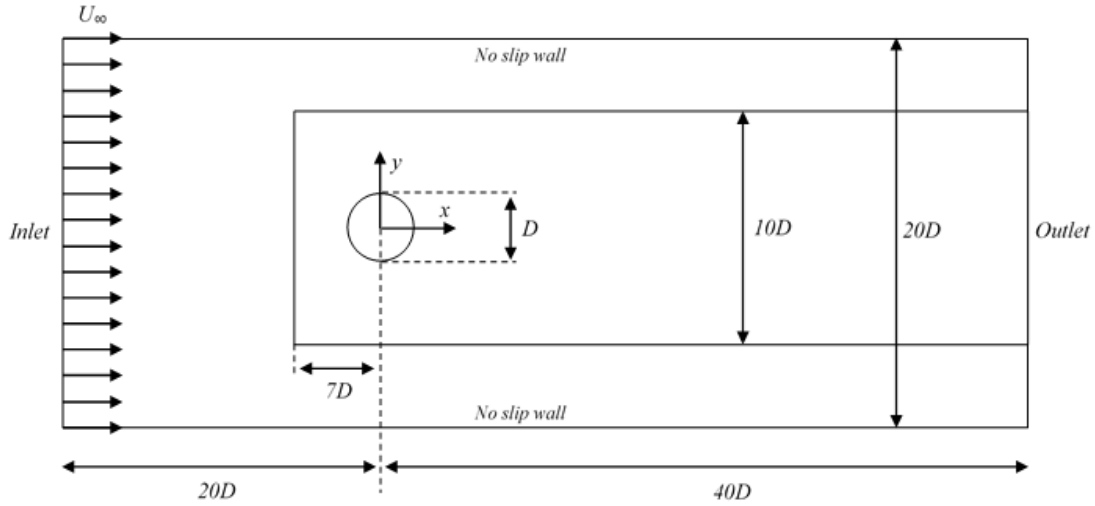

Figure 6.1: Flow domain of circular cylinder

The meshing process for this study is generated by fluent meshing. In all cases, triangle method has made for whole domain with two different element sizes for the main domain and the subdomain with element size of 0.009 and 0.004 respectively. In addition, an inflation method has constructed on the vicinity of the cylinders and shown in figure 6.2.

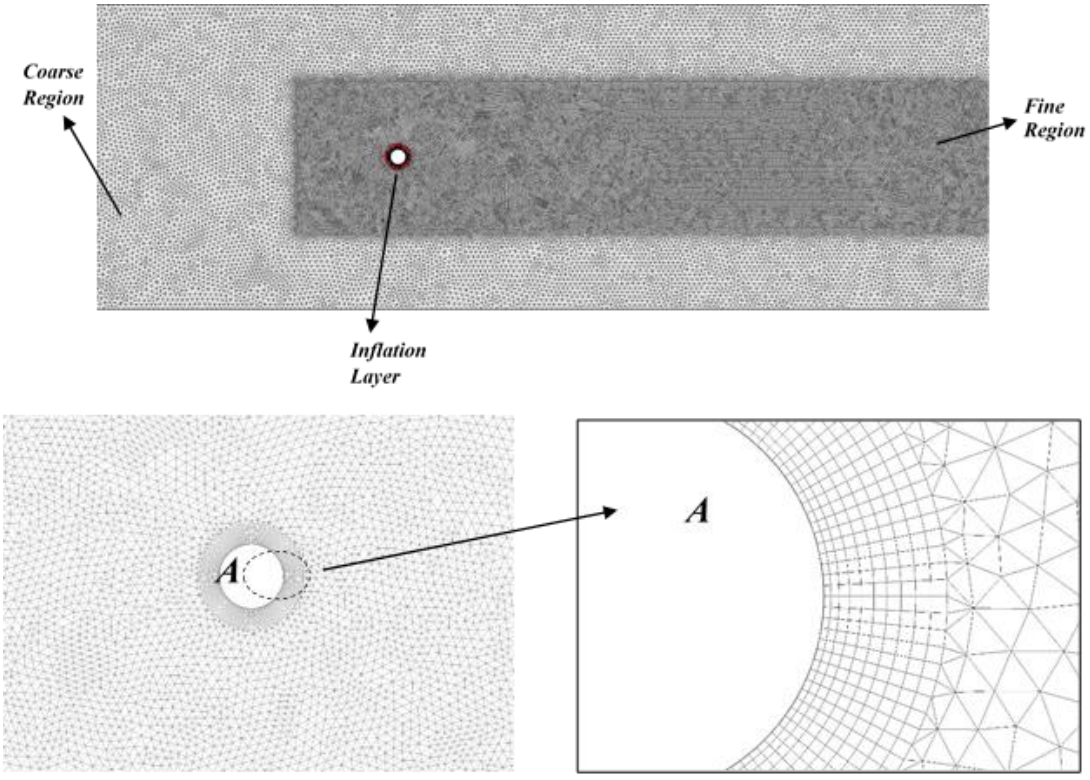

Figure 6.2: The computational mesh for circular cylinder with 38400 nodes and 74928 elements

In order to estimate the distance between the wall and the first grid layer y1, the following formula have used:

$$y_1 = Ly^+\sqrt{74Re_d^{-13/14}} \tag{6.7}$$

Which L is the characteristic length, y+ is conservative value (For $k-\omega$ turbulence model y+ max< 2), and Re_L is the Reynolds number calculated based on the characteristic length. The meshing methods imposed for all the modified geometries in order to be similar with each other to compare the results. Despite that, the number of the elements on each computational domain is varies according to the geometry for instance, the number of elements for SC is 59310 however, in C shape it increases dramatically to 82410 as it presents on figure 6.3. Finally, the max skewness computed for all the cell have been find as 0.1 which is ideal for this study.

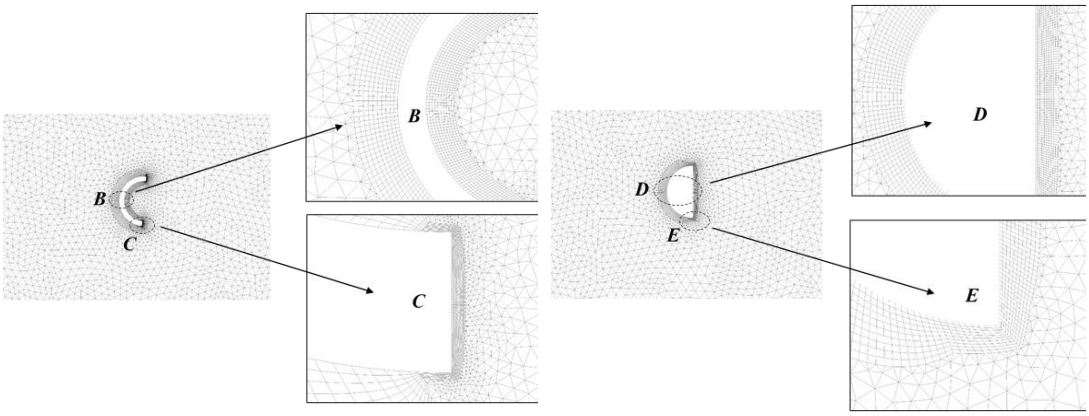

(a) Semi Circular with 31270 nodes and 59310 elements

(b) C shape with 44319 nodes and 82410 elements

Figure 6.3: The computational mesh for semi circular and C shape

6.2.3 Turbulence Modelling

One of the major problems in modelling turbulent flows is the accurate prediction of flow separation from smooth surfaces. Predicting the phenomenon of separation is important in many practical issues for both internal and external flows. This is one of the most important issues in mechanical engineering issues, such as aerodynamic issues of aircraft and turbomachines. Models such as $k-\varepsilon$ often fail to predict the starting point and the flow separation amount. In fact, turbulence models based on Equation $k-\varepsilon$ predict the separation too late and less in its value. The model proposed to solve this problem, in many industrial applications, provide accurate estimates of the separation phenomenon. The most important of these models can be referred to the $k-\omega$ family models. In this study transient simulations have performed with Shear Stress Transport model (SST $k-\omega$) turbulence model in order to predict the beginning and the value of separation point in boundary layer with high accuracy (Cox, 1998).

6.3 Results

The dominant vortex shedding frequency can be obtained from the spectral peak. In this study lift force fluctuation have been employed to obtain the shedding frequency.

The corresponding Strouhal number ($s_t = fD/U_\infty$) can be computed for the geometries. Table 6.1 list the shedding frequencies and corresponding Strouhal number for the three geometries. Also, the drag coefficient for circular cylinder and modified geometries are present in Table 6.1.

Table 6.1: Computed shedding frequencies, corresponding strouhal number, and drag coefficient

	Circular Cylinder (CC)	**Semi Circular (SC)**	**C shape (CS)**
Frequency (f)	93.7	87.4	87.4
Strouhal Number (s_t)	0.269	0.251	0.251
C_d	0.56	1.49	1.51

In order to validate the numerical results, the Strouhal number of both methods have been compared and presented in Table 6.2.

Table 6.2: Numerical and experimental frequency and strouhal no comparison

	Numerical			**Experimental**		
	Circular Cylinder (CC)	**Semi Circular (SC)**	**C shape (CS)**	**Circular Cylinder (CC)**	**Semi Circular (SC)**	**C shape (CS)**
Frequency (f)	93.7	87.4	87.4	63.5	68.4	68.4
Strouhal Number (s_t)	0.269	0.251	0.251	0.182	0.197	0.197

According to the study have been made by (Cox, 1998) for the subcritical two-dimensional simulations, Strouhal number is overpredicted. Therefore, the results of the numerical study are in a good agreement with experimental results,

In this section instantaneous velocity and corresponding pressure, turbulent kinetic energy and vorticity field are demonstrated in figures 6.4-6.18. Figure 6.4-6.6 illustrates the instantaneous velocity u component contours in the wake region up to x/D=8 behind the Circular Cylinder, SC and CS respectively. The development of the vortex street in the wake zone are apparent from the figures. It can be observed that CS cylinder demonstrated lowest acceleration possibly due to entrainment of fluid into the cavity of the shell while SC exhibit the highest peak. In addition, the modification of SC and CS exhibit a stronger reverse flow comparing to the CC.

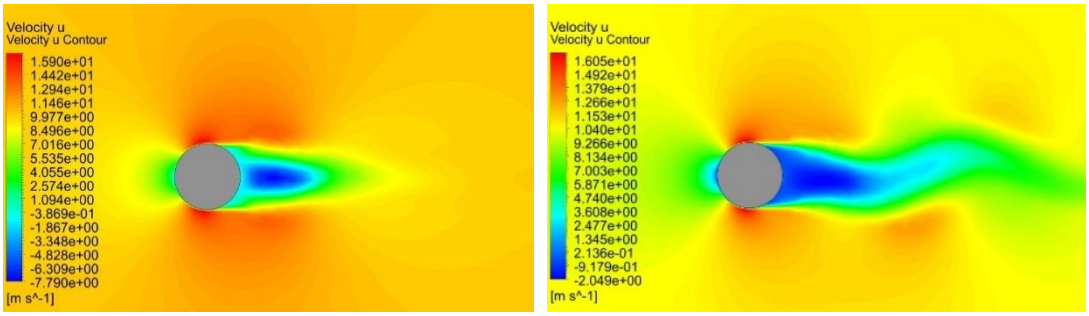

(a)Time=0.015s (b) Time=0.032s

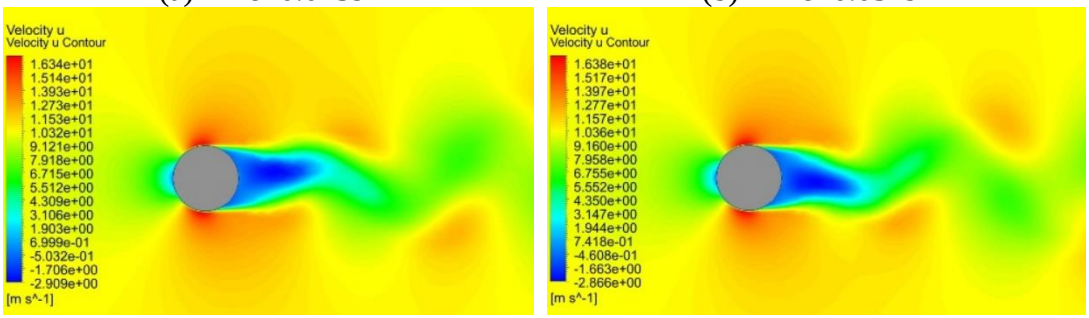

(c) Time=0.047s (d) Time=0.064s

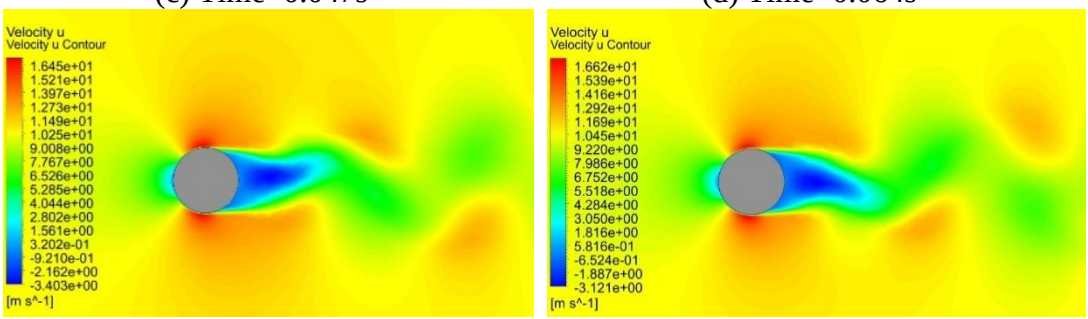

(e) Time=0.080s (f) Time=0.096s

Figure 6.4: Instantaneous streamwise velocity behind the CC

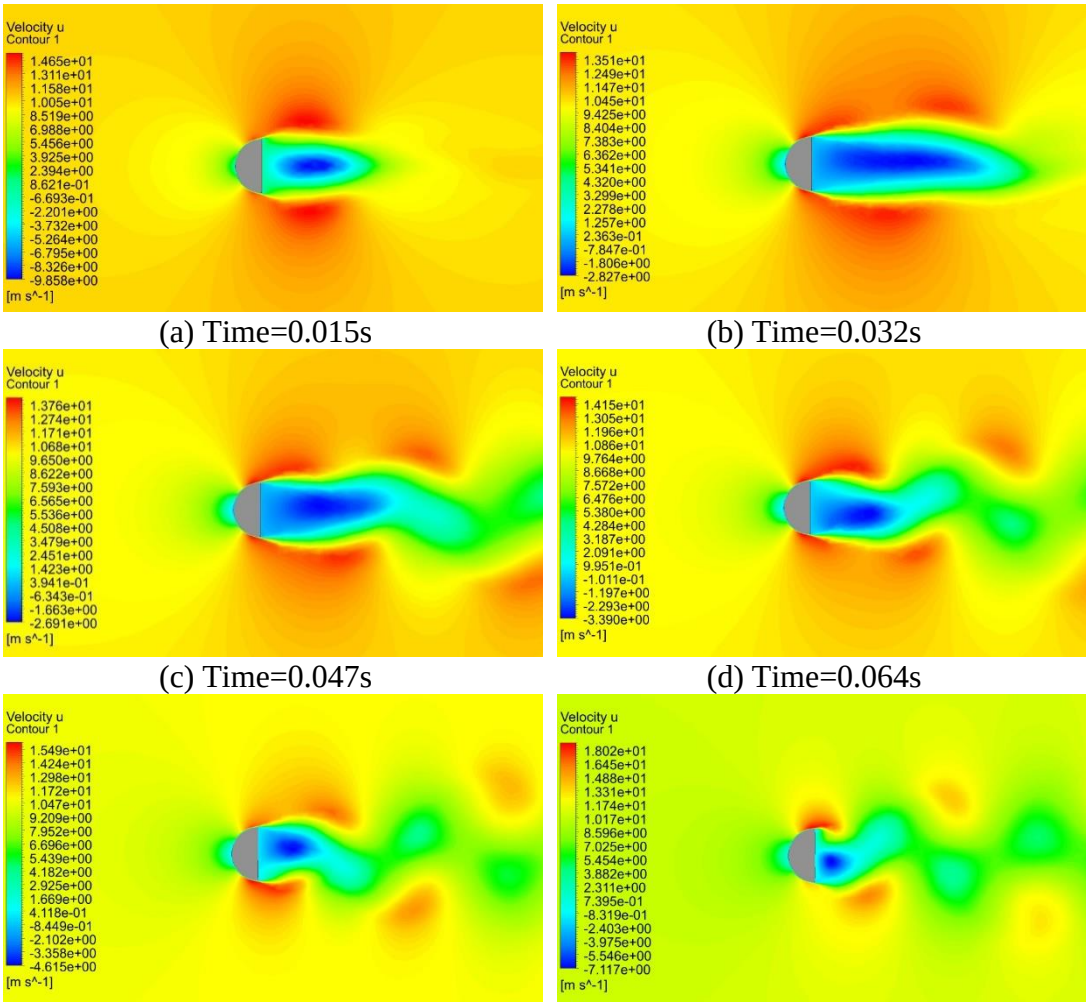

(a) Time=0.015s (b) Time=0.032s

(c) Time=0.047s (d) Time=0.064s

(e) Time=0.080s (f) Time=0.096s

Figure 6.5: Instantaneous streamwise velocity behind the SC Cylinder

For all cases due to the stagnation point in front of the cylinders the pressure value increase and velocity value reduce. From these figures it can observe that the location of the stagnation has not change for all cases. For modified cylinders the recirculation region has separate beyond the cylinder but in CC the flow attached to the rear surface.

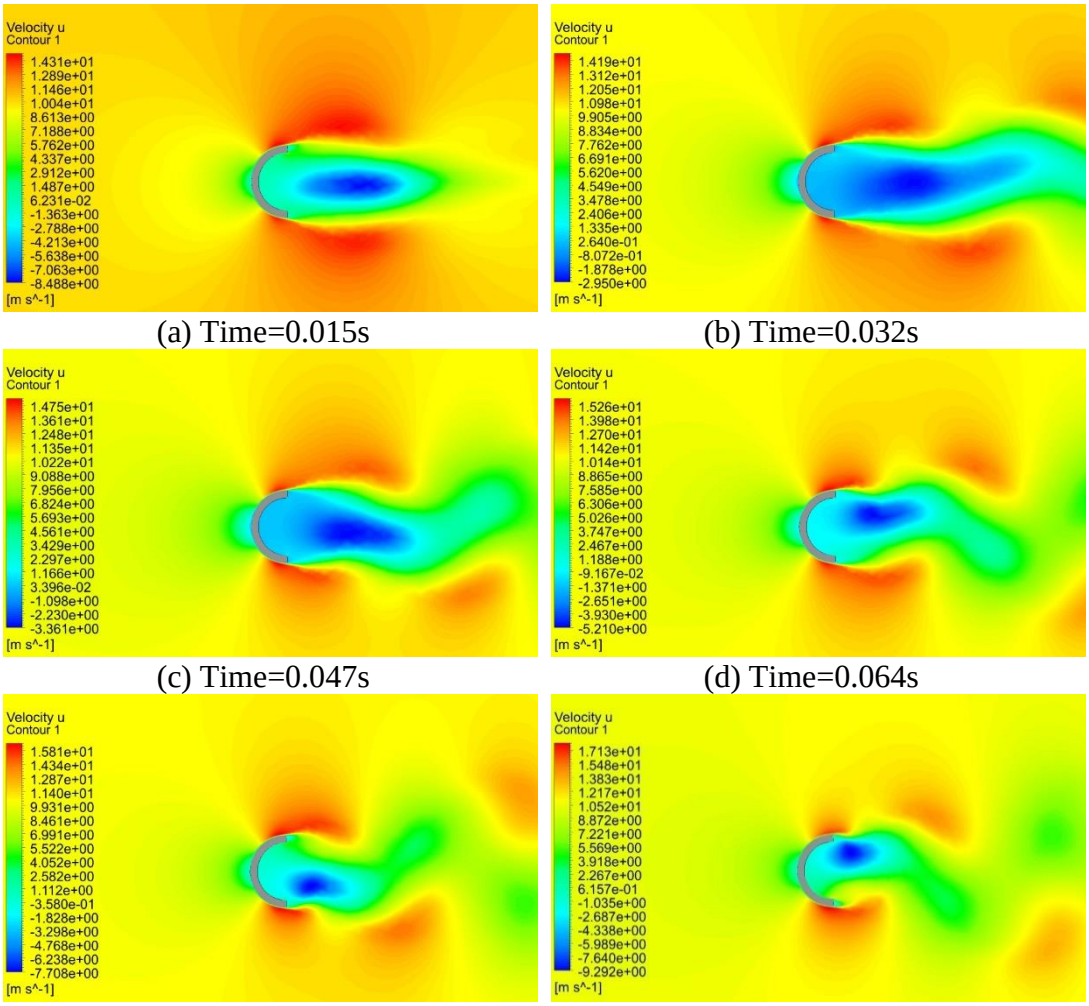

(a) Time=0.015s (b) Time=0.032s

(c) Time=0.047s (d) Time=0.064s

(e) Time=0.080s (f) Time=0.096s

Figure 6.6: Instantaneous streamwise velocity behind the CS Cylinder

Average streamwise velocity are shown in figure 6.7 for the three cases. In all cases, flow has created symmetry about horizontal line (x-axis). This figure present that for the CS cylinder and the SC there are three reverse flow regions, one in each edge and one in center.

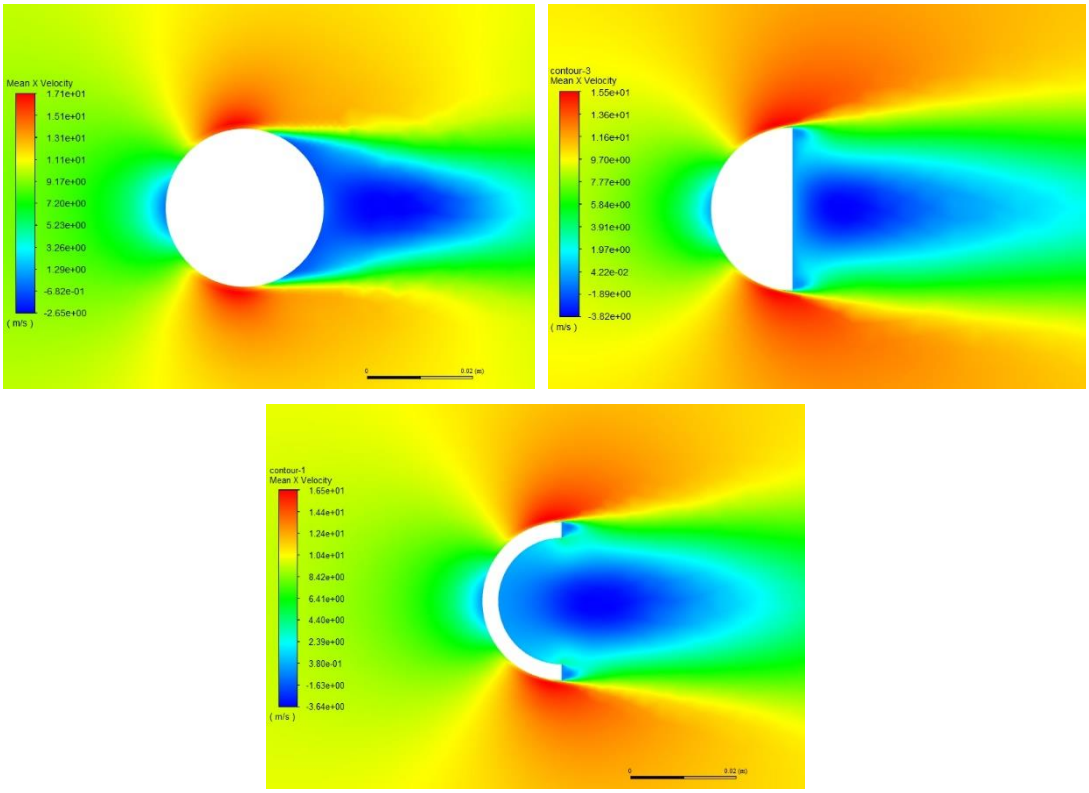

Figure 6.7: Average streamwise velocity behind circular cylinder and the modified bodies

The instantaneous traverse velocity has been presented from figure 6.8-6.10. The figures shown that the v component of the velocity in the upstream of the CC act different than CS cylinder and SC. For instance, in CC they have divided by two large area with highest speed at the top and the lowest reverse flow region at the bottom. On the other hand, for CS cylinder and SC these two regions have been moved and separate from each other and reduce in size gradually.

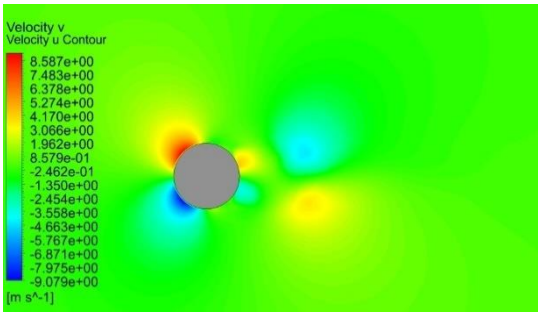

(a) Time=0.015s

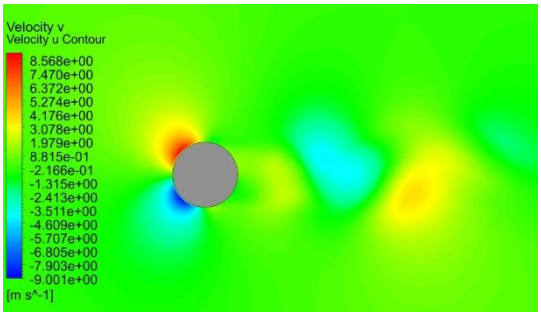

(b) Time=0.032s

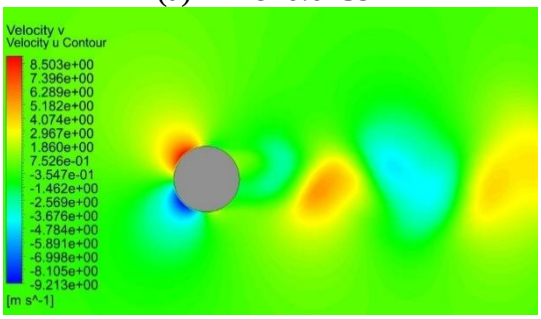

(c) Time=0.047s

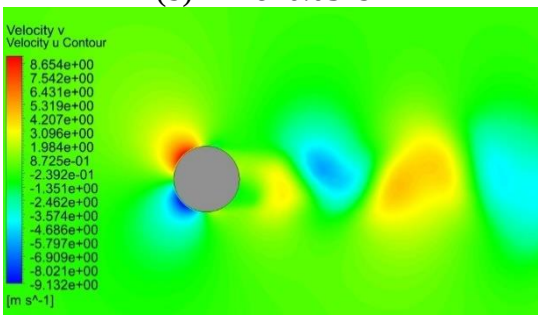

(d) Time=0.064s

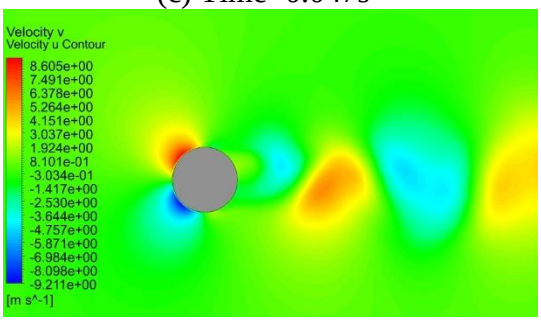

(e) Time=0.080s

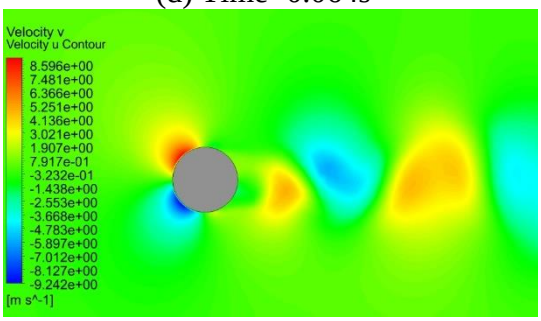

(f) Time=0.096s

Figure 6.8: Instantaneous transverse velocity behind the CC

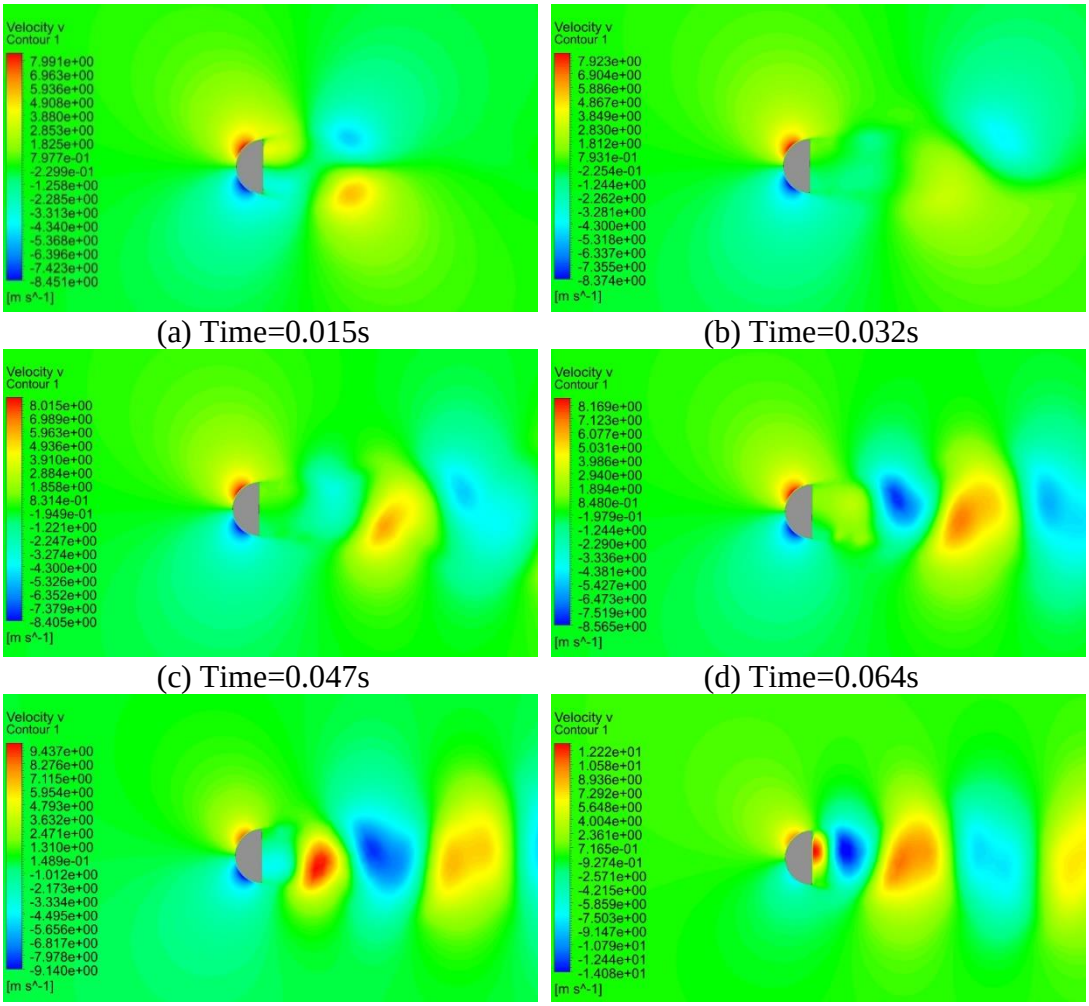

(a) Time=0.015s (b) Time=0.032s

(c) Time=0.047s (d) Time=0.064s

(e) Time=0.080s (f) Time=0.096s

Figure 6.9: Instantaneous transverse velocity behind the SC cylinder

Also, as it presented in figures 6.8f-6.10f, the downstream flow for all cases is shown off differently. For example, in CC the relatively high recirculate region separates and move far away but, in SC cylinder the highest value region stick to the backside surface of the cylinder. Likewise, due to the gap behind CS cylinder the flow entrainment causes the reverse flow and enter to the gap.

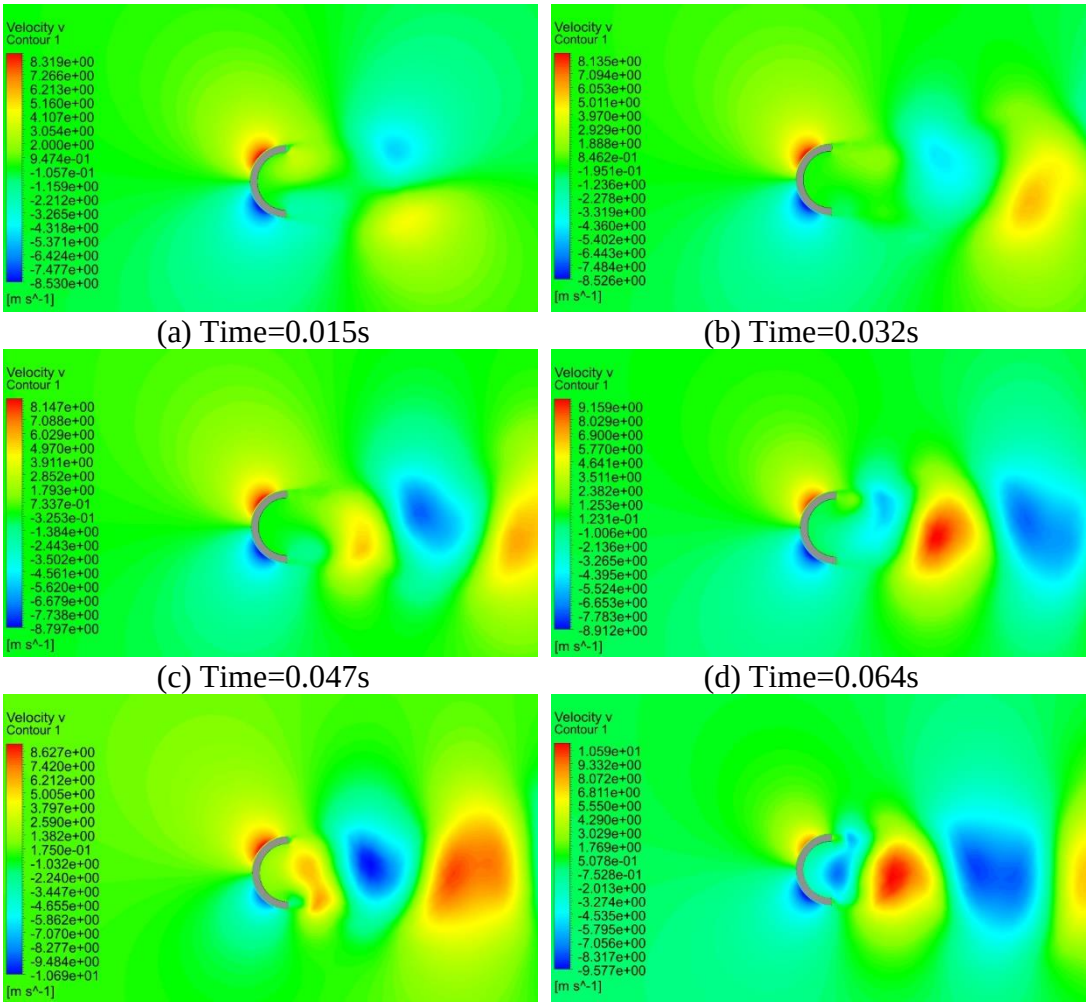

(a) Time=0.015s (b) Time=0.032s

(c) Time=0.047s (d) Time=0.064s

(e) Time=0.080s (f) Time=0.096s

Figure 6.10: Instantaneous transverse velocity behind the CS cylinder

Instantaneous pressure field contours in the wake region are depicted in the figure 6.11-6.13. From the figure the stagnation points with high pressure value can be spotted in front of the cylinders. Moreover, modification of circular cylinder has altered the base pressure of SC and CS cylinder as it can be seen.

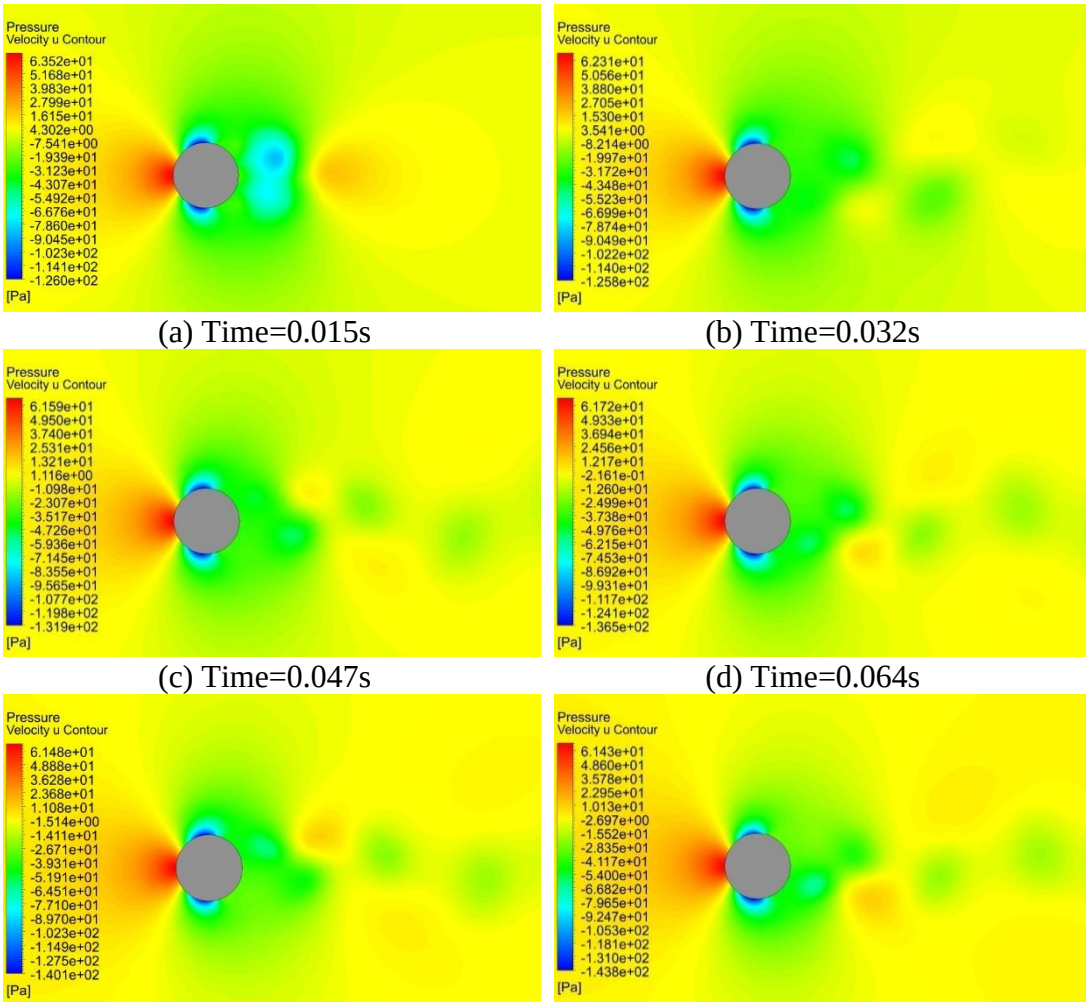

(a) Time=0.015s (b) Time=0.032s

(c) Time=0.047s (d) Time=0.064s

(e) Time=0.080s (f) Time=0.096s

Figure 6.11: Instantaneous pressure behind the CC

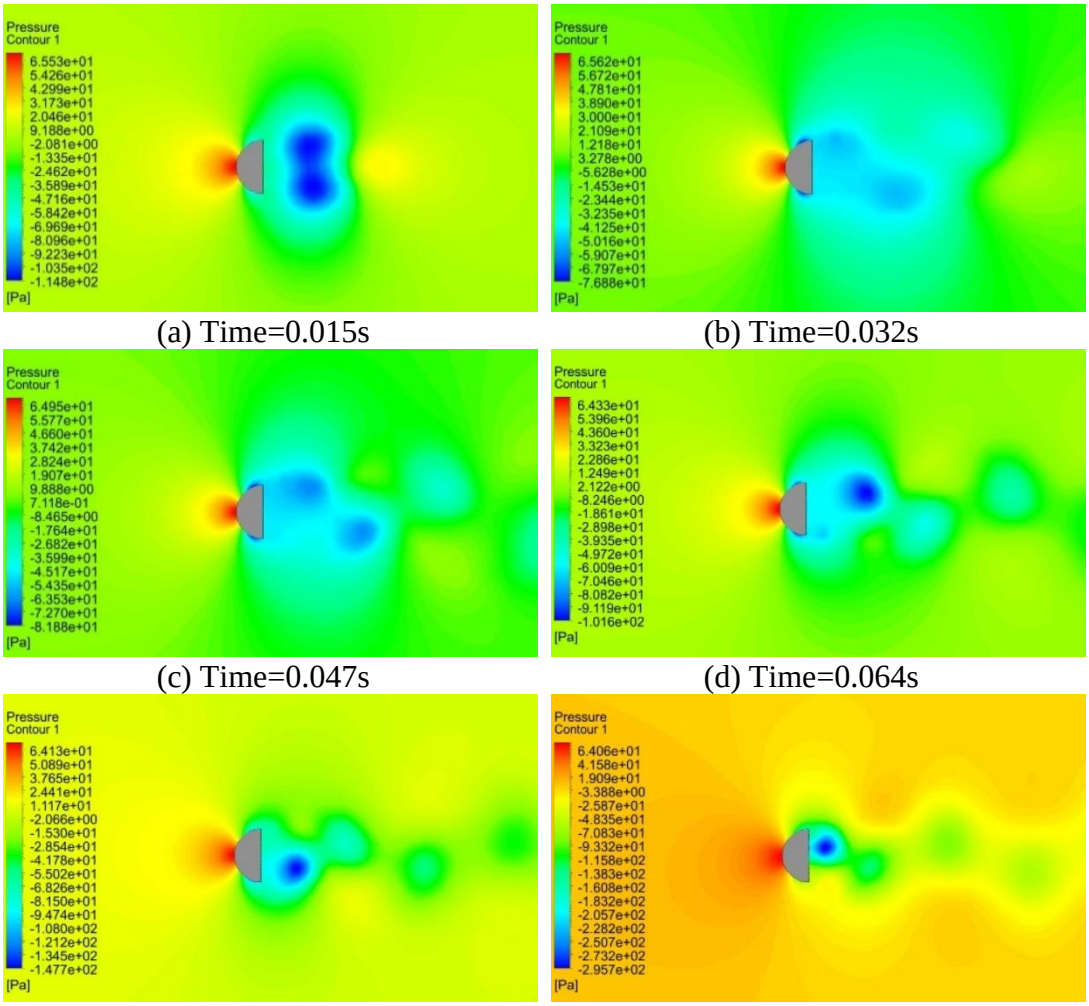

(a) Time=0.015s (b) Time=0.032s

(c) Time=0.047s (d) Time=0.064s

(e) Time=0.080s (f) Time=0.096s

Figure 6.12: Instantaneous pressure behind the SC cylinder

According to the figure 6.12f and 6.13f the wake pressure delayed in CS cylinder respect to SC cylinder. Also, due to the flow entrainment the pressure magnitude falls more that 55%.

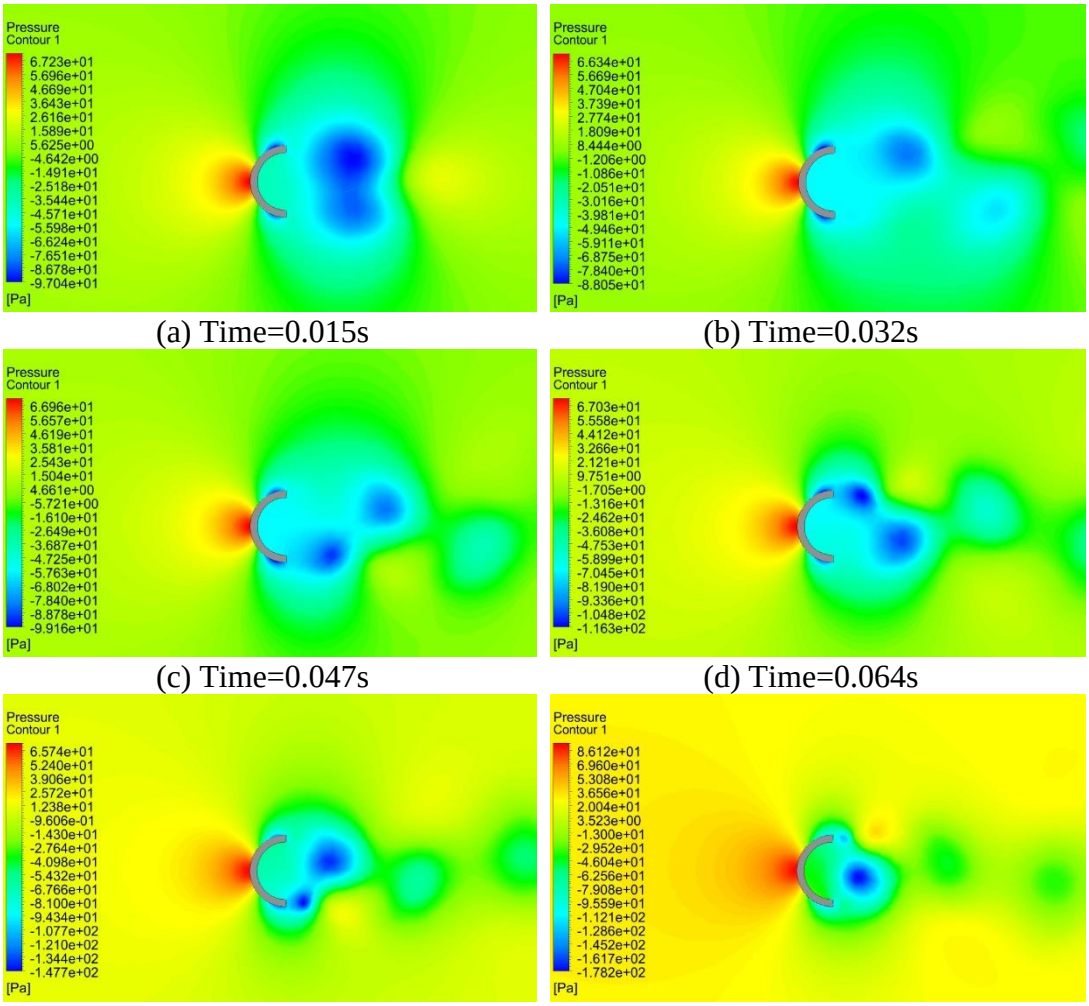

(a) Time=0.015s (b) Time=0.032s

(c) Time=0.047s (d) Time=0.064s

(e) Time=0.080s (f) Time=0.096s

Figure 6.13: Instantaneous pressure behind the CS cylinder

In figure 6.14 the average static pressure contour has presented. This figure illustrates that for the CC there are a low-pressure zone on top and bottom side of the cylinder symmetrically but for the SC this region moves behind the geometry with a bit delay. Also, in CS cylinder the low-pressure region starts from the two edges and move all over behind the gap without any delay.

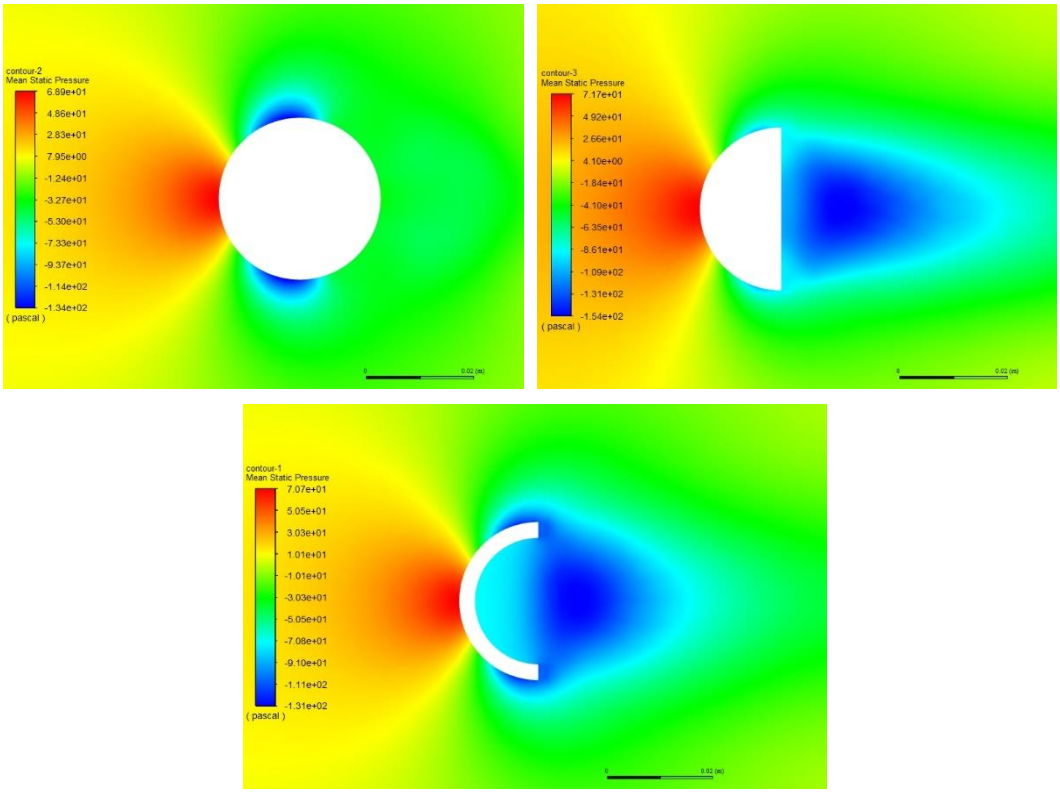

Figure 6.14: Average pressure field behind the modified bodies

Figure 6.15-6.17 illustrates the instantaneous turbulent kinetic energy in the wake zone of circular cylinder and modified cylinder. From the figure the effects of the gematric modification on the TKE at the base region in the wake is apparent. The wake region of CC and SC exhibit a peak value at the sides of separated shear layer. However, CS cylinder exhibit a different structure where the TKE concentrated at the base region along the centerline. Such observation can be as a result of flow entrainment into the cavity of shell. In addition, while CC and SC almost demonstrated similar level of TKE peak value, CS wake region exhibit a significant increase of 40% in the peak value.

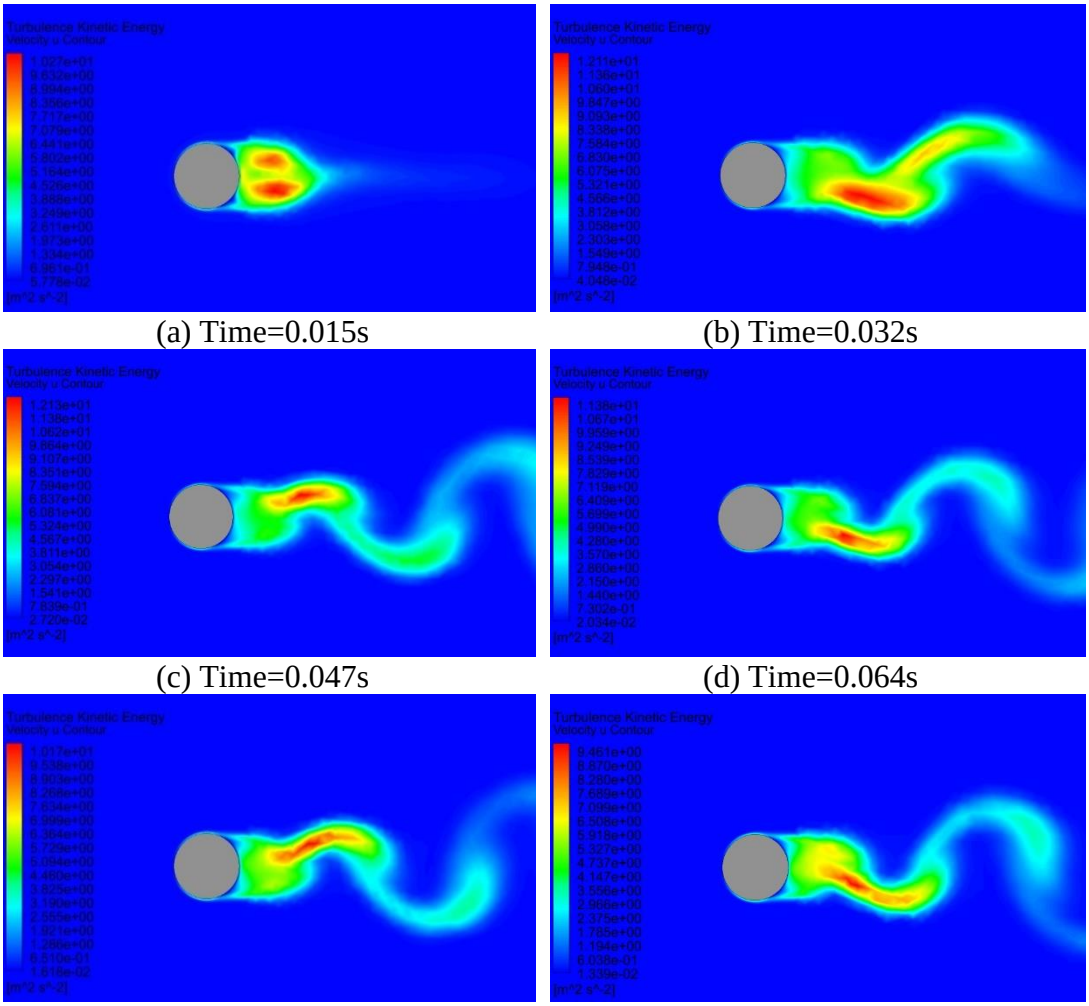

(a) Time=0.015s (b) Time=0.032s

(c) Time=0.047s (d) Time=0.064s

(e) Time=0.080s (f) Time=0.096s

Figure 6.15: Instantaneous TKE behind the CC

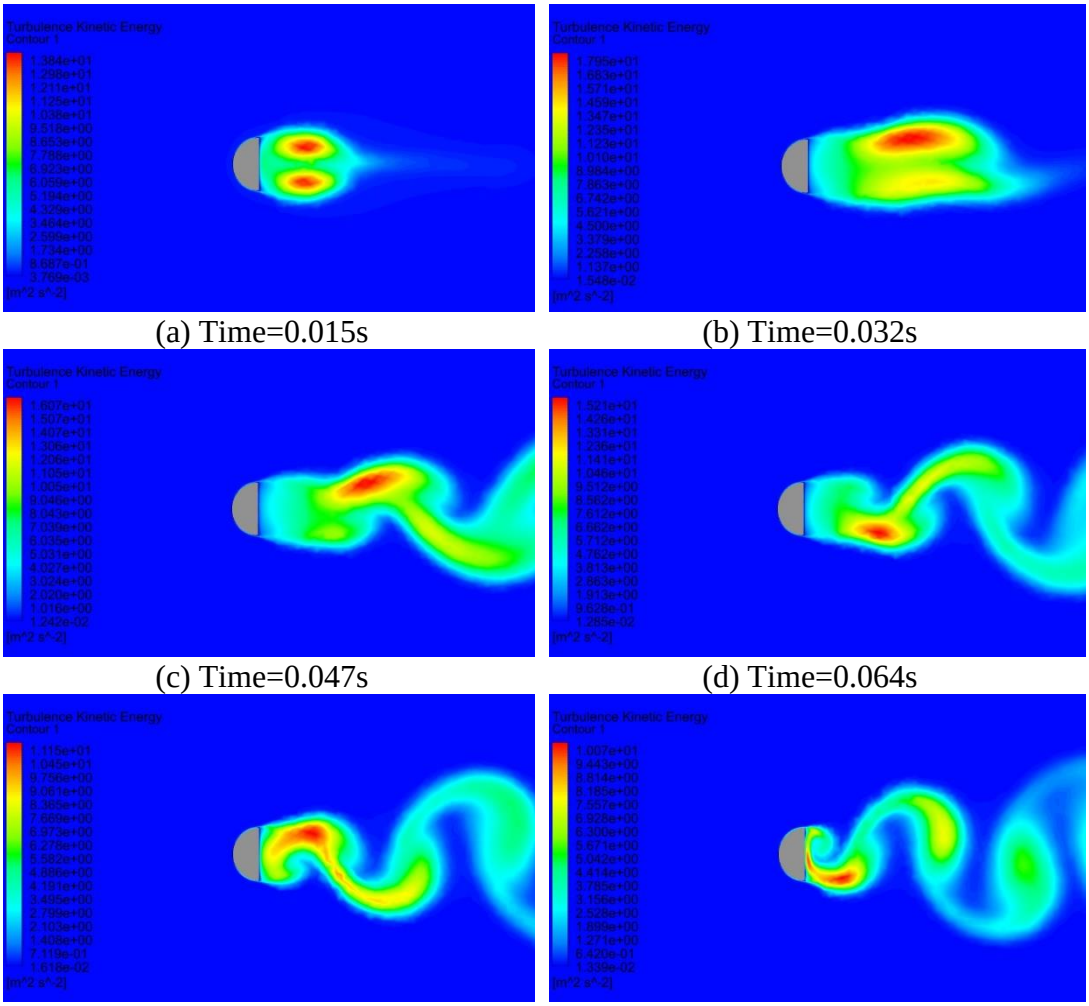

(a) Time=0.015s (b) Time=0.032s

(c) Time=0.047s (d) Time=0.064s

(e) Time=0.080s (f) Time=0.096s

Figure 6.16: Instantaneous TKE behind the SC cylinder

Figures 6.15f-6.16f present that the high value of the turbulence kinetic energy separates with a delay but in SC geometry the high region recirculation didn't separate completely and appeared with two circulate region with low value and high value on top edge and bottom edge respectively. In addition, due to the gap for CS cylinder the moderate value of the huge recirculate entered to the gap and the high region area become smaller respect to the CC and SC cylinder.

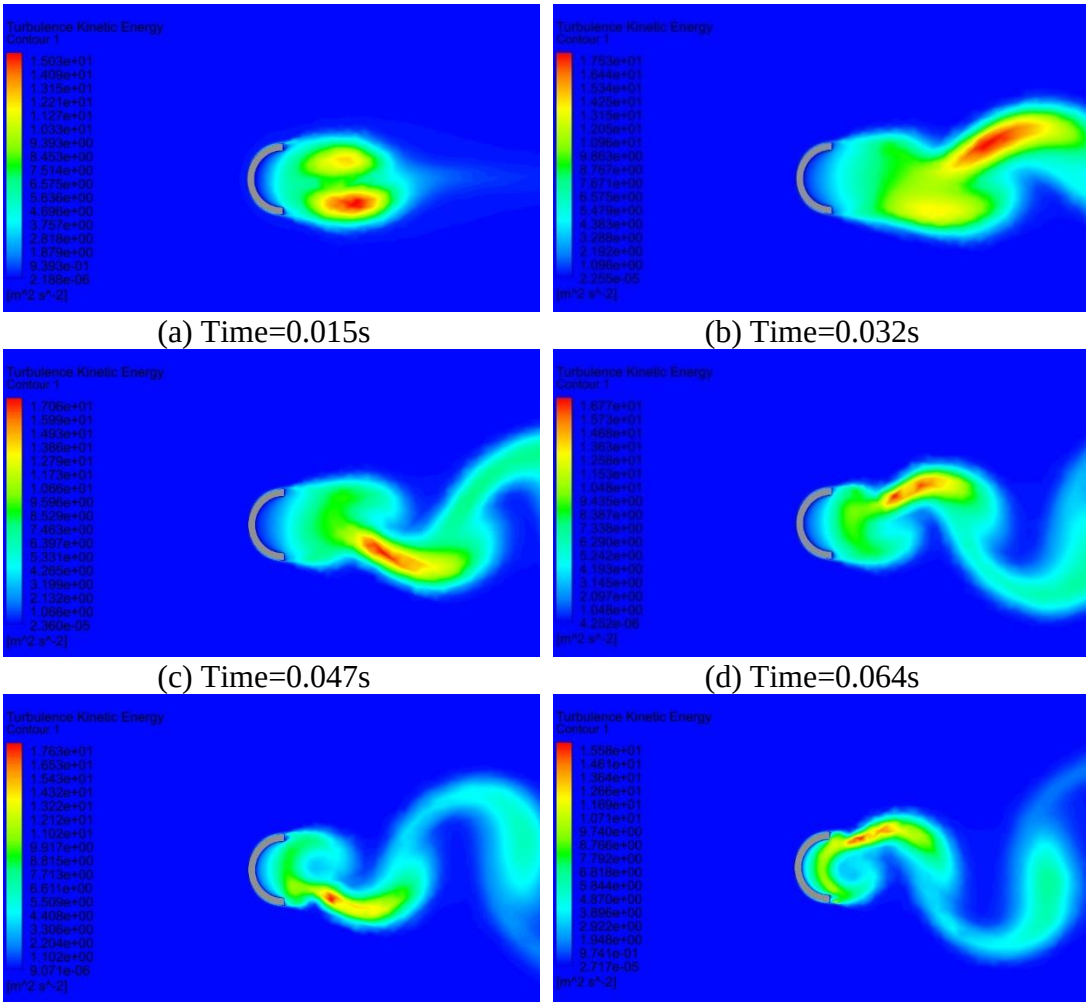

(a) Time=0.015s (b) Time=0.032s

(c) Time=0.047s (d) Time=0.064s

(e) Time=0.080s (f) Time=0.096s

Figure 6.17: Instantaneous TKE behind the CS cylinder

Finally, in order to obtain a better illustration of the shedding phenomenon the instantaneous vorticity behind the circular and modified circular cylinders have been demonstrated in the figure 6.18. As illustrated from the figure the vorticity peak value does not affect significantly by the modifications.

While CC and CS cylinder exhibit similar structure, the SC wake region exhibit with different pattern. The vorticity in the wake region behind CC and CS cylinder concentrated along centerline with some tendency toward the edge of shear layer for the case of vorticity behind of CS cylinder. However, the vorticity in the wake of SC is mostly concentrated along the edges of separated shear layers. In addition, the

separation appeared after 90 degrees for the CC but for SC and CS cylinder the separation point has been dictated by geometry.

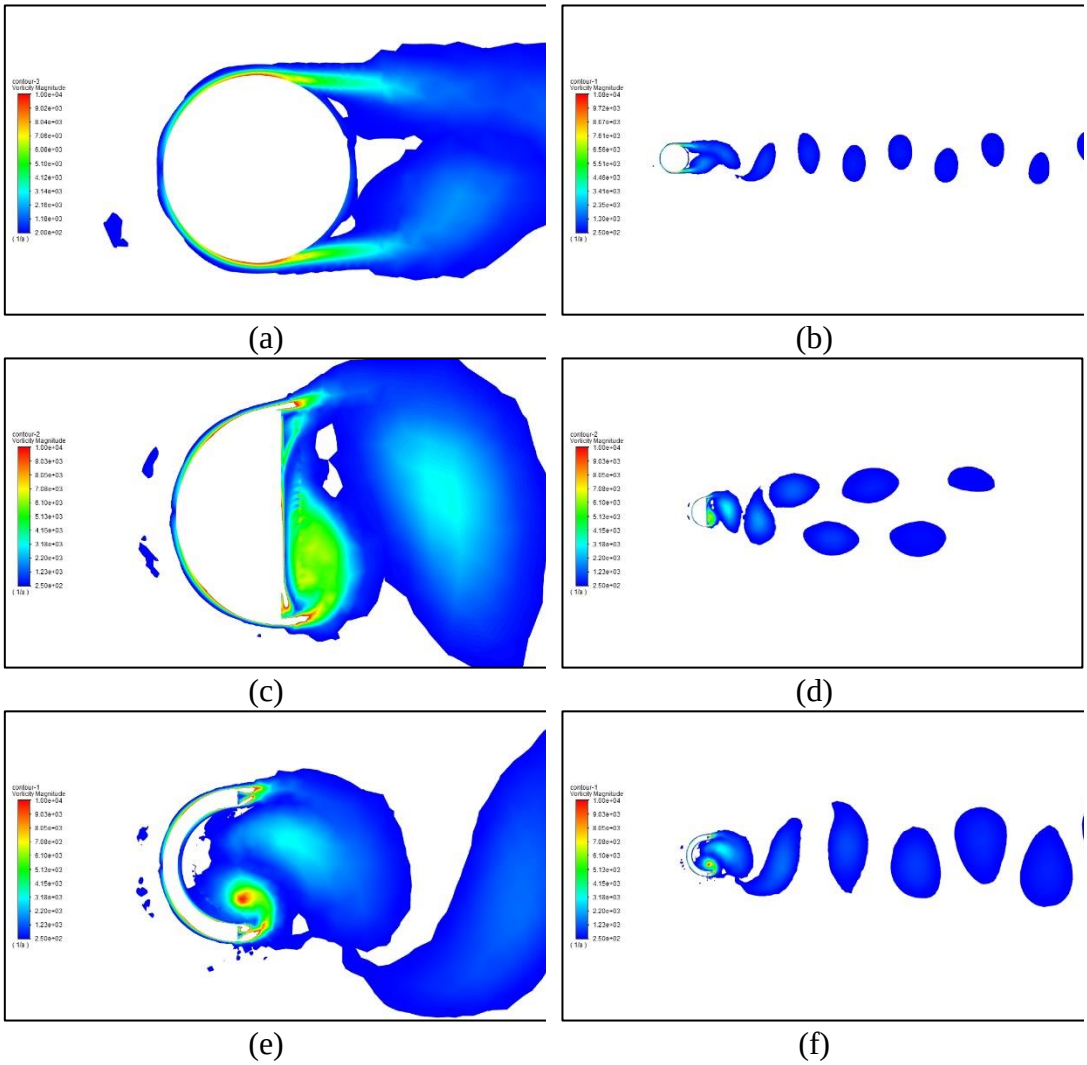

Figure 6.18: Instantaneous vorticity behind the modified cylinders at time=0.16s

Finally, the drag and lift coefficient plot have been present for circular cylinder and S cylinder in figure 6.19. From the figure it can illustrate that there is a significant drop in amplitude of C_d for circular cylinder while the magnitude of the CS cylinder is rising up.

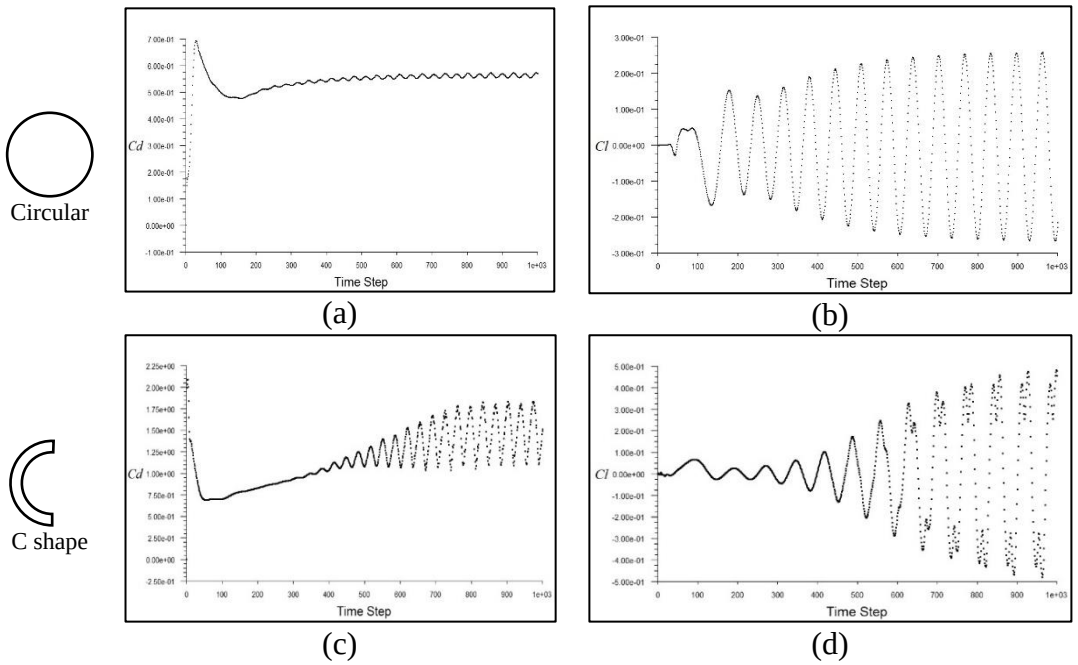

Figure 6.19: Time histories of Cd and Cl value of CC and S cylinder

Moreover, the fluctuation of the C_L has delayed respect to historic time for CS cylinder but the amplitude remains same for both cases.

Chapter 7

CONCLUSION

7.1 Final Remark

This study contains two main scopes: 1- description of triple decomposition technique and its application on the near wake of a square cylinder, and 2- investigation of the flow structure and vortex shedding behind the circular cylinder and it modify cylinders (namely Semi Circular and C shape) experimentally and numerically.

Turbulent flow structure in the downstream of a square cylinder has been studied and different flow characteristic and structures has been investigated. The results of phase averaged time mean velocities and phase averaged fluctuations revealed a symmetrical flow pattern along the centerline. The vortex formation process has been investigated and features of shear stresses corresponding to the vortex shedding have been reported. It was shown that incoherent stresses reach the highest level as vortices are being shed. During vortex formation from one edge of the square cylinder a maximum in the incoherent streamwise normal stress was observed. However, the initiated shear layers from the opposite edge causes a maxima in transverse stress production. Therefore, 1/5 of period after a vortex is shed, significant momentum transfer towards the opposite shear layer was also observed. Turbulent kinetic energy production contours demonstrated that the main turbulent kinetic energy production occurs in the region with the same width of square cylinder.

On the other hand, the flow structure in the downstream wake of modified circular cylinders have been investigated in terms of Strouhal number and coherent and incoherent turbulent kinetic energy (TKE). The result illustrated the evolution of the TKE production in the downstream wake. TKE is observed to be concentrated at sides of the separated shear layer for low x/D's whereas TKE peaks spotted at centerline in the wake region for higher x/D's. Finally, a double peaks profile corresponding to the edges of the cylinders have been observed for time averaged incoherent normal Reynolds stresses in streamwise direction.

I addition, a complimentary study using numerical simulation have been conducted to investigate the wake region behind modified circular cylinder and to demonstrate the effects of it on the wake region. The numerical study results have been verified and validated by experimental results. The flow domain has been studied in terms of velocity, pressure, turbulent kinetic energy and vorticity contour.

Entrainment of fluid into the cavity of the C shape was illustrated and accelerated and reverse flow have been compared for the three geometries. It was observed that while CC and SC demonstrated similar level of TKE peak value, CS wake region exhibit a significant increase of 40% in the peak value. It was also illustrated that the vorticity in the wake region of SC is mostly concentrated along the edges of separated shear layers.

7.2 Suggestions for future studies

Further experiments are required to investigate the flow characteristics behind bluff bodies with finite curvature to sharp edge structure at subcritical to supercritical Reynolds domain.

Also, an experimental study could perform for suppressing the vortex shedding downstream of a perforated square cylinder in front of a circular cylinder with different gap ratios for various Reynolds regime.

Moreover, PIV measurements can be employed for further studies of the tandem inclined plates arrangements. PIV have capability of global flow field velocity measurement while hot wire anemometer (HWA) only provides point-wise 99 measurements. Therefore, the gap region between the two plates can be also investigated for better insight to this problem.

REFERENCES

Abbassi, H., Turki, S., & Nasrallah, S. B. (2001). Numerical investigation of forced convection in a plane channel with a built-in triangular prism. *International Journal of Thermal Sciences, 40*(7), 649-658.

Achenbach, E., & Heinecke, E. (1981). On vortex shedding from smooth and rough cylinders in the range of Reynolds numbers 6× 103 to 5× 106. *Journal of Fluid Mechanics, 109*, 239-251.

Baj, P., Bruce, P. J., & Buxton, O. R. (2015). The triple decomposition of a fluctuating velocity field in a multiscale flow. *Physics of Fluids, 27*(7), 075104.

Bearman, P. (1971). An investigation of the forces on flat plates normal to a turbulent flow. *Journal of Fluid Mechanics, 46*(01), 177-198.

Bearman, P., & Obasaju, E. (1982). An experimental study of pressure fluctuations on fixed and oscillating square-section cylinders. *Journal of Fluid Mechanics, 119*, 297-321.

Behara, S., & Mittal, S. (2011). Transition of the boundary layer on a circular cylinder in the presence of a trip. *Journal of fluids and structures, 27*(5-6), 702-715.

Blackburn, H., & Melbourne, W. (1996). The effect of free-stream turbulence on sectional lift forces on a circular cylinder. *Journal of Fluid Mechanics, 306*, 267-292.

Bosch, G., & Rodi, W. (1998). Simulation of vortex shedding past a square cylinder with different turbulence models. *International journal for numerical methods in fluids, 28*(4), 601-616.

Bradshaw, P. (1996). *An Introduction to Turbulence and Its Measurement*: Pergamon Press.

Bradshaw, P. (2013). *An introduction to turbulence and its measurement: thermodynamics and fluid mechanics series*: Elsevier.

Bruun, H. H. (1996). Hot-wire anemometry: principles and signal analysis. In: IOP Publishing.

Cadot, O., Desai, A., Mittal, S., Saxena, S., & Chandra, B. (2015). Statistics and dynamics of the boundary layer reattachments during the drag crisis transitions of a circular cylinder. *Physics of Fluids, 27*(1), 014101.

Cantwell, B., & Coles, D. (1983). An experimental study of entrainment and transport in the turbulent near wake of a circular cylinder. *Journal of Fluid Mechanics, 136*, 321-374.

Chopra, G., & Mittal, S. (2017). The intermittent nature of the laminar separation bubble on a cylinder in uniform flow. *Computers & fluids, 142*, 118-127.

Çuhadaroglu, B. (2009). A numerical study on turbulent flow around a square cylinder with uniform injection or suction. *International Journal of Numerical Methods for Heat & Fluid Flow, 19*(6), 708-727.

Çuhadaroğlu, B., & Turan, O. (2009). Numerical simulation of turbulent flow around a square cylinder with uniform injection or suction and heat transfer. *Numerical Heat Transfer, Part A: Applications, 55*(2), 163-184.

Derakhshandeh, J., & Alam, M. M. (2019). A review of bluff body wakes. *Ocean Engineering, 182*, 475-488.

Desai, A., Mittal, S., & Mittal, S. (2020). Experimental investigation of vortex shedding past a circular cylinder in the high subcritical regime. *Physics of Fluids, 32*(1), 014105.

Durbin, P. A. (1994). Turbulence modeling for separated flow. *Annual Research Briefs-1994*, 97.

Dutta, S., Panigrahi, P., & Muralidhar, K. (2008). Experimental investigation of flow past a square cylinder at an angle of incidence. *Journal of engineering mechanics, 134*(9), 788-803.

Enotiadis, A., Vafidis, C., & Whitelaw, J. (1990). Interpretation of cyclic flow variations in motored internal combustion engines. *Experiments in Fluids, 10*(2-3), 77-86.

Farell, C., & Blessmann, J. (1983). On critical flow around smooth circular cylinders. *Journal of Fluid Mechanics, 136*, 375-391.

Gad-El-Hak, M. (1998). Fluid mechanics from the beginning to the third millennium. *International Journal of Engineering Education, 14*(3), 177-185.

Gao, N., Li, Y., Bai, H., & Wu, C. J. (2016). Effects of Synthetic jets on a D-Shaped Cylinder wake at a Subcritical Reynolds Number. *Flow, Turbulence and Combustion, 97*(3), 729-742.

Hacışevki, H., & Teimourian, A. (2015). Comparison of flow structures in the wake region of two similar normal flat plates in tandem and a square cylinder. *Experimental Thermal and Fluid Science, 69*, 169-177.

Hacışevki, H., & Teimourian, A. (2016). Interacting wakes of a narrow and a wide flat plate in tandem arrangement. *Fluid Dynamics Research, 48*(1), 015505.

Hourigan, K., Thompson, M. C., & Tan, B. T. (2001). Self-sustained oscillations in flows around long blunt plates. *Journal of fluids and structures, 15*(3-4), 387-398.

Irwin, P. A. (2008a). Bluff body aerodynamics in wind engineering. *Journal of Wind Engineering and Industrial Aerodynamics, 96*(6-7), 701-712.

Irwin, P. A. (2008b). Bluff body aerodynamics in wind engineering. *Journal of Wind Engineering and Industrial Aerodynamics, 96*(6), 701-712.

Jackson, C. (1987). A finite-element study of the onset of vortex shedding in flow past variously shaped bodies. *Journal of Fluid Mechanics, 182*, 23-45.

Johansson, S. H., Davidson, L., & Olsson, E. (1993). Numerical simulation of vortex shedding past triangular cylinders at high Reynolds number using ak-ε turbulence model. *International journal for numerical methods in fluids, 16*(10), 859-878.

Jorgensen, F. (1971). Directional sensitivity of wire and fiber-film probes. *DISA information, 11*(3), 1-7.

King, L. V. (1915). LVII. On the precision measurement of air velocity by means of the linear hot-wire anemometer. *The London, Edinburgh, and Dublin Philosophical Magazine and Journal of Science, 29*(172), 556-577.

Knauss, D. T., John, J., & Marks, C. (1976). The vortex frequencies of bluff cylinders at low Reynolds numbers. *Journal of Hydronautics, 10*(4), 121-126.

Knauss, D. T., John, J. E., & Marks, C. H. (1976). The vortex frequencies of bluff cylinders at low Reynolds numbers. *Journal of Hydronautics, 10*(4), 121-126.

Kurtulus, D., Scarano, F., & David, L. (2007). Unsteady aerodynamic forces estimation on a square cylinder by TR-PIV. *Experiments in Fluids, 42*(2), 185-196.

Lehmkuhl, O., Rodríguez, I., Borrell, R., Chiva, J., & Oliva, A. (2014). Unsteady forces on a circular cylinder at critical Reynolds numbers. *Physics of Fluids, 26*(12), 125110.

Lin, Y.-J., Miau, J.-J., Tu, J.-K., & Tsai, H.-W. (2011). Nonstationary, three-dimensional aspects of flow around circular cylinder at critical Reynolds numbers. *AIAA journal, 49*(9), 1857-1870.

Lyn, D., Einav, S., Rodi, W., & Park, J.-H. (1995). A laser-Doppler velocimetry study of ensemble-averaged characteristics of the turbulent near wake of a square cylinder. *Journal of Fluid Mechanics, 304*, 285-319.

Lyn, D., & Rodi, W. (1994). The flapping shear layer formed by flow separation from the forward corner of a square cylinder. *Journal of Fluid Mechanics, 267*, 353-376.

Meliga, P., Pujals, G., & Serre, E. (2012). Sensitivity of 2-D turbulent flow past a D-shaped cylinder using global stability. *Physics of Fluids, 24*(6), 061701.

Minguez, M., Brun, C., Pasquetti, R., & Serre, E. (2011). Experimental and high-order LES analysis of the flow in near-wall region of a square cylinder. *International Journal of Heat and Fluid Flow, 32*(3), 558-566.

Murakami, S., & Mochida, A. (1995). On turbulent vortex shedding flow past 2D square cylinder predicted by CFD. *Journal of Wind Engineering and Industrial Aerodynamics, 54*, 191-211.

Nishimura, H., & Taniike, Y. (2001). Aerodynamic characteristics of fluctuating forces on a circular cylinder. *Journal of Wind Engineering and Industrial Aerodynamics, 89*(7-8), 713-723.

Nishiyama, H., Ota, T., & Matsuno, T. (1988). Heat transfer and flow around elliptic cylinders in tandem arrangement. *JSME international journal. Ser. 2, Fluids engineering, heat transfer, power, combustion, thermophysical properties, 31*(3), 410-419.

Okajima, A. (1982). Strouhal numbers of rectangular cylinders. *Journal of Fluid Mechanics, 123*, 379-398.

Ozgoren, M. (2006). Flow structure in the downstream of square and circular cylinders. *Flow Measurement and Instrumentation, 17*(4), 225-235.

Ozgoren, M., Pinar, E., Sahin, B., & Akilli, H. (2011). Comparison of flow structures in the downstream region of a cylinder and sphere. *International Journal of Heat and Fluid Flow, 32*(6), 1138-1146.

Parezanovic, V., & Cadot, O. (2012). Experimental sensitivity analysis of the global properties of a 2D turbulent wake. *J. Fluid Mech, 693*, 115.

Perrin, R., Braza, M., Cid, E., Cazin, S., Chassaing, P., Mockett, C., . . . Thiele, F. (2009). *Coherent and turbulent process analysis in the flow past a circular cylinder at high Reynolds number.* Paper presented at the IUTAM Symposium on Unsteady Separated Flows and their Control.

Perry, A., & Steiner, T. (1987). Large-scale vortex structures in turbulent wakes behind bluff bodies. Part 1. Vortex formation processes. *Journal of Fluid Mechanics, 174*, 233-270.

Provansal, M., Schouveiler, L., & Leweke, T. (2004). From the double vortex street behind a cylinder to the wake of a sphere. *European Journal of Mechanics-B/Fluids, 23*(1), 65-80.

Rashidi, S., Bovand, M., Pop, I., & Valipour, M. (2014). Numerical simulation of forced convective heat transfer past a square diamond-shaped porous cylinder. *Transport in Porous Media, 102*(2), 207-225.

Rashidi, S., Nouri-Borujerdi, A., Valipour, M., Ellahi, R., & Pop, I. (2015). Stress-jump and continuity interface conditions for a cylinder embedded in a porous medium. *Transport in Porous Media, 107*(1), 171-186.

Reynolds, W., & Hussain, A. (1972). The mechanics of an organized wave in turbulent shear flow. Part 3. Theoretical models and comparisons with experiments. *Journal of Fluid Mechanics, 54*(2), 263-288.

Rodi, W. (1993). On the simulation of turbulent flow past bluff bodies. *Journal of Wind Engineering and Industrial Aerodynamics, 46*, 3-19.

Roshko, A. (1954). On the drag and shedding frequency of two-dimensional bluff bodies.

Saha, A., Muralidhar, K., & Biswas, G. (2000). Experimental study of flow past a square cylinder at high Reynolds numbers. *Experiments in Fluids, 29*(6), 553-563.

Schewe, G. (1983). On the force fluctuations acting on a circular cylinder in crossflow from subcritical up to transcritical Reynolds numbers. *Journal of Fluid Mechanics, 133*, 265-285.

Singh, S., & Mittal, S. (2005). Flow past a cylinder: shear layer instability and drag crisis. *International journal for numerical methods in fluids, 47*(1), 75-98.

Sjunnesson, A., Nelsson, C., & Max, E. (1991). LDA measurements of velocities and turbulence in a bluff body stabilized flame.

So, R. M., & Savkar, S. D. (1981). Buffeting forces on rigid circular cylinders in cross flows. *Journal of Fluid Mechanics, 105*, 397-425.

Stalnov, O., Palei, V., Fono, I., Cohen, K., & Seifert, A. (2007). Experimental estimation of a D-shaped cylinder wake using body-mounted sensors. *Experiments in Fluids, 42*(4), 531-542.

Taylor, Z. J., Gurka, R., & Kopp, G. A. (2014). Effects of leading edge geometry on the vortex shedding frequency of an elongated bluff body at high Reynolds numbers. *Journal of Wind Engineering and Industrial Aerodynamics, 128*, 66-75.

Teimourian, A., Hacisevki, H., & Bahrami, A. (2017). Experimental study on flow past two inclined flat plates in tandem arrangement. *Journal of Wind Engineering and Industrial Aerodynamics, 169*, 1-11.

Tennekes, H., Lumley, J. L., & Lumley, J. L. (1972). *A first course in turbulence*: MIT press.

Tiederman, W., Privette, R., & Phillips, W. (1988). Cycle-to-cycle variation effects on turbulent shear stress measurements in pulsatile flows. *Experiments in Fluids, 6*(4), 265-272.

Wesfreid, J., Goujon-Durand, S., & Zielinska, B. (1996). Global mode behavior of the streamwise velocity in wakes. *Journal de Physique II, 6*(10), 1343-1357.

Yeon, S. M., Yang, J., & Stern, F. (2016). Large-eddy simulation of the flow past a circular cylinder at sub-to super-critical Reynolds numbers. *Applied Ocean Research, 59*, 663-675.

Zang, Z.-P., & Gao, F.-P. (2014). Steady current induced vibration of near-bed piggyback pipelines: Configuration effects on VIV suppression. *Applied Ocean Research, 46*, 62-69.

Zang, Z.-P., Gao, F.-P., & Cui, J.-S. (2013). Physical modeling and swirling strength analysis of vortex shedding from near-bed piggyback pipelines. *Applied Ocean Research, 40*, 50-59.

Zdravkovich, M. (1997). Flow around Circular Cylinders; Vol. I Fundamentals. *Journal of Fluid Mechanics, 350*(1), 377-378.

Zhang, X., & Perot, B. (2000). Turbulent vortex shedding from triangle cylinder using the turbulent body force potential model. *Proceedings of ASME Fluids Engineering Division, FEDSM2000, 11172*.

Zielinska, B., & Wesfreid, J. (1995). On the spatial structure of global modes in wake flow. *Physics of Fluids, 7*(6), 1418-1424.